Nanostructured Porous High Surface Area Ceramics for Catalytic Applications

PhD Thesis

In partial fulfillment of the requirements
for the academic degree of

Doctor rerum naturalium

(Dr.rer.nat.)

Submitted to

The Faculty of Mathematics and Natural Sciences
of the Dresden University of Technology

by

M.Sc.Eng. Piotr Krawiec

Born on May 18,1978 in Krasnystaw (Poland)

Approved by: Prof. Dr. Stefan Kaskel

Prof. Dr. Ferdi Schüth

Prof. Dr. Wladimir Reschetilowski

Submitted on: August 11,2006.

Date of oral examination: December 20, 2006

Contents

1. Motivation

Since the discovery of ordered mesoporous silica in 1992[1, 2], many reports were published on possible applications of those materials in catalysis[3, 4]. One advantage of an ordered pore structure is a precise control of pore diameter by changing the size of templating molecules, or addition of swelling agents. Another one is the existence of different pore arrangement symmetries e.g cubic, lamellar, or hexagonal - affecting the guest molecules mobility and reactant diffusivity.[3, 5] Before this discovery, ordered porous structures were only known for crystalline microporous materials like zeolites or macroporous foams with low specific surface areas. However, the pore size of the M41S family materials (MCM-41 with hexagonal and MCM-48 with cubic pore symmetry developed by Mobil) was small (2-6 nm) and new procedures had to be developed to prepare materials with larger pores. Preparation of large pore silica was especially desired for immobilization of large molecules like enzymes, proteins and for improving mobility inside the pores.[6] In 1998 Zhao et.al. reported the use of block co-polymers as templates for the preparation of ordered mesoporous silica materials with 4-30 nm pore diameter and hexagonal geometry.[7, 8] However, silica is not always considered to be an optimal support. The low chemical resistance in alkaline conditions, hydrolysis and hydrophilic surface makes it unattractive for many applications. Therefore similar synthesis procedures have been developed to prepare other oxides (like TiO_2, ZrO_2, Al_2O_3) with ordered mesoporosity, exhibiting different chemical properties than silica.[9, 10] On the other hand, the sol-gel syntheses methods are often not suitable for preparation of non-oxide materials. Ryoo et al. showed that nanocasting of MCM-48 or SBA-15 can be used for preparation of ordered mesoporous carbons designed as CMK-1 and CMK-3 materials.[11-13] Typically, the source of carbon is a simple sugar (sucrose) which is carbonized at higher temperatures. The silica template is removed afterwards by treatment with HF or NaOH and pure carbon material is obtained. If one goes one step further, also CMK materials can be used as a templates for nanocasting,[14, 15] especially in the case where silica removal conditions could damage the product. For example boron nitride can be prepared by nanocasting of CMK-3 and subsequent removal of carbon matrix in ammonia flow.[16]

This thesis shows that ordered mesoporous silica can be used as hard template for the preparation of ordered mesoporous silicon carbide (via nanocasting) and as a support for highly dispersed (catalytically active) species. Ex-situ and in-situ incorporation procedures are also used in order to incorporate noble metals (like platinum and palladium), vanadium nitride and vanadium carbide.

High surface nitrides and carbides, are promising supports or catalysts for heterogeneous catalysis. Nitrides and carbides were typically used as structural ceramics (BN, BC, SiC, Si_3N_4) due to their high mechanical strength (especially at high temperatures), hardness and high thermal conductivity (SiC).[17] However, they are not available commercially as high surface area materials. Therefore, it is of high interest to develop new synthesis procedures for preparation of porous carbide and nitride nanostructures with high specific surface areas. Due to their specific properties, nano-meter sized carbide and nitride materials are not only of interest in catalysis[18] but also in electronics and as a nanocomposite components.[19]

It is shown in this work, how mesoporous silicon carbide is prepared via infiltration into ordered mesoporous silica structure and subsequent removal of silica by HF treatment. The applied procedures include: chemical vapor deposition from simple silanes,[20, 21] reactions under high autogenic pressures[21] and liquid infiltration of low molecular weight polycarbosilanes and their further conversion to SiC.[22] The obtained materials were chracterised by specific surface areas of up to 830 m^2g^{-1} and large mesopore volumes (up to 0.9 cm^3g^{-1}). What is important, mesoporous SiC has a high thermal stability, higher than that of SBA-15 template. A highly ordered pore structure with narrow pore size distribution was achieved for polycarbosilane derived materials. These materials are of interest as supports due to their high thermal stability, heat conductivity and chemical inertness.[18]

Transition metal nitrides were found to exhibit similar catalytic properties as the group VIII metals (Pt, Pd, Rh).[23] Therefore they may become an economic alternative for expensive precious metal catalysts.[24] However, preparation of high surface area transition metal nitrides and carbides is difficult. A new synthetic approach to prepare high surface area transition metal nitrides and supported transition metal nitrides and carbides is proposed in this thesis. Instead of pure oxide (V_2O_5), a high volume macroporous composite consisting of amine intercalated V_2O_5 is used as a precursor and upon nitridation, high surface area vanadium nitride (up to 190 m^2g^{-1}) is formed.[25] In contrast, preparation from pure V_2O_5 under similar conditions gives material with surface areas up to 33 m^2g^{-1} only and the highest value reported in literature was 90 m^2g^{-1}.[26] Highly dispersed VN and VC were also prepared, using ordered mesoporous silica, and activated carbon as supports. The prepared materials were also found to have high catalytic activity in non-oxidative propane dehydrogenation as compared to materials synthesized by standard procedure.

The work also presents an effective in-situ procedure to incorporate metals into mesoporous MCM-41 silica.[27] A swelling agent (toluene), which is typically used to expand the pore diameter of MCM-41,[28] is used to deliver hydrophobic metal precursors

(acetylacetonate complexes). The high incorporation (80-100 % yield) of metal and absence of large particles outside of the pore system makes this short procedure interesting. Moreover, in the case of Pt containing MCM-41, template removal process was enhanced catalytically by the metal allowing lower calcinations temperatures.

2. Introduction

2.1 Ordered Mesoporous Materials

M-41S family

According to IUPAC, porous materials can be divided into three classes depending on the pore size [Figure 1].[29] Materials with pore diameter smaller than 2 nm are called microporous and typical representatives of those are crystalline zeolites (eg. ZSM-5)[30, 31] or more recently discovered metal-organic frameworks.[32-35] In zeolites, pores are created by templating with single molecules (which are removed afterwards by calcination, creating empty spaces) or are a consequence of a unique crystalline structure. In the case of metal-organic frameworks, the crystalline porous material is formed from organic linkers (eg. terephtalic acid) and metals to which they are connected, forming three-dimensional coordination polymers. The pore size control is achieved by adjusting the linker size.[32] However, also amorphous microporous materials exist, like activated carbons[36] or materials prepared by templating with small organic molecules.[37] The microporous materials are of great importance in catalysis (zeolites are used in petroleum processing)[30] as well as in adsorption applications (gas storage, purification of liquids and gases).[38-41]
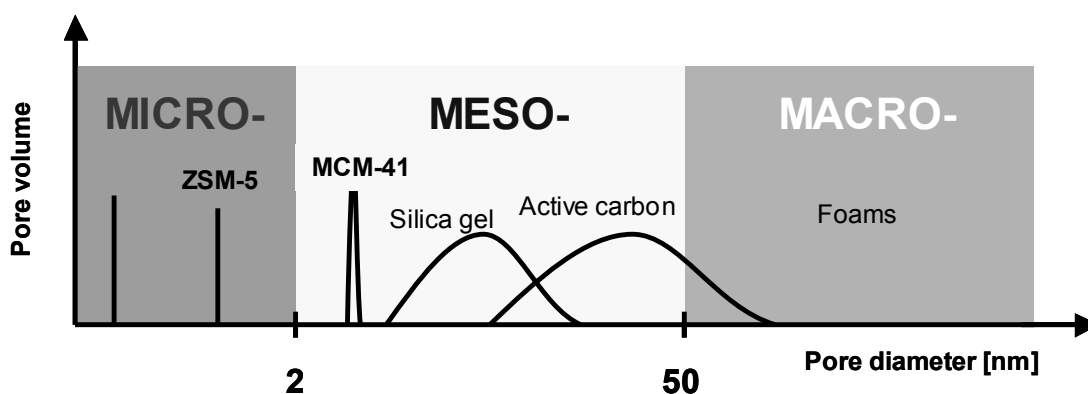
Figure 1. IUPAC classification of porous materials with respect to pore diameter

On the other end of the IUPAC scale [Figure 1 - MACRO-] macroporous materials with pore diameters larger than 50 nm are classified.[29] They can be prepared by templating with large organic or inorganic materials, solvent drying or mechanical treatment.[42-44] Although the macroporous materials typically possess small surface areas, they are often used in catalysis as supports in form of monoliths. The large pores allow to use fast gas flows and to avoid pressure drops in catalyst beds.

Materials with a pore diameter in between 2 and 50 nm are assigned as mesoporous. They are of great interest due to their large specific surface areas and larger pore diameters than in the case of microporous materials. The latter is extremely important in processing or immobilization of large molecules where microporous substances have often too small pore diameters to host large molecules (eg. enzymes) or cause diffusion limitations.[6, 45] Mesoporous materials are typically synthesized as aerogels, xerogels (oxides) or as activated carbons with disordered pore. The main disadvantage of these methods is that typically materials with broad pore size distribution [Figure 1 – silica gel, active carbon] and moderate surface areas are prepared.

In 1992 scientists from Mobil Co. synthesized for the first time ordered mesoporous silica materials (M41S) with a very narrow pore size distribution.[1] The expression "ordered" was referred to the 3-dimensional pore ordering, since pore walls of such materials are amorphous. Unlike in zeolites where single molecules are used as templates, in the case of M41S family self assembled molecular aggregates or supramolecular assemblies are used as the structure directing agents. However, different mechanisms of formation are proposed, from templating of already existing liquid crystal assemblies (*true liquid crystal templating*) to formation of ordered structures from disordered surfactant micelles solutions (*cooperative self assembly*) [Figure 2].
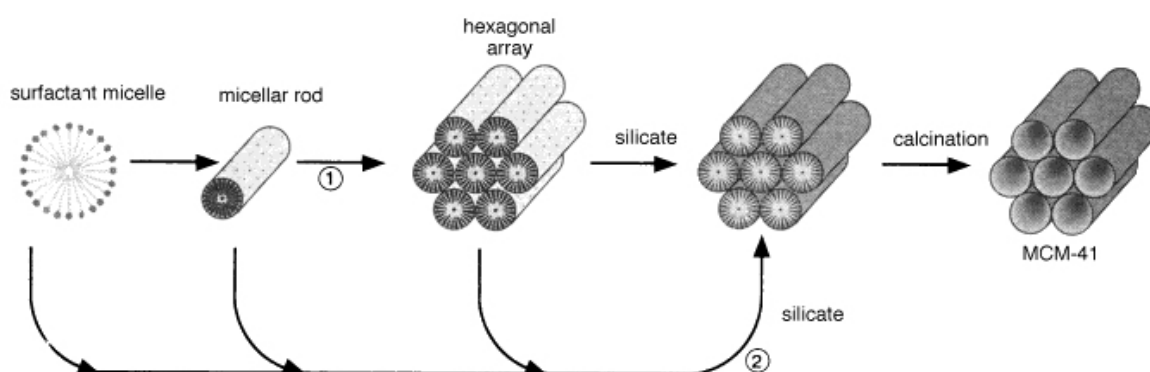
Figure 2. Two possible pathways for the liquid crystal templating mechanism. (1) True liquid crystal templating (2) Cooperative self assembly[1]

Already in the first report[1, 2] materials with hexagonal, cubic (space group: Ia3d) and lamellar symmetry of pore ordering were prepared by using ionic surfactants as templates or structure directing agents [Figure 3]. The influence of chemical composition (surfactant to silicon ratio, water concentration - Figure 4Figure 4) as well as geometrical dimensions of

templating molecules were found to play a crucial role in the formation of different 3-dimensional pore structures [Figure 5].

MCM-41   **MCM-48**   **MCM-50**
Hexagonal   **Cubic**   **Lamellar**
p6m   *Ia3d*   *p2*
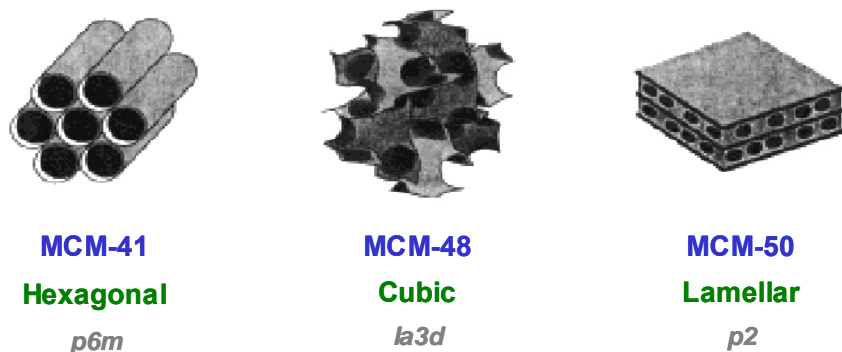
Figure 3. Ordered mesoporous silica materials with different symmetry of pore ordering synthesized by Mobil Co.[1]
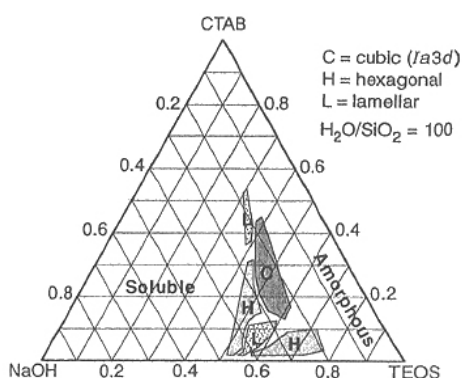
Figure 4. Influence of chemical composition for a given synthesis procedure on the symmetry of pore ordering[46]

The so called effective surfactant packing parameter g (g=$V/a_0 l$) was proposed to predict the structure formation [Figure 5].[47-49] Different 3D pore arrangements can be easily identified on the basis of low angle X-ray diffractograms [Chapter 3.2] or by analysis of crystallographic lattice planes in transmission electron micrographs.

Effective packing parameter:

$$g = V/a_0 l$$

g	micelle shape	predicted mesophase
<1/3	spherical	cubic (Pm3n)
1/3-1/2	cylindrical	hexagonal (p6m)
1/2-2/3	flexible bilayer	cubic (Ia3d)
2/3-1	planar bilayer	lamellar (p2)
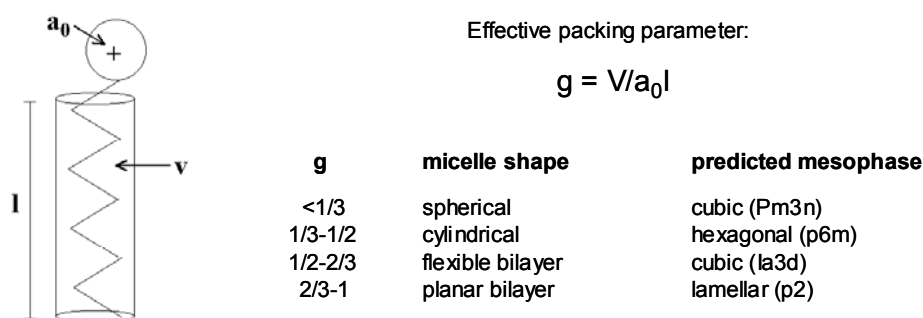
Figure 5. Surfactant geometry and its influence on the micelle shape as well as on the predicted mesophase ordering (the latter depends also strongly on the synthesis conditions). a_0 is a head group surface area (l) hydrophobic chain length and (v) its volume.[47-49]

Several reviews were published concerning the mechanisms of formation (liquid crystal templating [Figure 2 – 1] and cooperative self-assembly [Figure 2 – 2])[4, 5, 50] as well as possible applications of such materials (especially in catalysis as support and for preparation of other high surface area materials via nanocasting).[3, 51] Recently, also preparation of ordered mesoporous silica with chiral pore structure by using chiral surfactant molecules as template was reported.[52]

In fact, as important as the control over the 3-dimensional structure is the possibility of precise pore diameter adjustment. Surfactants having different hydrocarbon chain length can be applied [Figure 6 – hydrocarbon chain length].[1, 53, 54] Templates with long hydrocarbons form larger micelles than surfactants with a short hydrophilic tail. As a consequence, ordered mesoporous materials prepared from larger micelles have larger pore diameters. However, if the hydrocarbon chain is too long, the molecule is too hydrophobic and does not dissolve in water. In the case of MCM-41, the pore size can be controlled in the approximate range of 1.6 nm to 4 nm. Another known possibility is addition of swelling agents (eg. Trimethylbenzene, Toluene).[2, 28, 55] In this case, the hydrophobic swelling agent is transported into the core of the micelle causing swelling (the diameter of the micelle increases - Figure 6 – swelling agents). However, the main disadvantage of this method is that only a limited amount of swelling agent can be introduced, and too high concentrations disturb the 3-dimensional ordering of the pores.
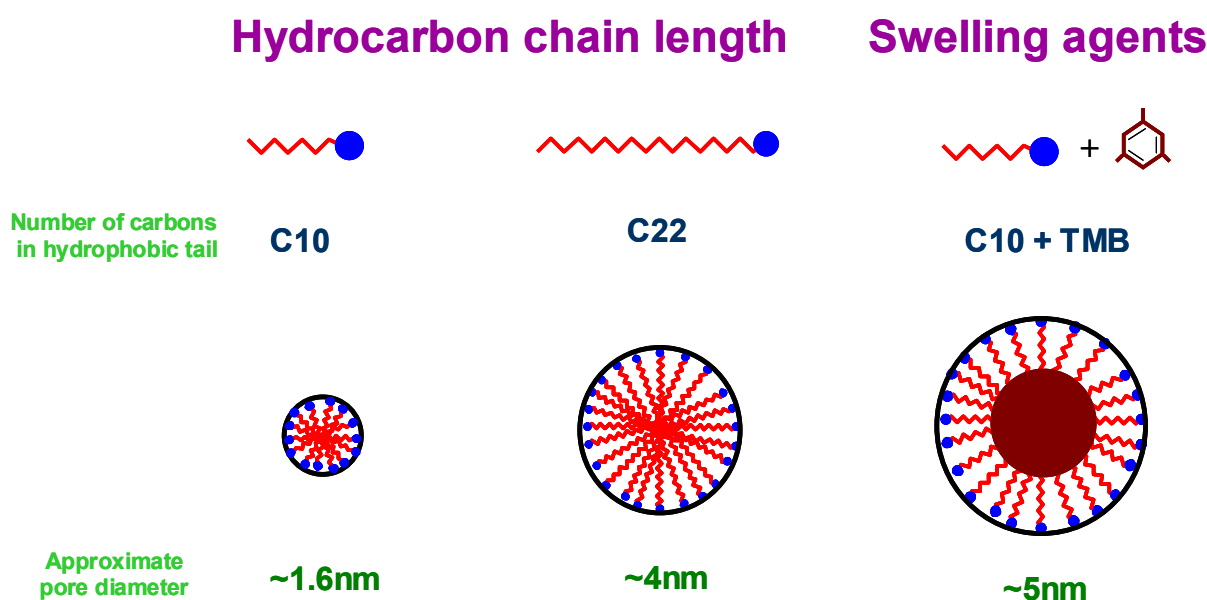
Figure 6. Pore diameter control in MCM-41 materials by applying surfactants with different chain lengths and by addition of swelling agents (TMB: trimethylbenzene)

SBA-15 type materials synthesized from block copolymers

In 1998 Zhao et al. reported the synthesis of a new ordered mesoporous silica (called SBA-15) with hexagonal symmetry and large pores of 4 to 30 nm in diameter.[7, 8] Instead of ionic surfactants, non-ionic block co-polymers were used as templates [Figure 7]. In one molecule ethylene oxide (EO)$_n$ monomer blocks are separated by a block of propylene oxide (PO)$_n$. The hydrophobic core of the micelles formed from such polymers is composed of hydrophobic PO part, while hydrophilic EO blocks are pointing outwards. Such micelles have significantly larger dimensions (4-30 nm diameter) than the ones created from ionic surfactants (1.5-4 nm) [Figure 7]. Typically a block-copolymer with the composition $EO_{70}PO_{20}EO_{70}$ (Pluronic P123) was used: and the resulting material with hexagonal arrangement of pores was called SBA-15.
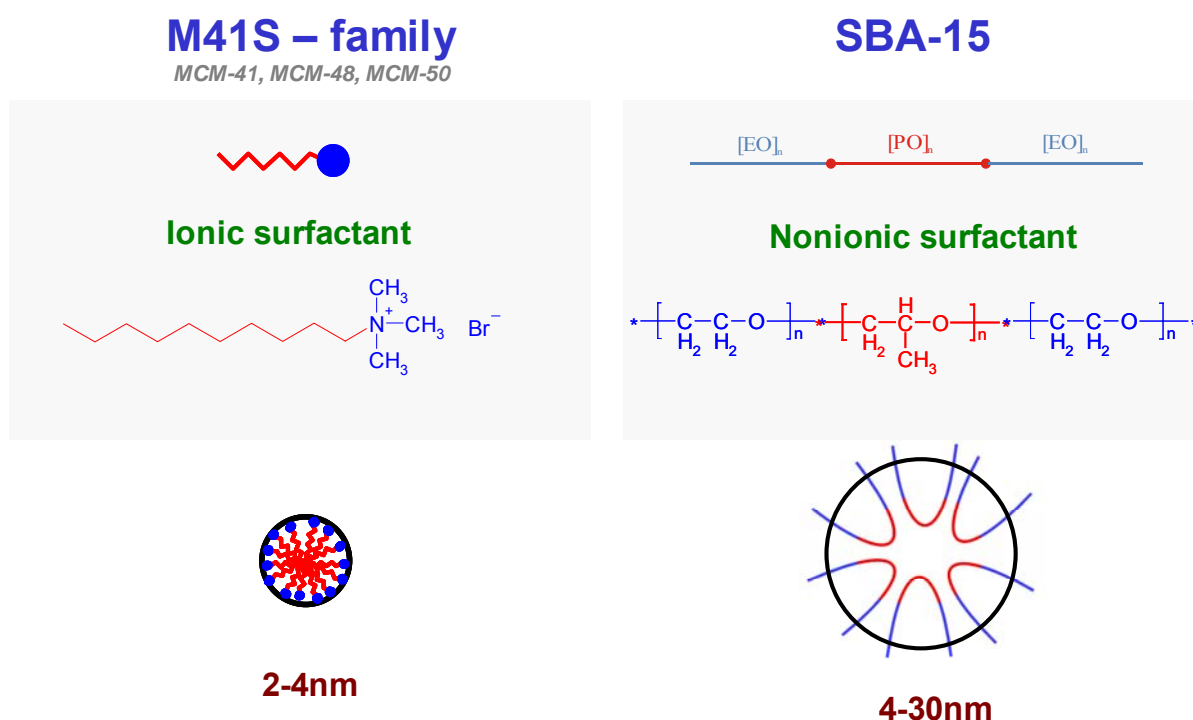
Figure 7. Templating molecules used in M41S family (cationic surfactant) and in SBA-15 (non-ionic block co-polymer) materials syntheses and corresponding shape and size of the micelles.

According to Kleitz et al., one can obtain cubic Ia3d pore symmetry (KIT-6 which is a large pore analog of MCM-48) by adding co-surfactants like n-butanol [56] or cubic, cagelike pores (SBA-16) which were also obtained originally by Zhao by employing F127 ($EO_{106}PO_{70}EO_{106}$) block copolymers.[8] However, beside differences in pore diameter (as compared to M41S family) these materials had also different pore wall structure. As

investigated by Galarneau et. al. block copolymer derived mesoporous silica exhibited significant amount of microporosity.[57] The latter is due to the specific behaviour of non-ionic surfactants.[58]   Non-ionic micelles in water are surrounded by a corona of hydrated polyethylene oxide (PEO), pointing out around 1 nm from the micelle surface.[59] When isotropic micellar solution is formed, the repulsion between opposite combs of hydrated PEO chains separates the micelle to a distance of 3-4 nm [Figure 8]. PEO chains pertaining to adjacent micelles do not share their hydration shells. However, by increasing the temperature, the PEO chain becomes less hydrophilic and withdraws on the micelle surface, and intermicellar attractions arise from PEO-PEO interactions between adjacent micelles [Figure 8].
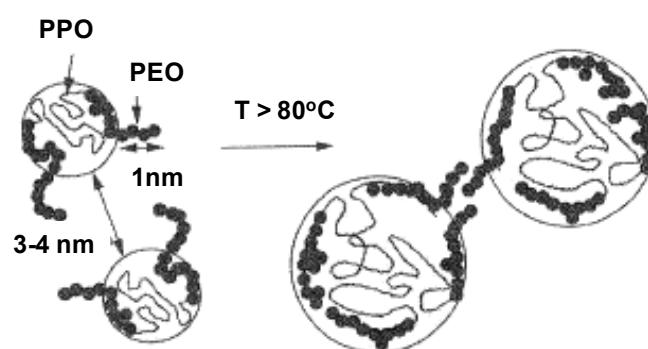
Figure 8. Schematic representation of micelle dehydration upon temperature[57]

The evolution of SBA-15 with the synthesis temperature closely corresponds to this pattern. In all syntheses, the first performed step is a day-long aging at 35 ^{o}C . At this temperature silica triggers the formation of a composite mesophase from the isotropic surfactant solution present in the absence of silica.[60] Ordered mesoporous SBA-15 materials are the result of the restructuring of this precursor formed at low temperature by secondary heat treatment at higher temperatures . In the case of materials synthesized below 60 ^{o}C, there is observed microporosity in the pore walls and a wall thickness of around 4 nm [Figure 9]. If the temperature of treatment is increased to 100 ^{o}C or 130 ^{o}C, the pore size increases (as the micelle diameter increases), and pore wall becomes thinner (2 nm). At the same time, the micropores increase in diameter and form opened connections between the mesopores [Figure 9].[57]
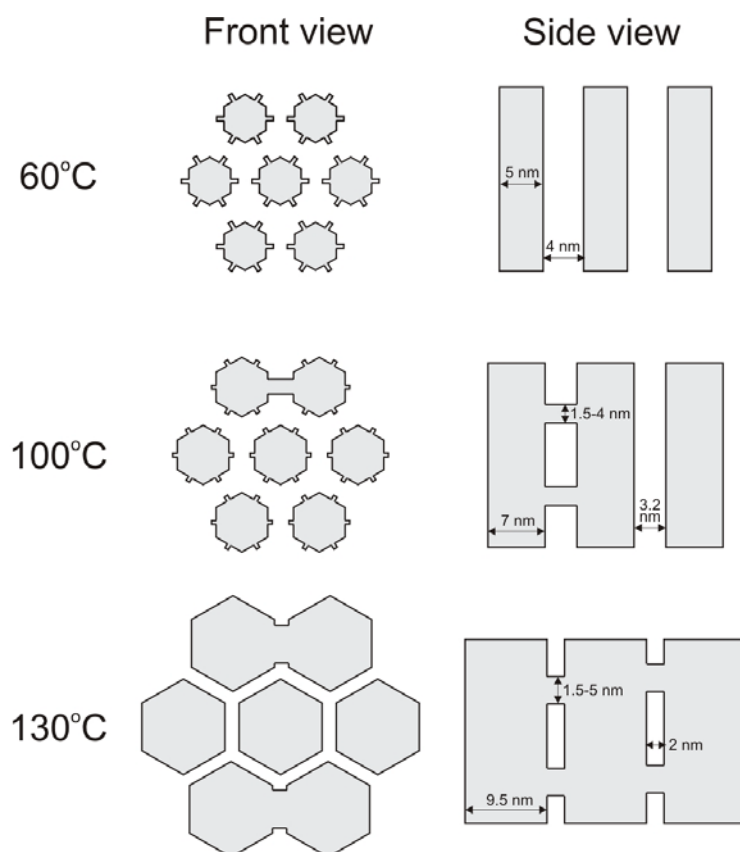
Figure 9. Schematic representation of SBA-15 heat treated at different temperatures[57]

The differences between pore ordering symmetries and pore sizes can be observed ex-situ via low angle X-ray diffraction measurements, nitrogen adsorption [see Chapter 3.1] or transmission electron microscopy. Figure 10 shows two different ordered mesoporous silica materials - MCM-48 with a pore diameter of 2.4 nm and cubic Ia3d pore symmetry, and contrasting SBA-15 with large pores (6 nm in diameter) and hexagonal P6mm symmetry.
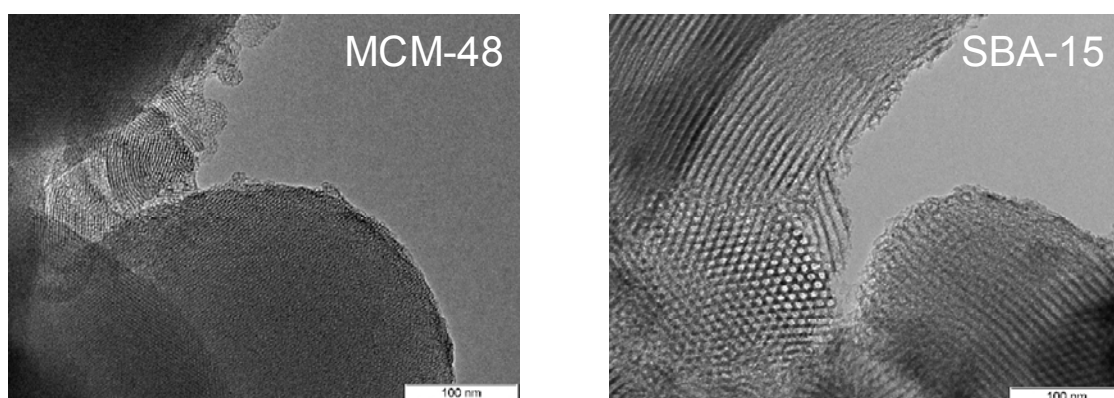
Figure 10. Transmission electron micrographs of cubic small pore MCM-48 and hexagonal large pore SBA-15 materials

In the case of cubic MCM-48, visualization of pores is difficult due to the small pore diameter and non-linear pore geometry. Also, if too high magnifications are used, the high energy electron beam easily destroys this structure. However, in the case of SBA-15 the pores can be viewed along the c-axis [Figure 10 – SBA-15] and larger pores with thicker walls are more resistant to the electron beam.

Non-siliceous oxide mesoporous materials via sol-gel synthesis

The liquid crystal templating and cooperative self assembly mechanism proposed for the preparation of ordered mesoporous silica can also be used to prepare non-siliceous mesostructured materials [Table 1].[9, 10] In this case, to the surfactant solutions instead of silica source (TOES, sodium silicate, …) a precursor of the desired product is added and mesostructured compositions of surfactant with various oxides, phosphates and sulfides are achieved. The first nonsiliceous ordered mesoporous material was synthesized in 1995 by Antonelli et al. (titania)[61] and Ciesla et al. (Zirconium oxo-phosphate).[62] Although in many cases mesostructered materials can be prepared, often upon calcination they lose the ordered mesopore structure.[63] It is due to the low melting temperatures, crystallization processes, phase transformations and redox behaviour of mesostructured material (for example V_2O_5[64] or Fe_2O_3[63]). Another parameter hindering preparation of these materials is fast hydrolysis of most oxide precursors in water medium (alkoxides and chlorides). In such case, deposition of oxides outside of the templating molecules can compete with mesostructure formation mechanisms. In order to overcome this problem another medium that does not react with precursor as vigorously as water can be used. Yang et.al. prepared various mesostructured metal oxides by using metal chlorides ($ZrCl_4$, $TiCl_4$, $NbCl_5$, WCl_6,..) as precursors and pure ethanol as solvent for surfactant molecules.[65] After template removal these materials showed high surface areas (alumina – 300 m^2g^{-1}, ZrO_2 – 150 m^2g^{-1}) and ordered pore arrangement.

Non-oxide materials via the sol-gel synthesis

Non-oxide materials were also synthesized using the surfactant assisted mechanism.[9] Mesostructured chalkogenides (sulfides and selenides) were synthesized using the true liquid crystal templating mechanism. Metal salts in aqueous surfactant solutions were treated with hydrogen sulfide gas, forming sulfides.[66-68] However no ordered mesoporous sulfides were reported until now.

Porous nitrides and imides were prepared by employing alkylamines and alkylimides in non-aqueous medium by ammonia treatment. However, the final material was microporous and disordered.[69] On the other hand, mesoporous silicon nitride can also be prepared from cheap silicon halides without the presence of surfactants. Upon the ammonolysis, ammonium halide nanocrystals are formed and are subsequently removed by calcination in ammonia, causing the porosity of final silicon nitride product. By proper choice of the hydrocarbon and silicon halide, the pore sizes can be adjusted in a similar range as for ordered mesoporous silica. [70, 71]

Mesostructured noble metals were prepared by true liquid crystal templating mechanism by Attard and Goltner.[72] The lyotropic liquid crystalline phase was loaded with the metal precursor ion and reduced with less noble metals or hydrazine. The surfactant was removed by washing in acetone, water and HCl. The pore size was found to be of around 3nm with relatively thick walls, and due to the relatively high density of noble metals, materials with low specific surface areas were obtained (20 m^2g^{-1}).

Table 1. Examples of non-siliceous ordered mesoporous oxide materials synthesized via sol-gel syntheses (mostly based on the review article of Schüth F.)[9]

Composition	Structure
Al_2O_3	H,D
TiO_2	C,H,L, D
Ti-oxophosphate	H,D
ZrO_2	C,H,L,D
Zr-oxophosphte	H
HfO_2	D
V_2O_5	H,L,D
V-P-oxide	C,H,L
Nb_2O_5	H,D
Ta_2O_5	H
MoO_3	L
Mn-oxide	H,L
ReO_2	D
Fe_2O_3	L
CoO	L
NiO	L
ZnO	L
$HznPO_4$	L
Y_2O_3	H,L
Rare earth metal oxides	H,L,D

*C=cubic, H=hexagonal, L=lamellar and D=disordered symmetry of pore ordering. Materials marked in red are synthesized as mesoporous or otherwise as mesostructured.

2.2   Nanocasting of Ordered Mesoporous Materials

In the previous chapter, the synthesis of mesostructured materials by liquid crystal templating was discussed. However, already existing ordered mesoporous hard templates can also be used for the preparation of other ordered mesoporous structures. In 1999, Ryoo et al. showed that mesoporous silica can be used as a matrix for preparing ordered mesoporous carbons.[11] In this procedure sucrose was infiltrated from water solution into the pores, polymerized (in presence of sulfuric acid) and carbonized at 900 $^{\circ}$C to form carbon. After dissolving the silica in aqueous HF solution, an inverse carbon replica of MCM-48 (named CMK-1) or SBA-15 (named CMK-3) can be prepared. CMK materials possess even higher specific surface area (up to 1800 m^{2}g^{-1}) as compared to the matrix (up to 1400 m^{2}g^{-1}). It can be due to the differences in density of both materials and presence of micropores in the walls of ordered mesoporous carbons. However, not all materials are suitable for preparation of ordered inverse carbon replicas. Typically, all cubic 3-dimensional structures can be replicated (MCM-48,[11] KIT-6,[56] and SBA-16[73]) to give ordered carbon materials. In the case of materials with one dimensional pore systems (like MCM-41 and SBA-15) the possibility of carbon replica preparation depends on the mesopore system connectivity through the silica walls. The mesopores in MCM-41 are not connected and therefore no ordered replica can be synthesized (only disordered carbon rods can be achieved)[Figure 11].
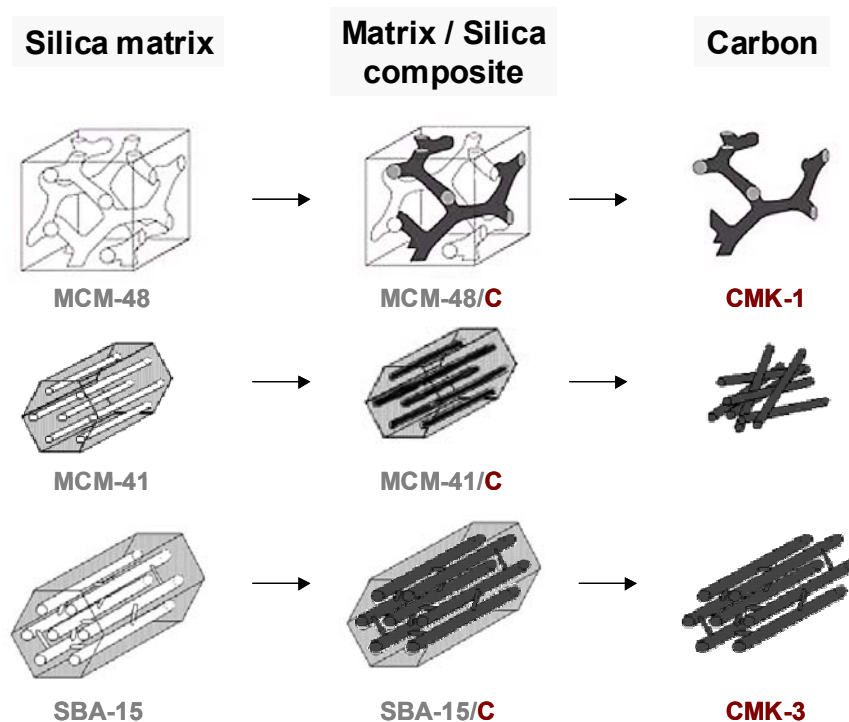
Figure 11. Preparation of carbon replica of ordered mesoporous silica[13]

On the other hand, in the case of SBA-15 (with one dimensional hexagonal pore structure) it is possible to form an inverse replica of this material [Figure 11]. The decisive fact is the presence of microporous connections between the mesopores of SBA-15 synthesized at higher temperatures [see Chapter 2.1]. In the nanocasting process these connections (as well as the mesopores) are filled with carbon and after the removal of silica they connect the rods, synthesized inside the mesopores [Figure 11]. As in the case of MCM-48 and CMK-1, it can be seen that the symmetry of the silica matrix does not always correspond to the symmetry of carbon material prepared from it. This concerns materials with two independent 3-dimensional pore channels, not connected by micropores. Recently Kim et al. showed how the structural transformation of CMK-8 carbon replica takes place when pore connectivity decreases in KIT-6 materials. If one uses KIT-6 prepared at high temperatures (130 ^{o}C – where mesopores are well connected via micropores, as in the case of SBA-15), the carbon replica has the same Ia3d pore symmetry. However, if the temperature of KIT-6 synthesis is decreased (the wall thickness increases and micropores are no longer connecting mesopores), the carbon replica gradually transforms into I4$_1$32 symmetry [Figure 12], typical of CMK-1 materials synthesized from MCM-48.[74]
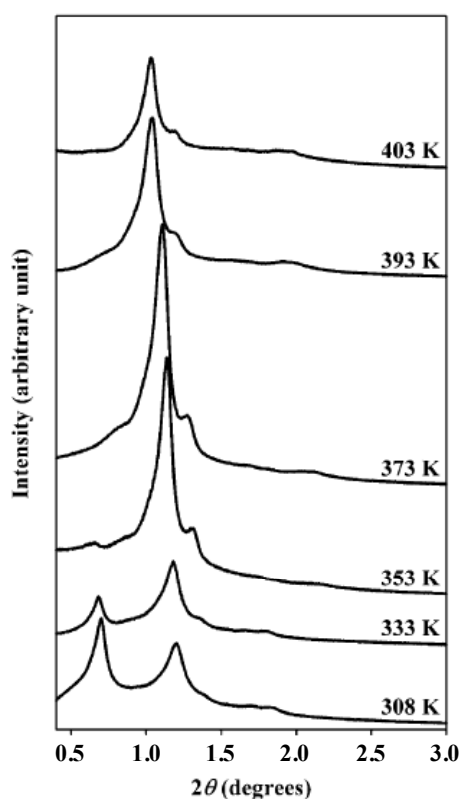
Figure 12. Powder XRD patterns of cubic ordered mesoporous carbons prepared from Ia3d cubic KIT-6 silica synthesized at different temperatures. The sample prepared from silica synthesized at 403 K preserves Ia3d symmetry, while the sample prepared from silica synthesized at 308 K transforms into I4$_1$32[74]

Also oxide inverse replicas of ordered mesoporous silica can be obtained. For example, preparation of mesoporous CeO_2, Co_3O_4 via nanocasting of ordered mesoporous silica was also reported by the Ryoo and Schüth group.

Another important fact is that carbon replicas can be composed not only of the nano-rods, but also synthesis of ordered carbon nanotubes inside the pores of ordered mesoporous silica is possible [Figure 13].[75-77] Such nanotubes possess much higher specific surface areas up to 2200 m^2g^{-1} and can be used for ultrahigh dispersions of noble metal particles. Preparation of nanotubes is achieved by aluminium catalyzed furfuryl alcohol polymerization. The aluminium is first grafted on SBA-15 walls and then furfuryl alcohol is introduced and polymerized in layers on acidic aluminium sites. In the next step, the polymerized alcohol is carbonized at high temperature (900 ^{o}C) and the silica matrix is removed by HF treatment.
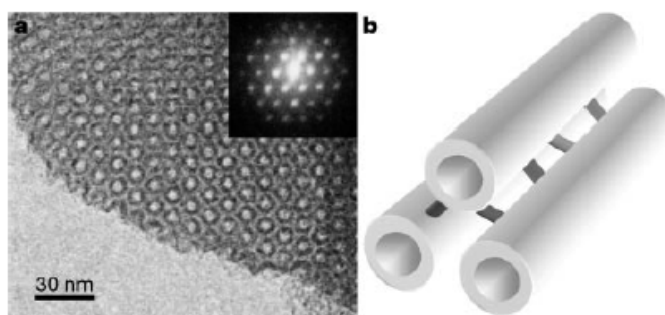
Figure 13. Ordered nanoporous carbon obtained by template synthesis. a) TEM micrograph along the pore b) Schematic model for the carbon structure[75]

Ordered mesoporous carbons can also be used as matrices for preparation of other ordered mesoporous materials. This was demonstrated first by Kang et.al. and Lu et.al., where CMK-3 was used for preparation of ordered mesoporous silica NCS-1.[14, 78] In principle, this approach can also be used for preparation of other oxides (like MgO) and non-oxide materials.[15] Recently, also ordered mesoporous boron nitride ceramics were prepared by infiltration of a preceramic precursor into CMK-3 matrix and its subsequent removal in ammonia flow.[16]

This work investigates preparation of ordered mesoporous silicon carbide using ordered mesoporous silica as template. The used methods included chemical vapor deposition,[20, 21] high temperature autogenic pressure reactions[21] and polycarbosilanes infiltration[22]. Silicon carbide has several interesting properties (hardness, high thermal conductivity and thermal stability – see Chapter 2.4) rendering SiC as a promising support for catalysts.

2.3   Supported Catalysts on Ordered Mesoporous Materials

Pt in ordered mesoporous silica as an example of various preparation techniques

In the previous chapters, preparation of ordered mesoporous materials with silica or carbon composition was discussed. Although silica and carbon materials are relatively inert and do not act as catalysts they are often used as a support for catalytically active species.[3] Preparation of supported materials can be in principle divided into in-situ and ex-situ methods. The differences between both of them are discussed on the example of platinum supported on MCM-41 or SBA-15. In the ex-situ method [Figure 14 – ex-situ] the porous material is first synthesized and then subsequently metal particles (or their precursors) are introduced inside the pores.
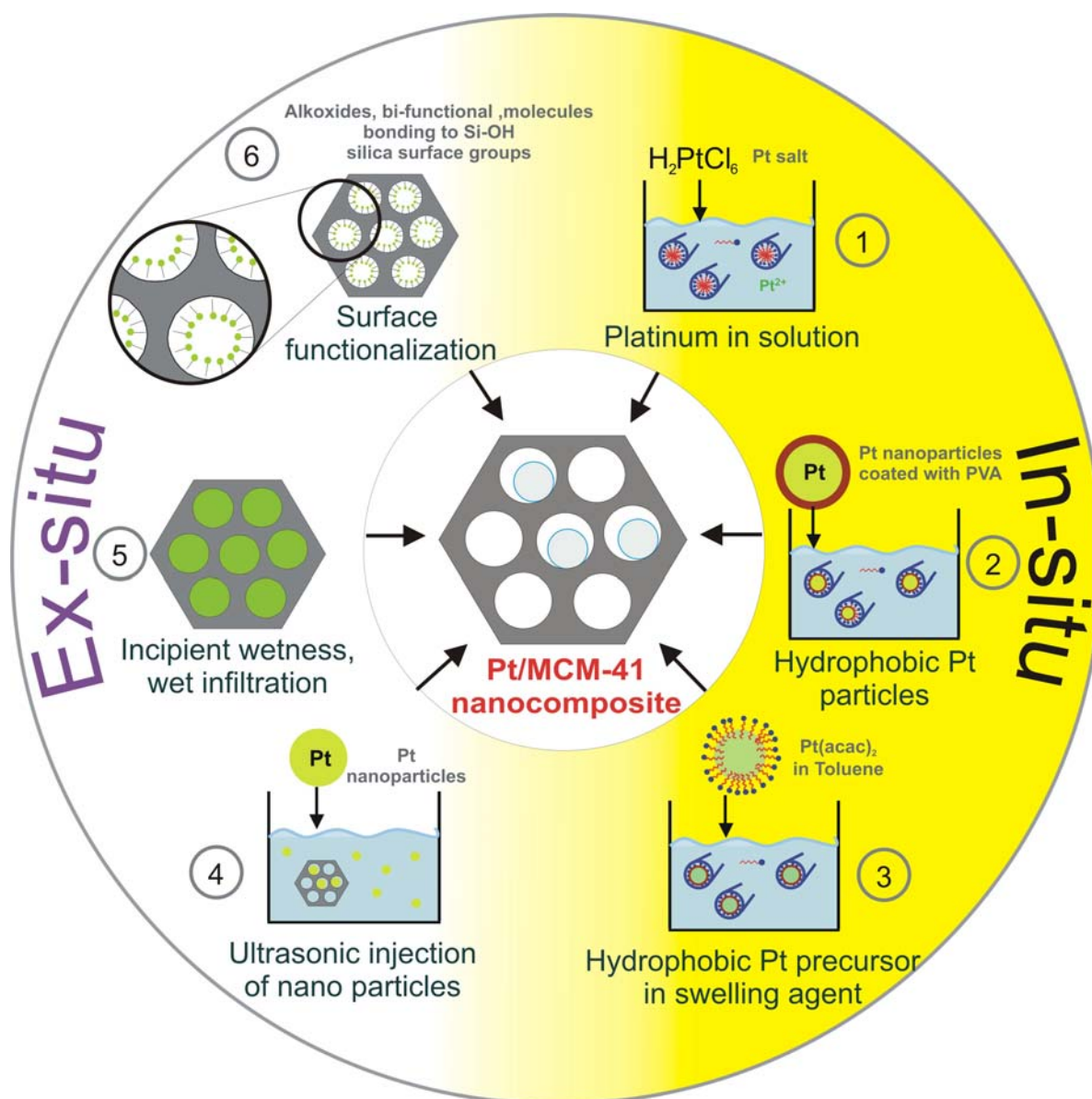
Figure 14. Preparation methods of platinum containing MCM-41 catalysts

This was typically made by the incipient wetness (saturated solution was added in amount which more or less corresponded to the mesopore volume of the material) or wet impregnation (mesoporous material suspended in low concentration solution) [Figure 14 – 5], where solution of metal precursor was introduced on the mesoporous silica powder, followed by solvent removal and reduction of Pt salt or complex to metallic platinum.[79-81] On the other hand, the catalyst could also be introduced by surface functionalization [Figure 14 – 6]. In such case, the catalyst was directly bound to the Si-OH groups on the surface or bi-functional molecules were used (one active group was bound to the Si-OH groups on the surface while the second group acted as catalyst).[82-84] Another chemically active group could also be functionalized already inside the pores via different chemical methods (exchange or chemical reaction). The grafting method allowed to introduce catalytic species exclusively on the pore walls without their deposition outside. Also, direct infiltration by CVD or PVD processes was investigated for the preparation of gold nanoparticles inside mesoporous silica.[85] As prepared platinum nanoparticles with a proper diameter could also be injected by ultrasonication into mesoporous silica [Figure 14 – 4].[86]

As an alternative to ex-situ methods, also in-situ preparations were used [Figure 14 – in-situ]. In this case already during the preparation, platinum or a platinum precursor was introduced [Figure 14 – In-situ]. Typically, water soluble platinum salts could be dissolved in the surfactant solution from which porous silica was prepared [Figure 14 – 1]. However, in this case, low quantities of metal were incorporated and the residues remained in the solution, as well as large particles could be detected outside the pore system.[81, 87, 88] The nanoparticles could also be prepared separately, covered with hydrophobic polymer and injected into the surfactant micelles before addition of silica source [Figure 14 – 2].[89-91] Such process required multiple preparation steps, and already at 1 wt% loading the pore ordering was significantly disturbed. In this work, the possibility of injecting a hydrophobic precursor (like Pt(acac)$_2$) into the micelle core by dissolving in non-polar solvent (toluene) was investigated [Figure 14 – 3]. The main advantage of this method was a high degree of incorporation of the metal (80-100 %), and particles located exclusively inside the MCM pore structure.[27] On the other hand, only limited amounts of the swelling agent could be used, due to the loss of periodicity or phase separation.

As shown in the Figure 14, platinum formed particles or rods inside the pores. However, also coverage of the walls with this metal was possible. Using the same precursor, Yamada el al. showed how the dispersion of platinum could be controlled by applying different temperature/radiation treatments [Figure 15].[92] As expected, in the case of high temperature

aging, nanosized particles with a diameter slightly smaller than the pore diameter were formed [Figure 15 (a)]. However, if instead of the temperature treatment , γ-radiation was used, platinum was uniformly dispersed on the mesoporous silica walls and no larger particles were observed in the pores [Figure 15 (b)].
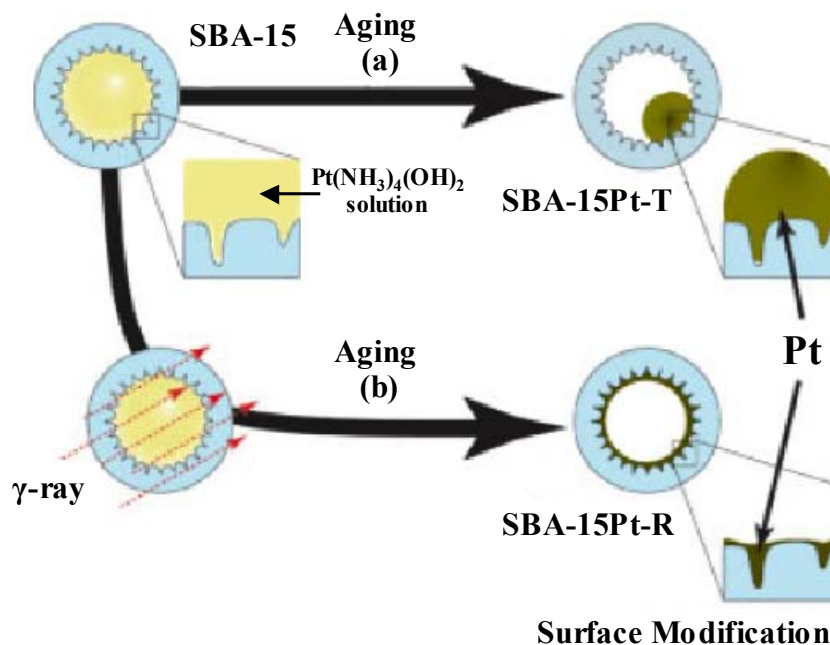
Figure 15 Influence of the postsynthetic treatment on the platinum morphology inside SBA-15. (a) Material is thermally treated and Pt particles are formed, while in (b) material is subjected to γ-radiation covering of SBA-15 walls with a platinum layer is achieved[92]

Metals, metal oxides and metal sulfides particles supported on ordered mesoporous

materials

Ex-situ preparation procedures can be used to support other compounds on the ordered mesoporous materials. Supported metals like Pd, Rh, Au, Co, Ni as well as their alloys, were extensively studied for the heterogeneous oxidation or hydrogenation reactions.[3, 84, 93-99] Metal oxides like ZrO_2, Fe_2O_3, Cs_2O, MgO, Ga_2O_3, In_2O_3, Y_2O_3 as well as heteropoly acids and isoployanions ($W_{10}O_{32}^{4-}$, $Mo_7O_{24}^{6-}$) were successfully supported on the ordered mesoporous silica.[3, 100-104] Interestingly, a change in the phase transformation temperatures can be observed for some of the confined species. For example, tetragonal ZrO_2 is typically transformed into monoclinic ZrO_2 at 450 °C. However, in the case of ZrO_2 materials confined in the SBA-15, no phase transformation was observed, even at 900 °C.[105] The size of the domains has also a large influence on the magnetic properties of compounds. Superparamegnetic Fe_2O_3 was synthesized inside MCM-41 materials[106]. Transition metal

sulfides like WS_2 and MoS_2 were supported on SBA-15 and found to be catalytically active in hydrodesulfurization reactions.[107, 108]

The same approach can be used to support particles on ordered mesoporous carbons. In contrast to silica materials, extraordinary high dispersions of metal were achieved on the nano-pipe structure of the CMK-5 material. Such materials showed superior performance in the O_2 reduction in a fuel cell setup as compared to the standard catalyst.[75]

Highly dispersed species incorporated into the silica network, hybrid materials

Similar to zeolites, ordered mesoporous materials can also incorporate different atoms into the silica framework.[3] Especially incorporation of Al into MCM-41 in order to obtain highly acidic materials was of great interest. Theoretically, such materials could be very useful in the fluidized catalytic cracking catalysis of bulky molecules.[109] However, incorporation of Al atoms into ordered meosporous silica structure yields materials with the low hydrothermal stability and acidity lower than that of the zeolites.[3, 110-112] On the other hand, cracking reactions of bulk molecules under mild conditions and fine chemical syntheses dealing with large molecules were still found to be effective on this kind of materials. Beside Al also other heteroatoms like B, Fe, Ga, Ti, V and Sn can modify the silica wall structure or wall surface.[3] They can be introduced via surface grafting, ion-exchange or during the synthesis via the in-situ procedure. Grafting procedures allow also to fix larger molecules or complexes inside the mesopores.

Ordered mesoporous bioactive glasses with the SiO_2-P_2O_5-CaO composition were prepared by Yan et al.[113-115]. More recently[116] also the group of Stucky reported the synthesis of mesoporous cements showing rapid formation of apatite.

Periodic mesoporous organosilicas (PMOs) can be prepared by co-condesation of functionalized alkoxysilanes in presence of surfactants.[117] The organic functional groups, like methylene, ethylene, phenylene, vinylene or benzene are used.[118-122] After synthesis, templating molecules are typically removed in mild conditions (solvent extraction) in order to avoid burning of organic groups during the high temperature calcinations process.

2.4 Silicon Carbide as a Catalyst Support – Advantages and Properties

Silicon carbide has several interesting properties such as excellent heat conductivity, hardness and high temperature mechanical stability [Table 2].[17] SiC was widely studied as a dense ceramic[123, 124] and used for the preparation of composite materials.[125, 126] Especially the preparation of nano-sized silicon carbide received considerable attention in the context of preparation of bulk materials with increased plasticity[127] or nano-composites with enhanced mechanical and tribological properties.[19] Due to its chemical inertness it was also proposed to be an interesting catalyst support,[18] with unusual high temperature chemical and mechanical stability as compared to other ceramics. Although the stability of high surface area silicon carbide under oxidizing conditions at higher temperatures was found to be low due to the passivation of the surface, under inert conditions the material retained a high surface area for longer duration.[128] Several reports were published, showing that this material effectively competes with conventional supports, such as alumina, silica or activated carbons, especially in exothermic reactions where heat conductivity of the support plays a crucial role.[129-133] However, commercially available silicon carbide has a low specific surface area ($S_g < 25 m^2g^{-1}$) and is not suitable as a catalyst support. Thus, new methods were developed for the preparation of the high surface area materials.

Table 2. Physical properties of silicon carbide compared to alumina and silica

Property	SiO_2 (quartz)	SiO_2 (fused silica)	Al_2O_3	SiC
Thermal conductivity $(W\ m^{-1}K^{-1})$	1.4	1.3	16-30	100-200
Thermal expansion coefficient $(10^{-6}\ K^{-1})$	12.3	0.4	7.2	3.7-4.7
Dielectric constant (at 1Mhz)	-	3.8	9.7	40
Density $(g\ cm^{-3})$	2.65	2.20	3.97	3.20
Melting point (K)	1720-1830	1720-1830	2054	2700
Young modulus (GPa)	70	73	340-410	300-450

One of the first procedures for the manufacture of carbide materials with surface areas up to 200 m^2g^{-1} was "shape memory synthesis". High surface area activated carbon was reacted with silicon monoxide (SiO) at elevated temperatures for the synthesis of silicon carbide.[129] Reduction of high surface area silica with carbon precursors also gave high surface area silicon carbide materials. An example was the reduction of high surface area silica aerogels with carbon precursors for the production of materials with a specific surface area of 112 m^2g^{-1}.[134] The same idea of reacting silicon and carbon was used to prepare silicon carbide

from ordered mesoporous materials, but in this case, surface areas did not exceed 160 m^2g^{-1}.[135-137] Decomposition of simple silane precursors at low pressures was used for the manufacture of SiC with a surface area of 50 m^2g^{-1}[132] or at high autogenic pressures 146 m^2g^{-1} was achieved.[138] Chemical vapor deposition (CVD) and chemical vapor infiltration (CVI) were also used for the impregnation of ordered porous hosts in order to control the size of the deposited domains.[139-141] The thesis shows that silicon carbide was directly deposited inside the MCM-48 and SBA-15 by CVI.[20] CVI allowed to use simple and inexpensive precursors and gave good control of the product composition.[142] After HF treatment of SiC/SBA-15 composite materials, high surface area (410-830 m^2g^{-1}) mesoporous SiC was obtained.[20, 21] However, low angle X-ray measurements suggested no mesoscopic ordering of the pore structure. Well-ordered SiC structures were prepared by vapor/liquid condensation/infiltration with melted low molecular weight polycarbosilanes[22] or by organic solvent assisted process from polycarbosilanes with higher molecular weights.[143]

2.5 Transition Metal Nitrides and Carbides - Alternative to Noble Metal Catalysts

Transition metal nitrides and carbides have been studied intensively as electronic and structural ceramics.[144-146] Compared to oxides they have superior properties in some respects such as hardness, mechanical strength and high melting points (the melting point of V_2O_5 is 690 °C while for VN and VC it is 2050 and 2810 °C).[144] As shown in the pioneering work of Levy and Boudart[23] and, more recently, summarized by Oyama,[24, 147] transition metal nitrides and carbides can also be efficient catalysts. In particular, compounds such as W_2N or Mo_2N have attracted attention as catalysts for hydrotreating reactions.[148-150] In oxidation, hydrogenation or isomerization reactions, the catalytic properties of the transition metal nitrides and carbides resemble those of group VIII noble metals [Figure 16].[23, 147] Thus, transition metal nitrides and carbides may offer a promising economic alternative to conventional noble metal catalysts.
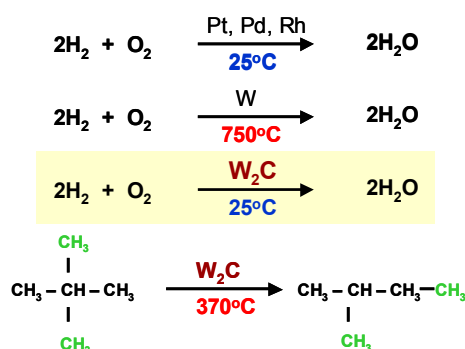
Figure 16. Transition metal carbides exhibit similar properties as group VIII metals: reacting hydrogen with oxygen (chemisorbed on the surface of carbide) at room temperature as well as showing activity in isomerization reactions[23]

In some reactions, nitrides and carbides show not only higher resistance against poisoning as compared to noble metals, but also comparable specific reaction rates.[24] Kwon et al. showed that similar dehydrogenation rates of n-butane can be measured over high surface area vanadium nitride and a standard supported Pt-Sn catalyst [Figure 17].[151]

Catalyst	Specific surface area [m^2 g^{-1}]	Specific reaction rate [nmol g^{-1} s^{-1}]
VN	29	166
VN	59	253
Pt-Sn/Al$_2$O$_3$	228	350
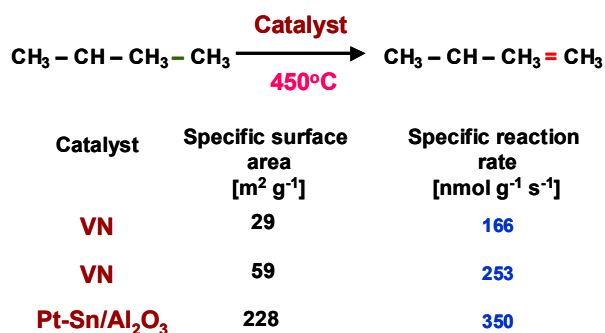
Figure 17. n-Butane dehydrogenation over vanadium nitride and Pt-Sn catalyst[151]

The dehydrogenation activity of the vanadium nitride catalyst clearly increases with the measured specific surface area [Figure 17],[151] therefore a key issue for improving this class of materials is the development of synthesis methods producing materials with high surface areas and particle sizes in the nanometer range.[37, 152] Nanoparticles (d < 100 nm) are also crucial in the preparation of dense materials, since they allow rapid densification at temperatures lower than required for micrometer-sized powders, and yield materials with enhanced plastic or superplastic properties.[127, 153, 154]

Until now, molybdenum oxynitride was the only material (among transition metal carbides and nitrides) applied commercially as catalyst. It is used in the space industry as a catalyst for hydrazine decomposition for microthrusters correcting the satellite orbit[Figure 18].[155]
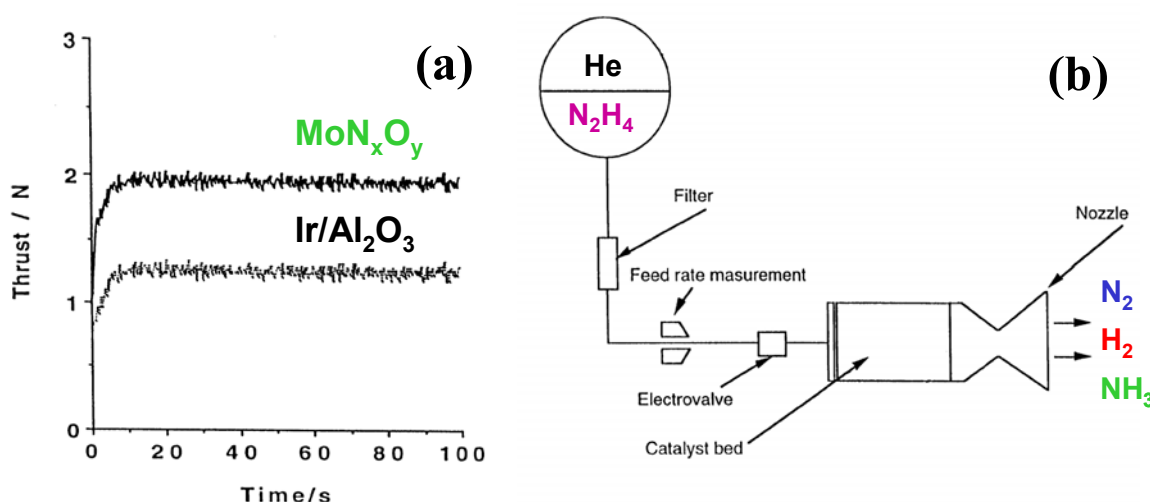
Figure 18 (a) MoO_xN_x as an effective catalyst for hydrazine decomposition (b) Schematic drawing of the microthruster used in satellites for orbit corrections[155]

A common method for the preparation of high surface area transition metal nitrides and carbides is nitridation of the corresponding oxides with ammonia (or mixture of H_2/N_2) or carbonization with CH_4/H_2 gas mixture.[26, 156] Typically, extremely high gas flow and high gas purity is required in order to obtain the high surface area material. The presence of water as an impurity or as a reaction product (due to too low gas flow) suppresses the reaction and causes sintering effects. Therefore, high surface area nitrides like VN are prepared in extremely high ammonia flows (for example VN with 90 m^2g^{-1} can be prepared from V_2O_5 with 19 m^2g^{-1} under 1300 h^{-1} of molar space velocity of ammonia).[26] Surface areas up to 150 m^2g^{-1} for other nitrides like Mo_2N and W_2N were reported.[24] Prestructured precursors (vanadium oxide aerogel) and even higher ammonia space velocities (1870 h^{-1}) allowed to prepare VN with even higher surface area of 120 m^2g^{-1}.[157]

Transition metal nitrides and carbides tend to react on the surface with oxygen present in the air and form a passivation layer. This is extremely important in the case of high surface area materials. Due to small particle size and large external surface area such materials can oxidize in bulk rapidly if directly exposed to air.[158] Therefore, a passivation in inert gas containing low oxygen amounts (~1%) is necessary before exposing to air. For example, high surface area Mo_2N ($150m^2g^{-1}$)when exposed to air without passivation, oxidizes immediately (is pyrophoric).

Also supports like zeolites, high surface area alumina and silica were used for the preparation of highly dispersed molybdenum nitride and carbide.[24, 159, 160] The thesis shows how vanadium nitride and carbide catalysts can be supported on ordered mesosporous silica and activated carbon. Amine intercalated oxide was also demonstrated to be a useful precursor for the preparation of vanadium nitride with surface areas up to 190 m^2g^{-1} under orders of magnitude lower ammonia flows.[25] Moreover, supported and foam-derived high surface area vanadium nitride catalysts showed significantly higher conversions and selectivities in propane dehydrogenation as compared to low surface area VN materials (prepared via direct V_2O_5 nitridation).

3. Methods and Experimental Details

3.1. Gas Adsorption on Solids as a Tool for the Characterization of Porous Materials

The interactions between a gas and a solid are divided into two groups. Reaction of both phases can take place and a new chemical compound is formed (Figure 19 Generic/Absorption). On the other hand, also adsorption interactions only on the phase boundary can take place and these are divided into physisorption and chemisorption.[161] Depending on the nature of the bond formed between the adsorbed gas molecule and the solid, both phenomena are arbitrarily distinguished (based on the enthalpy of adsorption). In the case of physisorption, weak physical interactions between adsorbate molecules and adsorbent exist and such phenomena are typically studied at temperatures close to the boiling point of the adsorbate. Characteristic of physisorption is the formation of multilayers of the adsorbate on the surface. However, in the case of chemisorption (which is typically investigated at higher temperatures), only one strongly bonded monolayer of adsorbate is formed. These two processes are used to estimate various properties of solids with high specific surface areas. Physisorption measurements are typically used in heterogeneous catalysis to determine the specific surface area, pore size distribution and pore volume of catalysts, while chemisorption of selected gas molecules allows to determine the dispersion of the active phase and nature of the active sites.
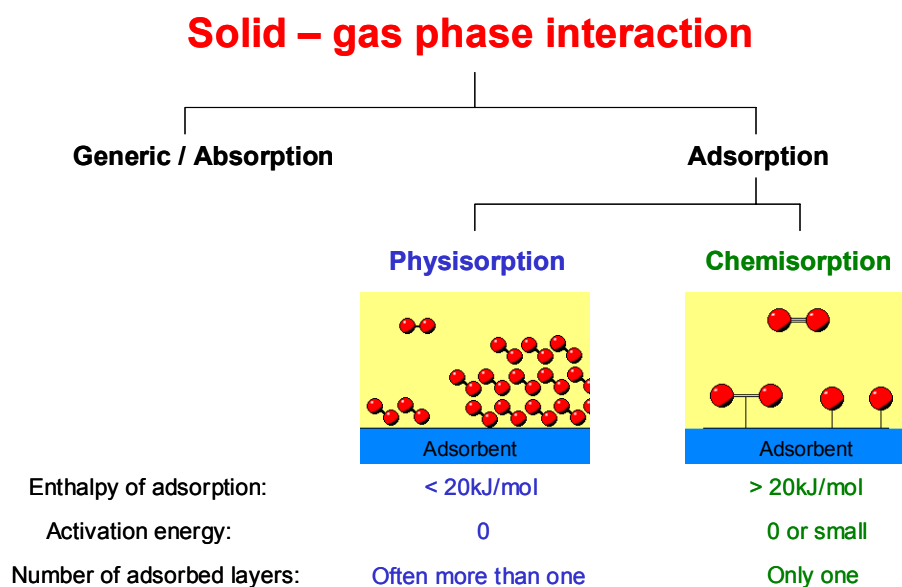
Figure 19 Classification of gas – solid interactions

3.1.1 Nitrogen Physisorption at 77K

The most common technique to characterize high surface area meso- and microporous materials is physisorption of nitrogen at liquid nitrogen temperature. It allows precise, non-destructive analysis of porous materials. However, there are some limitations for nitrogen as an adsorbate, due to the large dimensions (kinetic diameter of 3.64 Å) especially in characterization of the microporous materials, but in such cases other gas molecules like argon (kinetic diameter of 3.41 Å) can be used for characterization. Typically, the sample is evacuated before measurement, cooled down to 77K and then, known amounts of nitrogen gas are dosed. Each dose is followed by pressure measurements in the sample cell. The recorded dose volume as a function of pressure in sample cell at constant temperature is called adsorption isotherm. Depending on which material adsorption takes place, different shapes of isotherms are obtained [Chapter 3.1.3]. Typical process of nitrogen adsorption (and corresponding isotherms) at different stages for mesoporous MCM-41 material is shown in Figure 20.
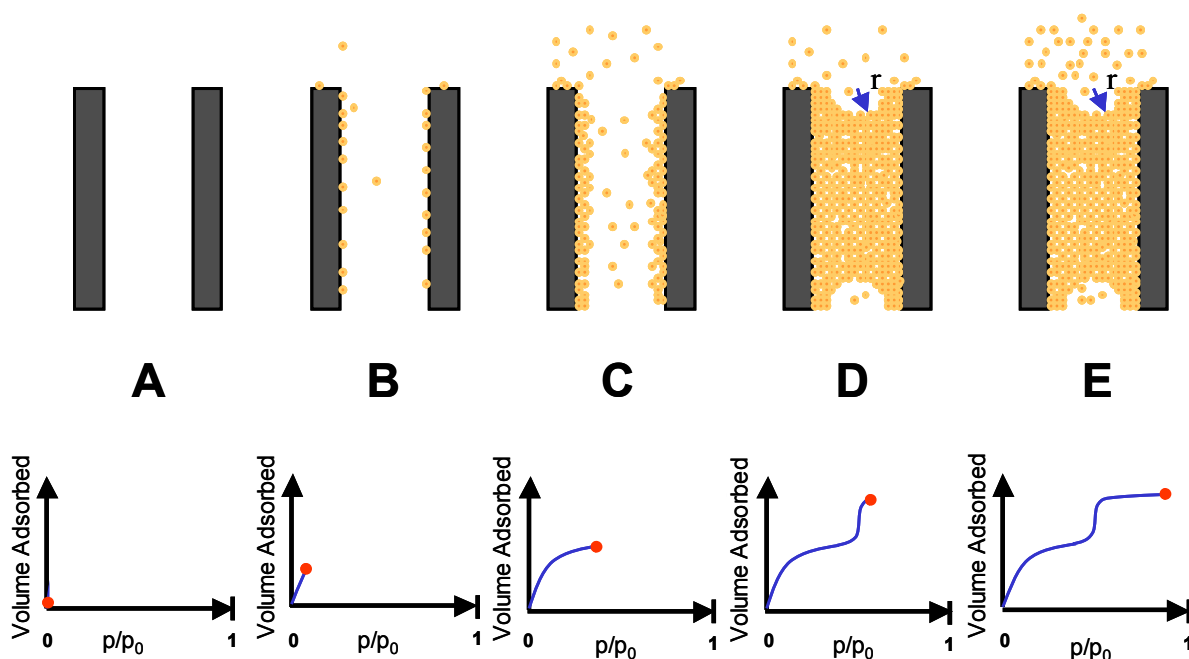
Figure 20. Nitrogen adsorption on the ordered mesoporous silica MCM-41 at 77K with isotherm shape corresponding to each adsorption step. Y axis: volume of nitrogen adsorbed, X-axis: relative N_2 pressure, where p is the N_2 pressure measured in cell and p_o is the saturation pressure of N_2 at 77K.

The first dose is made to the sample evacuated before (Figure 20A) and all nitrogen delivered is adsorbed on the surface (Figure 20B - the pressure remains almost at the vacuum level). In the next dose the surface coverage with adsorbate increases, multilayers are formed

and finally, due to higher desorption rate, also the pressure measured in the cell increases. Since each following multilayer is bound weaker, even small amounts of nitrogen dosed stay preferentially in the gas phase causing a significant increase of pressure (Figure 20C). The area of isotherms where multilayer adsorption took place (from 0.05 to 0.3 of relative pressure P/Po) is suitable for calculation of specific surface area based on the BET theory (chapter 3.1.4). In the next step, a meniscus is formed and capillary condensation takes place (chapter 3.1.2), consuming nitrogen to form a liquid phase in the pores. As much of nitrogen is dosed as necessary to fill the pore volume (Figure 20D) and further doses cause significant increase of the measured pressure (Figure 20E).

3.1.2 Capillary Condensation and Kelvin Equation

The relative pressure at which capillary condensation takes place is dependent on the pore size. The smaller the pore the lower pressure is required for the capillary condensation. The pressure at which capillary condensation takes place for a given meniscus radius (which was proportional to the pore radius), can be calculated from the Kelvin equation (eq.1, Figure 21).

$$\ln \frac{p}{p_0} = \frac{-2\gamma V_M}{rRT} \cos\varphi \tag{1}$$

Where p/p_o is the relative pressure of adsorbate (p – pressure of adsorbate measured in sample cell, po – saturation pressure of adsorbate); V_M - molar volume of the liquid adsorbate; R - universal gas constant; T – temperature; r - meniscus radius; φ – wetting angle (Figure 21)
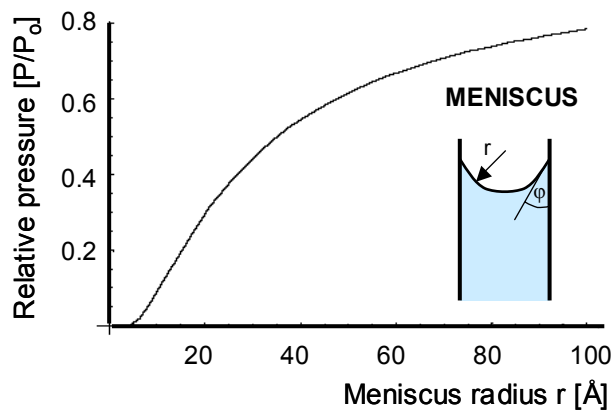
Figure 21. Graphical plot of Kelvin equation (eq. 1) for nitrogen at 77K.[45]

However for the estimation of the pore diameter (eq. 2 - d_{pore}), not only the diameter of the meniscus has to be known (eq. 2 – $d_{meniscus}$), but also the thickness of already existing

multilayer of the physisorbed adsorbate (eq. 2 - t) on which the meniscus is formed (eq. 1, Figure 22). It is calculated from the multilayer adsorption theory discussed in chapter 3.1.4. This pore size calculation method was proposed by Barrett, Joyner and Halenda and is known as BJH theory.[162]

$$d_{pore} = d_{meniscus} + 2t \qquad (2)$$

Where d_{pore} – pore diameter; $d_{meniscus}$ – meniscus diameter calculated from Kelvin eqation (eq. 1); t – adsorbate multilayer thickness calculated from the BET equation (Chapter 3.1.4) by dividing the multilayer volume (V) by the volume of monolayer (V_{max}) and multiplying by effective height parameter (eg. σ = 3.6 Å for hexagonal and 4.3 Å for cubic nitrogen molecular packing).

$$t = \frac{V}{V_{max}} \sigma \qquad (3)$$

The film thickness can alternatively be calculated from the Wheeler equation for nitrogen at 77K.[45]

$$t = 4.3 \left(\frac{5}{\ln(p_o / p)} \right)^{1/3} \qquad (4)$$

Multilayer thickness - t   Meniscus diameter - $d_{meniscus}$
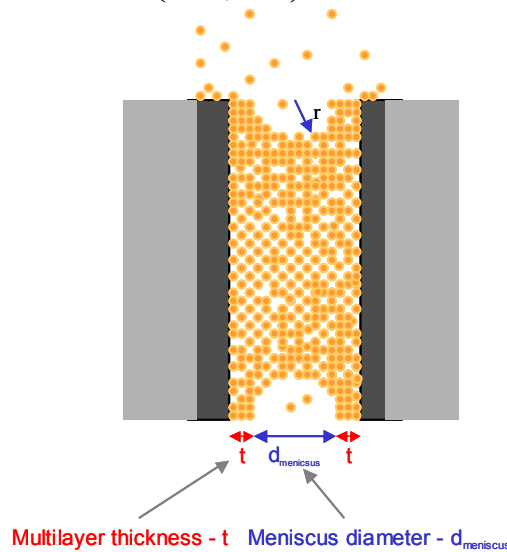
Figure 22. Pore size calculation according to the BJH theory.[45, 162]

The Kelvin equation cannot be applied to microporous materials since formation of a meniscus is not reasonable in such small pores. Also, condensation in the micropores takes place at much lower pressure due to the overlapping of the Lennard-Jones potentials from the opposite sides of the pore walls creating low energy minimum.

3.1.3   Isotherm Classification According to IUPAC

Adsorption isotherms are classified by IUPAC into six types.[161] Type I is that of the microporous materials. Maximum gas uptake can be observed at already very low pressures due to condensation in the pores and a plateau is reached. Type II isotherms are those of non-porous substances like powders, with high specific surface area. At low pressures, multilayers of adsorbate are formed on the surface, while at higher pressures some condensation due to the interparticular porosity takes place. In the case of Type III isotherms there is a weak interaction between adsorbate and adsorbent compound and only at higher relative pressures condensation in form of multilayers on the surface can be observed. Type IV isotherm which is typical of mesoporous materials, consists of a low pressure area where multilayers of adsorbate are formed, followed by capillary condensation (with a steep slope of the curve). If, for the same material, weak interaction between adsorbate and adsorbent is present, the shape of the isotherm at lower pressures is changed similarly to that of Type II isotherm. On the other hand if a porous material has bi- or tri-modal pore size distribution, Type VI isotherm, with multiple steps, can be observed. The steps can also be caused by the interactions or structural changes in the material when different pressures are applied.
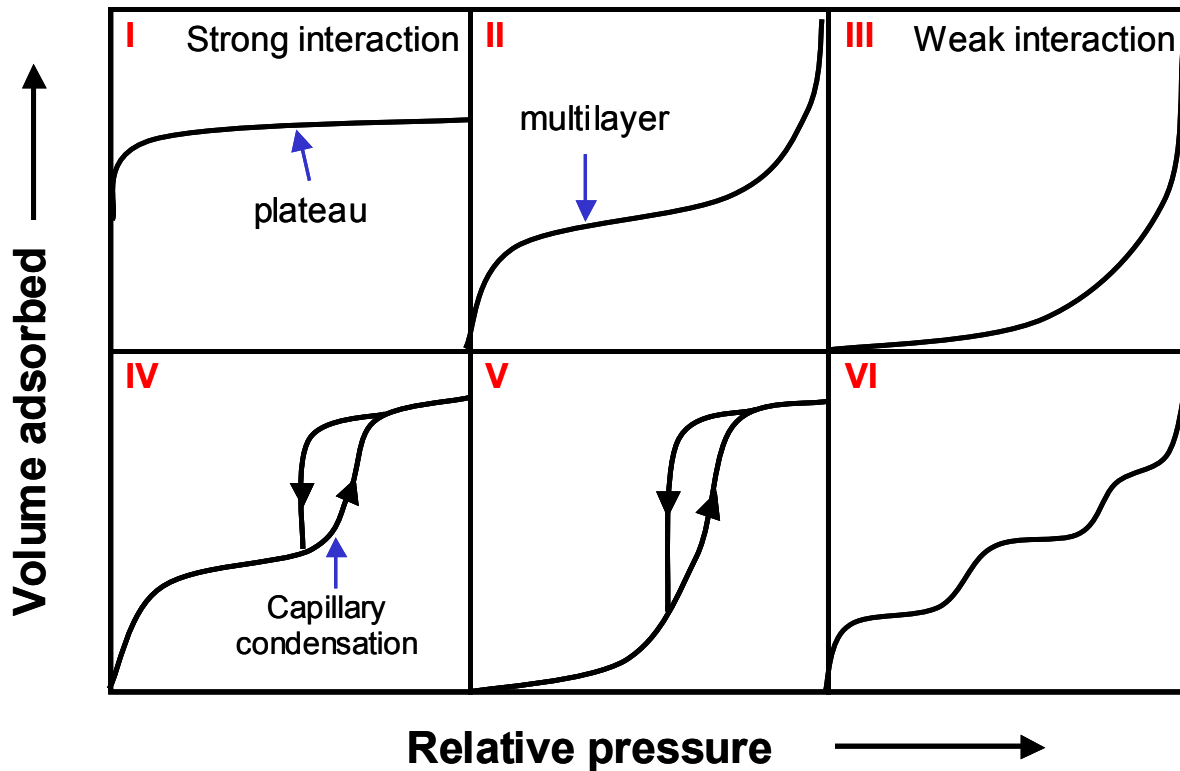
Figure 23. IUPAC classification of the adsorption isotherms[161]

Typically, not only adsorption, but also desorption of the adsorbate is measured. The desorption branch can follow exactly the adsorption or hysteresis loop is observed (desorption starts at lower pressures than adsorption). This depends on the nature of the adsorbent (in the case of nitrogen adsorption at 77K a hysteresis loop is always observed for capillary condensation steps at pressures higher than P/Po = 0.42) as well as on the shape of the pore or presence of particles in the pore system. If the pores are well defined with a uniform diameter, the desorption branch is shifted to slightly lower pressures as compared to the adsorption branch (H_1 type of hysteresis loop – Figure 24 - typical of large pore ordered mesoporous silica SBA-15). If the pore size distribution is broad, or the pores are blocked with particles or with a bottle-neck like geometry, the hysteresis loop becomes broader (H_2 type - Figure 24). H_3 loops are typically measured for the aggregates of platy particles or adsorbents containing slit-shape pores (mesoporous activated carbons). On the other hand, H_4 loops are also characteristic of the slit-shape pores as in many activated carbons consisting mainly of micropores. The desorption branch should meet adsorption branch at the closure point. This depends on the adsorbate and the temperature of the measurement (for nitrogen adsorption at 77K the lower closure point is located at P/Po = 0.42). If the hysteresis loop does not close at the specified point, the sample was not outgassed properly before the measurement, or sublimed or alternatively adsorbate molecules were trapped inside the flexible pore structure.
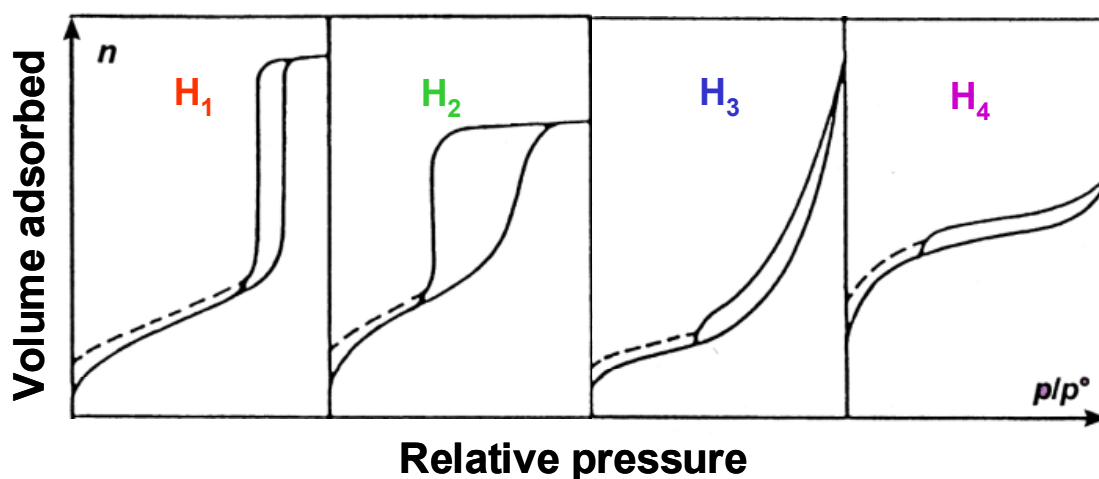
Figure 24. IUPAC classification of the hysteresis loops[161]

3.1.4 Specific Surface Area Estimation: Langmuir and BET Theory

In 1918 Langmuir presented a theory and mathematical description of gas adsorption on solid surface.[163] The kinetic derivation has the following assumptions:

- only a monolayer adsorption of adsorbate on adsorbent takes placeall adsorption sites have the same energy ($\Delta H_{chem.}$ - Figure 25a)

- there is zero or one molecule at each site and no interaction between adsorbed molecules

The Langmuir equation was derived as a dynamic equilibrium equation (equilibrium between the rate of adsorption and desorption) and shows how the coverage of the surface with adsorbate changes with pressure (eq. 5, Figure 25a). The same equation can also be presented in linear form, typically used for the calculation of monolayer volume (eq. 6)

$$\Theta = \frac{k_{ads}p}{k_{ads}p + k_{des}} \tag{5}$$

$$\frac{p}{V} = \frac{p \cdot k_{ads}}{k_{des} \cdot V_{max}} + \frac{k_{des}}{k_{ads}V_{max}} \tag{6}$$

Where θ is surface coverage (could be represented as ratio of volume of adsorbate (V) to the volume of monolayer (V_{max}) ; p = gas pressure; k_{ads} = gas adsorption rate; k_{des} = adsorbate desorption rate.
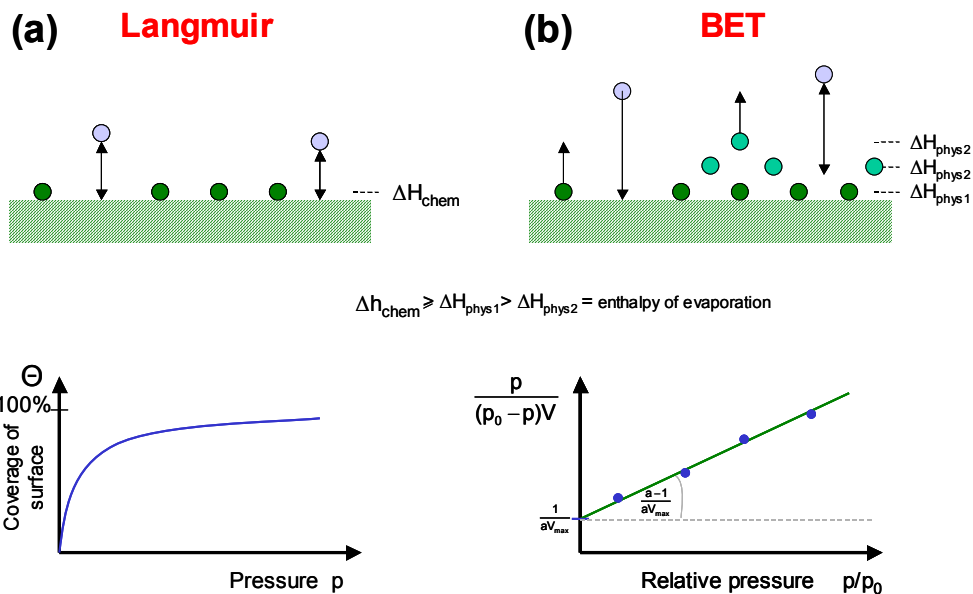
Figure 25. (a) Monolayer surface coverage (where ΔH_{chem} is the enthalpy of adsorption) and graphical plot of Langmuir equation (eq. 5). (b) Multilayer formation (first layer has higher adsorption energy than the following layers $\Delta H_{phys1} > \Delta H_{phys2}$) and graphical plot of BET equation (eq. 7)

Since monolayer formation is assumed, typically such equation should not be used for the estimation of surface area if the adsorbate is physisorbed and multilayers are formed. The

Langmuir estimation of surface area is sometimes used in the case of microporous materials, if the pores are too small to allow the formation of multilayers of the adsorbate. The Langmuir model is also widely applied for the description of chemisorption of gas molecules. In that case, typically only monolayer formation of adsorbate takes place and additional physisorption effects leading to multilayer formation are weak and can be neglected or extracted by secondary measurements.

Brunauer, Emmet and Teller (BET) presented in 1938 a new theory describing multilayer adsorption of gas molecules on solids.[164] The basic assumptions are as follows:

- infinite number of layers are formed
- the first layer is adsorbed stronger than the others ($\Delta H_{phys1} > \Delta H_{phys2}$)

The BET theory is a standard tool to calculate specific surface areas of solids via physisorption of gases. Typically the BET equation is presented in its linear form (eq. 7, Figure 25b):

$$\frac{p}{(p_0 - p)V} = \frac{1}{aV_{max}} + \frac{a-1}{aV_{max}}\frac{p}{p_0} \tag{7}$$

Where p is gas pressure; p_0 = saturation pressure of gas at given temp; V = volume of multilayer adsorbed; V_{max} = volume of monolayer; a = constant

If true multilayer physisorption takes place, the measured points on the BET plot should fit a line. However, there may be deviations, due to the presence of microporosity or capillary condensation in small mesopores. Therefore, the points for which the calculation is made should be chosen carefully in the linear range. It is recommended to use ranges between p/p_0 = 0.05-0.3 in the case of nitrogen physisorption at 77K.[161] If the material has small mesopores for which capillary condensation takes place in this range, the upper pressure range has to be excluded, so that exclusively the linear part of the BET plot is taken into account. If only one measurement point is available, the so called "single point" BET equation can be applied. In this simplified form linear equation is assumed to cross the origin point of the coordinate system and the $(aV_{max})^{-1}$ term equals zero. Such method is often used in the case of a flow adsorption apparatus with defined gas mixtures. For example, in the case of nitrogen physisorption at 77K, the flowing mixture of 30%N_2 with 70%He can be used and thermal conductivity detector connected to the integrator determines how much nitrogen is adsorbed at p/p_0 = 0.3 point. For a detailed calculation of a specific surface area, the surface area and volume occupied by a single gas molecule adsorbed has to be known. From this data and monolayer capacity (V_{max}) calculated from the BET equation, specific surface area is estimated. With the Langmuir method the known volume of monolayer (V_{max}) can be directly obtained from a linear form of the Langmuir equation (eq. 6).

3.1.5   Statistical Thickness "t-Plot" Method

The statistical thickness method is a tool for the estimation of pore volume as well as of the specific surface area. The generalized equation was derived by De Boer (eq. 8, Figure 26A).[161, 165]

$$t = \left[\frac{A}{\log(p_0/p) + B} \right]^C \tag{8}$$

Where t was statistical thickness; p = gas pressure; p_0 = saturation pressure of gas at given temp; A,B,C = constants

The A,B,C parameters of Equation 8 are optimized by fitting of the isotherms of the non-porous standard. Such fitting is characteristic for a given adsorbent and adsorbate system (for example N_2 on silica). In 't-plot', the statistical thickness (t) is located on the x-axis while the y-axis represents the gas volume adsorbed. If the material is non-porous the 't-plot' function is linear and starts from the origin [Figure 26A]. Materials with higher surface areas require more nitrogen to be adsorbed (the slope of 't-plot' is high) in order to obtain the same statistical thickness as for the materials with low surface area (the slope of 't-plot' is small). The main advantage of this method is the possibility of the pore volume estimation. For microporous materials (with type I adsorption isotherm), the micropore volume estimation is typically made for the volume of adsorbate physisorbed at p/p_o = 0.2 (in the case of N_2 adsorption at 77K). In the case of the 't-plot' method, the linear function is fitted to the part where the 't-plot' is linear [Figure 26B]. From the point where this line crosses the y-axis, the volume of nitrogen adsorbed in the micropores can be calculated. Such method allows to exclude the amounts of nitrogen forming multilayers outside the micropores. One should also remember that the volume of nitrogen given on the y-axis is that of gas at room temperature and therefore has to be converted to the volume of liquid nitrogen at 77K for the estimation of the specific micropore volume. In the case of a mesoporous material with Type IV isotherm the 't-plot' can be used to distinguish the mesopore and micropore volume [Figure 26C]. If the material is mesoporous, the 't-plot' starts from the origin of the axial system and maintains a linear form until the capillary condensation step takes place (deviation from linearity). After the capillary condensation step, the 't-plot' should become linear again as the multilayer adsorption takes place outside the filled pores. From the line fitting after the capillary condensation step [Figure 26C – Fit2] one can estimate the mesopore volume on the y-axis. From the angles at which both fitted lines cross the x-axis, the specific surface areas inside [Figure 26C – Fit-1] and outside [Figure 26C- Fit-2] the mesopores are estimated. Thus, the 't-

plot' method allows to distinguish the micro- and mesopore volume. If the mesoporous sample has additional micropores (as in the case of ordered mesoporous silica SBA-15), the first linear fitting of the 't-plot' [Figure 26C – Fit-1] intersects the y-axis above the zero point and indicates the volume of micropores. Therefore, in such case the mesopore volume measured by Fit-2 is in reality the sum of meso- and micropore volumes (measured by Fit-1). The true mesopore volume is then a difference between volume estimated by Fit-1 and Fit-2 [Figure 26C].
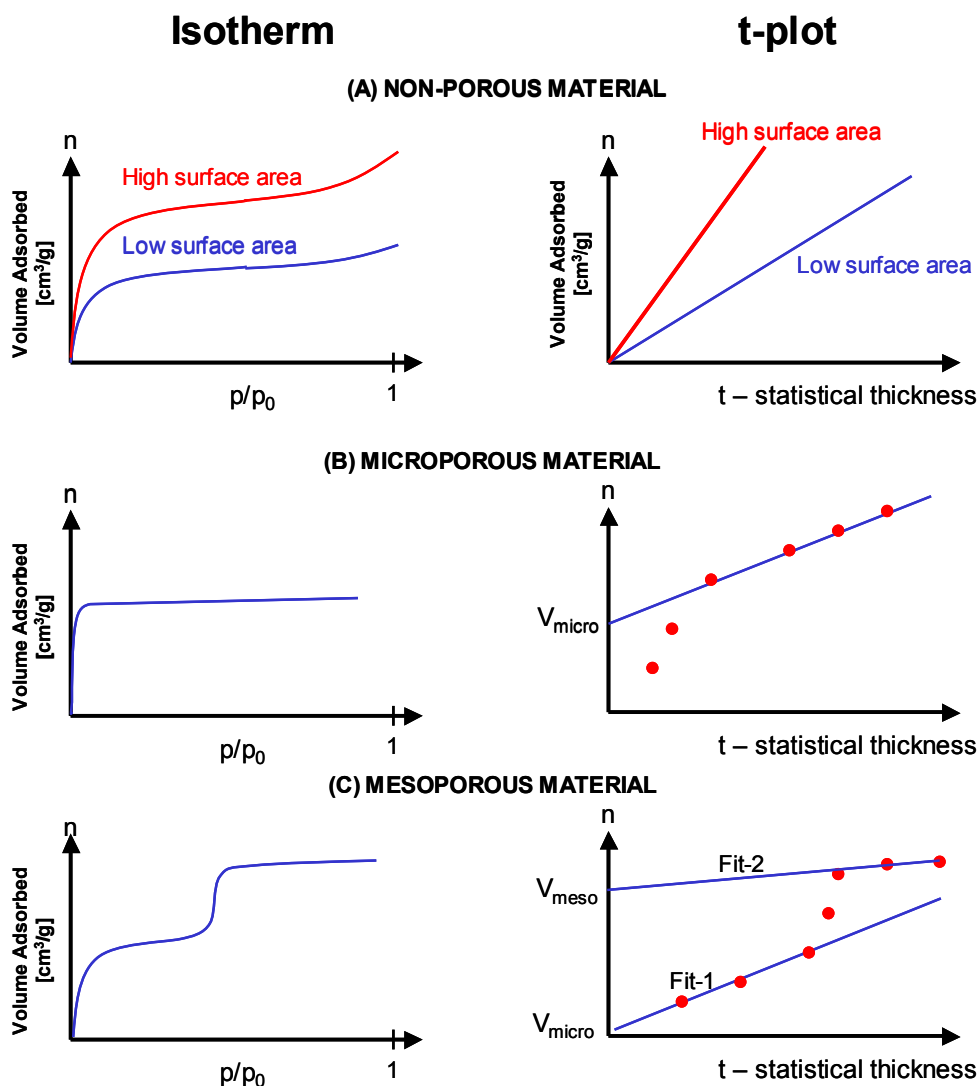
Figure 26. t-plot and isotherms for estimation of the surface area and porosity. (a) non porous materials with different surface areas. (b) microporous material and (c) mesoporous material

In the case of such micro- and mesoporous hybrid materials one cannot use directly the point at $p/p_o = 0.2$ for the estimation of micropore volume. It is due to the fact that already at this pressure multilayer formation of the adsorbate takes place in the mesopores and the calculated value leads to overestimation of the micropore volume.

3.2.   **Low and High Angle X-ray Diffraction**

Low angle X-ray diffraction of ordered mesoporous materials

The low angle X-ray measurements (from 0.5 to 6 2θ) were used to characterize the symmetry of the pore structure ordering in the mesoporous materials. In contrast to the wide angle X-ray diffraction, not only ordering of single atoms is observed, but also periodicity of electron density due to the existence of an ordered pore structure (if the walls of such material are crystalline, also reflections in high angle are observed). Since the distances between pores are much larger than the distances in single atoms in crystalline materials, the reflections are observed at low angles (as can be expected from Bragg equation).
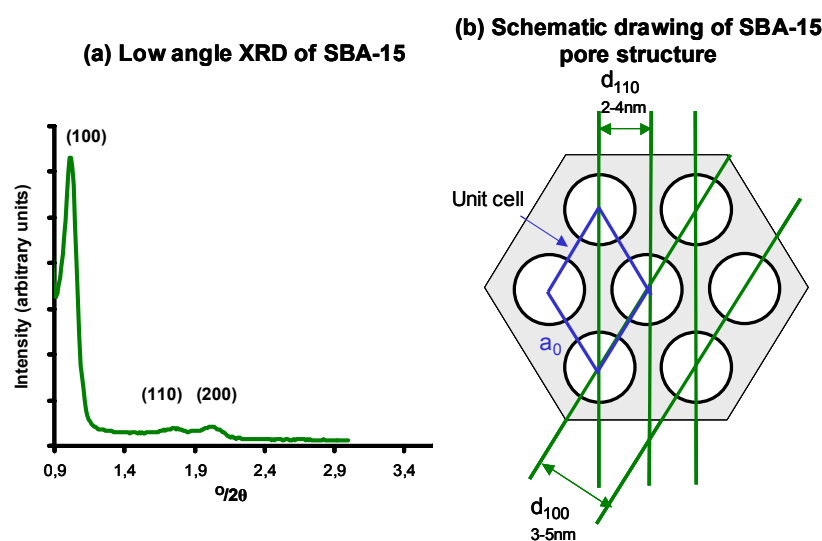
Figure 27. (a)Low angle diffraction of SBA-15 ordered mesoporous material (b) lattice plane assignment in the structure of SBA-15. Due to two- dimensional periodic structure of SBA-15 pores (the c-axis could be assumed as infinite) description with only a and b axes was also used (eg. instead of (100) plane index, (10) could be used).

Although for ordered mesoporous materials the pore structure can be identified from low angle diffractograms [Figure 27a], the exact peak position changes with different preparation procedures, pore size and pore wall thickness (unlike in crystalline microporous materials: zeolites or MOFs). Since the distance between the pores is easily calculated from geometric considerations [Figure 27b], also the wall thickness can be estimated if nitrogen physisorption data are available for pore diameter calculation.

Peak broadening : particle size estimation via Scherrer equation

In the case of well crystalline materials, narrow peaks should be observed on the diffractograms. However, if crystallites become imperfect or small, the peaks become broader.

This is also typical for nanocrystalline materials (where a smaller amount of lattice planes in single crystal contributes to one reflection).
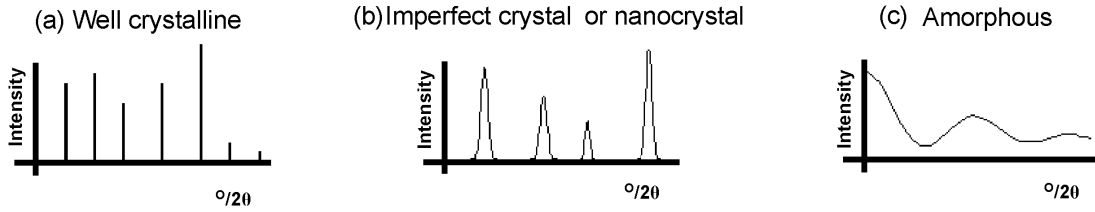
Figure 28 Powder X-ray diffractograms of (a) well crystalline material, (b) imperfect crystals or nanomaterials

The relation between particle size and peak broadening was first expressed as an empirical equation by Scherrer:

$$d_{crystallite} = K\frac{\lambda}{B_{cryst}\cos\theta} \tag{9}$$

The average crystallite size ($d_{crystallite}$) is calculated for a given reflection (at given θ angle), by measuring its integral half-width (B_{cryst} (radians)) for a given X-ray wavelength λ. The K shape factor is in the range between 0.87 and 1.39 (for spherical particles K = 0.9). However, it was found that not only particle size could cause peak broadening, but also the existence of stress/strain in the crystallite:

$$B_{strain} = 2\varepsilon\tan\theta \tag{10}$$

Where B_{strain} is the peak broadening caused by the strain in the crystallite; ε = strain in the crystallite; θ = peak position for which calculation was made.

Both effects can be distinguished by analysis of how the peak width changes with the θ angle. In the case of crystallite size broadening, the peak width changes as a function of cos θ (eq. 9), while for strain dependent broadening, as a function of tan θ (eq. 10). Both effects add up and are given in the form of linear function (when (B_{cryst}+B_{strain}) cos θ is plotted against sin θ) known as Williamson-Hall plot. Both stress and strain can be calculated from the plot:

$$(B_{cryst} + B_{strain})\cos\theta = K\frac{\lambda}{d_{crystallite}} + 2\varepsilon\sin\theta \tag{11}$$

However, the observed peak broadening (B_{obs}) typically measured directly from the diffractogram, depends also on the instrumental resolution and changes after each time when slit/collimator configuration is modified. Therefore, before each particle size estimation a standard (LaB_6) composed of large crystals is measured in the same configuration in order to extract peak width caused by the equipment (B_{instr}).

3.3 Synthesis Procedures and Experimental Setups

Chemicals used the in syntheses

Chemical	Formula	Purity	Supplier
Tetraethoxysilicate	$(C_2H_5O)_4Si$	98%	Acros Organics
Potassium hydroxide	KOH	85%	Reninghaus Chemie
Ammonia	NH_4OH	24%	BASF
Hexadecyl-trimethylammonium Bromide (CTABr)	$C_{16}H_{33}N(CH_3)_3Br$	ca.100%	Acros Organics
Dodecyl-trimethylammonium Bromide	$C_{12}H_{25}N(CH_3)_3Br$	ca.100%	Acros Organics
Pluronic 123	$EO_{20}PO_{70}EO_{20}$	ca.100%	BASF
Hydrochloric acid	HCl	37%	BASF
Dimethyldichlorosilane	$Si(CH_3)_2Cl_2$	98%	Fluka
Platinum acetylacetonate	$Pt(acac)_2$	99%	ABCR
Vanadium acetylacetonate	$V(acac)_3$	99%	Aldrich
Vanadium pentoxide	V_2O_5	99.6%	Acros
Molybdenum oxide	MoO_3	99.6%	Acros
Ammonium heptamolybdate Tetrahydrate	$(NH_4)_6Mo_7 \cdot 4H_2O$	99%	Acros
Palladium acetylacetonate	$Pd(acac)_2$	99%	Aldrich
Polycarbosilane (M_w=800)	$-[SiHCH_3-CH_2]-_n$	99%	Aldrich
Polycarbosilane SMPT-10	not specified	-	Starfire
Hydrofluoric acid	aqueous HF	40%	VWR
Toluene	C_7H_8	99%	VWR
Hexadecylamine	$C_{16}H_{33}NH_2$	90%	Aldrich
Palladium supported on carbon (Escat 103) C-1	Pd / C	5 wt.% Pd	Aldrich

3.3.1   Synthesis of Ordered Mesoporous Silica Materials

MCM-41

2.4 g of CTABr was dissolved in 120 ml of deionised H_2O (200 ml beaker). Then 9.5 g of 25% ammonia was added and stirred for 15 minutes. 10 g of TEOS was added and the solution was stirred for 1 hour. The mixture was filtered and washed with 100 ml of water. The solid product was dried overnight at 90 ^{o}C and heated to 550 ^{o}C for 5 hours, with a heating rate of 1 K/min (the silica yield was 98-100%). In order to control the pore diameter, instead of CTABr, surfactants with different hydrocarbon chain lengths could be used in the same mass amount as the CTABr (for example 2.4g of dodecyltrimethylammoniumbromide or 2.4 g of decyltrimethylammoniumbromide). Alternatively, pore size control could also be achieved via addition of a swelling agent (toluene or trimethylbenzene) to the surfactant/water solution before TEOS addition.

MCM-48

In a 200 ml glass beaker containing 22.32 g of distilled water 0.56 g KOH was dissolved. After 10 minutes, 4.74 g of surfactant was added (CTABr). This mixture was stirred for at least 20 minutes, until it became clear (CTABr was completely dissolved). Then 4.17 g of TEOS was added to the solution at once (stirring was continued). After 20 minutes a white, milky liquid product was transferred into a teflon liner and placed into an autoclave for three days at 115 ^{o}C. When the heat treatment was finished, the mixture was filtered and washed with 1.5 liter of water. The filtered product was dried for 1 day at 90 ^{o}C and then heated to 550 ^{o}C for 5 hours, with a heating rate of 1 Kmin^{-1} (the silica yield was 98-100%).

SBA-15[166]

3.46 g of Pluronic P123 was dissolved in 62.8 g of distilled water and 2.0 g conc. HCl (35%) to which 7.44 g of TEOS was added at once at 35 ^{o}C while stirring (SiO_2/P123 = 60). The mixture was then stirred for 24 hours at the same temperature. Afterwards, the temperature was increased to the desired hydrothermal treatment temperature (from 35 to 130 ^{o}C) and left 24 hours under static conditions. After cooling down, the solid was recovered by filtration (without washing with water) and the resulting product was immediatly calcined (without drying) at 550 ^{o}C for 5 hours (heating rate 1Kmin^{-1}) (the silica yield was 98-100%). In this

synthesis approach the wall thickness was easily controlled by controlling the SiO_2/P123 ratio in the range of 45-75 (the concentration of P123 in water remains constant and different ammounts of TEOS was used).

Table 3. Hydrothermal synthesis parameters of SBA-15 materials.

Sample code	Synthesis temperature [^oC]	Chapters
SBA-15	80	3.3.2; 4.1.1 – CVI of SiC
SBA-15	130	3.3.3; 4.1.2 – polymer derived mesoporous SiC

CMK-1 - Carbon inverse replica of MCM-48 silica[11]

1g of MCM-48 was impregnated with a solution of sucrose/H_2SO_4/water (1.25g/0.077ml/4.5g), dried at 343 K for 1h, at 373 K for 6h and at 433 K for 6h. The obtained black solid was ground and impregnated for the second time with sucrose solution (0.8g sucrose/0.049ml H_2SO_4/3g water) and heat treated according to the procedure described above. The pyrolysis was performed at 1173 K for 4h, with a heating ramp of 60 K/h. The silica/carbon nanocomposite obtained was treated with HF two times, filtered, washed with ethanol and dried at 373 K.

3.3.2   Chemical Vapor Deposition of SiC in Ordered Mesoporous Silica

SiC/SBA-15 nanocomposites preparation and mesoporous SiC via dissolution in HF[21]

The deposition of SiC on SBA-15 was carried out at atmospheric pressure in a hot-wall vertical quartz tube reactor which was 500mm in length and 30mm in diameter [Scheme 1]. The mesoporous host was supported on a quartz frit located in the middle of the tube. Dimethyldichlorosilane (DDS) was introduced as the SiC precursor into the reactor from the bottom using a saturator, and hydrogen/argon (4:3) as the gas mixture (V=2 Lh^{-1}, DDS evaporation rate = 1 mlh^{-1}, $T_{reactor}$=1118 K, heating rate = 10 Kh^{-1}). The host was heated in the carrier gas up to 673 K, and then dimethyl dichlorosilane vapor was introduced. After a specified time at reaction temperature, the reactor was cooled down to room temperature with a cooling rate of 5 Kh^{-1}. The prepared composite material was taken out from the reactor and treated with 30% HF solution (200ml) for 2 days, in order to remove the silica. The resulting porous silicon carbide was washed with water several times and dried at 343 K.
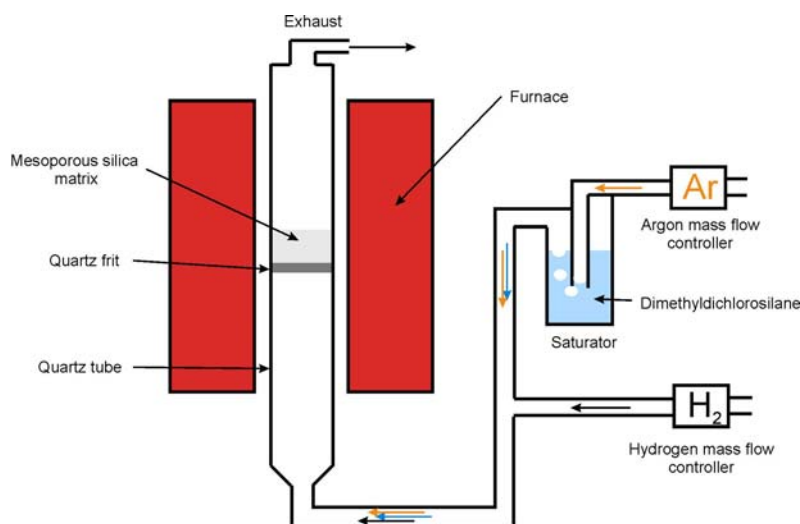
Scheme 1. Chemical vapor deposition reactor for synthesis of SiC/SBA-15 nanocomposites used for preparation of mesoporous SiC

Autogenic pressure synthesis of high surface area SiC via decomposition of TMS in SBA-15

A ½ inch Swagelok union part was filled with SBA-15 and heated to 523 K under argon for 1h in order to evaporate physisorbed water. Subsequently tetramethylsilane (TMS) was added and the vessel was closed (under argon). The closed vessel was placed in a quartz tube and heated to 1273 K in an argon flow with a heating ramp of 120 Kh^{-1} and maintained at this temperature for 6h. Afterwards the oven was cooled for 2 hours to room temperature and the resulting SiC/SBA-15 composite was treated with 10% HF solution in order to obtain high surface area SiC.

3.3.3 SiC Inverse Replica of Ordered Mesoporous Silica by Melt Infiltration

In the typical synthesis procedure[22] 1 g of SBA-15 was placed in a glass reactor, dehydrated at 150 ^oC in vacuum for 1 h, flushed with argon and cooled down to room temperature. Subsequently, 1.25 g of polycarbosilane (PCS - Aldrich or SMPT-10 - Starfire) was added and heated rapidly to 320 ^oC in an inert atmosphere. The sample was stirred several times and left at the same temperature for 12h. The infiltrated sample was cooled down, transferred to a high temperature oven, and heated in argon to 1300 ^oC with a heating ramp of 50 $^oCh^{-1}$ for 2 hours. Afterwards the obtained SiC/SBA-15 nanocomposite was treated with 125 mL of EtOH/H_2O/40% HF solution (volume ratio 1/1/1) and with water several times.

3.3.4 Incorporation of Metals and Metal Oxides into Ordered Mesoporous Silica

Pt,Pd,V_2O_5/MCM-41 in-situ synthesis procedure by delivery with swelling agent[27] (samples M-1, M-2, M-3, M-4, V-1- Chapter 4.2.1; IVN-1, IVN-2 – Chapter 4.3.1)

A somewhat modified synthesis of Grün et al.[167, 168] was employed. 1.2 g CTABr was dissolved in 60 ml H_2O and 4.75 g of conc. NH_3 (25 %) and heated to 50 ^{o}C. The solution was kept in a closed glass bottle during the synthesis. To this mixture an appropriate amount of Pt(acac)$_2$ (or V(acac)$_3$) dissolved in toluene was added (The Pt(acac)$_2$ solution was ultrasonicated at 80 ^{o}C and added quickly before cooling down). The resulting mixture was stirred rigorously for 20 min at 50 ^{o}C, and 5 g TEOS was added at once. The mixture was subsequently stirred for another 60 min and cooled down to 35 ^{o}C. The solid was filtered out and washed with 100ml of distilled water. The solid product was dried at 100 ^{o}C overnight and calcined in air according to the following heating program: heating to 180 °C with 1 °Cmin^{-1}, plateau for 180 min at 180 ^{o}C, heating to 450 ^{o}C with 1 °Cmin^{-1} followed by a plateau at 450 °C for 5 h. For the synthesis of Pd/MCM-41 and V_2O_5/MCM-41 instead of Pt(acac)$_2$, Pd(acac)$_2$ in toluene was used as a metal precursor for palladium containing MCM-41 materials, and V(acac)$_3$ in toluene for vanadium integration in MCM-41.

Pt/SBA-15 in-situ synthesis procedure by delivery with swelling agent[27] (samples S-1, S-2 - Chapter 4.2.2)

For metal-containing SBA-15 the synthesis method of Zhao et al.[7, 8] was modified. 2.41 g of Pluronic 123 (BASF) was dissolved in 63.4 g of distilled water (overnight) and 12.05 ml HCl (37%). Subsequently, an appropriate amount of the Pt(acac)$_2$/toluene solution was added (at 40 ^{o}C) and stirred for 20 minutes. In the next step, 5 g of TEOS was added within 30 minutes (while stirring) and stirred for 4 hours at the same temperature. An additional heat treatment at 80 ^{o}C in a polypropylene bottle was performed without stirring for 24 h. The solution was cooled down, filtrated, washed with 100 ml of water, dried at 100 ^{o}C and calcined using the same temperature program as indicated for the Pt/MCM-41 synthesis.

V_2O_5/MCM-41 in-situ synthesis procedure by direct solubilization in surfactant/water solution[27] (sample V-2 – Chapter 4.2.2; IVN-2, IVN-4 – Chapter 4.3.1)

2.4 g of CTABr was dissolved in 120 ml of deionised H_2O (200 ml beaker). Then 9.5 g of 25% Ammonia was added and stirred for 15 minutes. Afterwards an appropriate ammount of V(acac)$_3$ was dissolved in the solution overnight. In the next step, 10 g of TEOS was added

and stirred for 1 hour. The mixture was filtered and washed with 100 ml of water. The solid product was dried overnight at 90 ^{o}C and calcined as for the procedure above.

Ex-situ synthesis of supported vanadium oxide

Vanadium oxide was supported on various ordered mesoporous silica supports (SBA-15, MCM-41) and on microporous activated carbon NORIT-A. The ex-situ infiltration was performed via multiple incipient wetness infiltrations of porous supports with V(acac)$_3$ solution in toluene, each time followed by oxidation at 400°C [Table 4].

Table 4. Ex-situ synthesis of supported vanadium oxide

Sample code	Support (weight)	Infiltration cycles (ml of solution for each cycle)	Solution used
EM-VN-1	MCM-41 1g	5, 4, 3.5	3.5g V(acac)$_3$ in 50ml Toluene
EM-VN-2	MCM-41 1g	6.5, 5.5, 3.5, 3.5	3.5g V(acac)$_3$ in 50ml Toluene
EM-VN-3	MCM-41 1g	2	0.5g NH$_4$VO$_3$ in 2ml H$_2$O$_2$
ES-VN-1 and ES-VC-1	SBA-15 1g	3, 3, 1	7g V(acac)$_3$ in 50ml Toluene
EC-VN-1 and EC-VC-1	NORIT-A 1g	5, 4.5	3.5g V(acac)$_3$ in 50ml Toluene

3.3.5 Nitridation and carbonization of supported vanadium oxides for preparation of supported nitride and carbide catalysts

Nitridation of supported vanadium oxide

The as prepared supported oxides (0.8g) were nirtided in ammonia flow (160 mlmin^{-1}) at 800 ^{o}C for 1 h in a plug flow reactor with a heating rate of 120 ^{o}Ch^{-1}. After cooling down to room temperature, the samples were passivated in an O$_2$/N$_2$ gas mixture (1 vol.% O$_2$) for 4 h.

Carbonization of supported vanadium oxide

Supported oxides were carbonized in CH$_4$/H$_2$ (25% CH$_4$) gas flow at 1000°C for 1 h (heating ramp 120 ^{o}Ch^{-1}) in a plug flow reactor. After cooling down to room temperature the samples were passivated in an O$_2$/N$_2$ gas mixture (1 vol.-% O$_2$) for 4 h.

3.3.6 High Surface Area Nitrides by Foam Procedure[25]

5 g of V$_2$O$_5$ (or ternary precursors) was mixed with 10 g of hexadecylamine and 15 ml of acetone. The slurry was stirred until a pasty material formed (5−10 min) and, subsequently, 250 mL of 30 wt.-% H$_2$O$_2$ solution were added. The foaming process started after a few

minutes and the product was spread onto a clean glass surface for overnight drying. The as-prepared foam was placed in a vertical quartz tube reactor (diameter of 3 cm with a quartz frit in the middle) and heated in an ammonia flow (from bottom to top) at a heating rate of 120 °C h^{-1} to 800 °C. This temperature was maintained for 2 hours. After cooling the reactor down to room temperature, the solid product was passivated in the same tube in an O_2/N_2 gas mixture (1 vol.-% O_2) for 4 hours. The ammonia flow during the synthesis was maintained at the same level (170 cm^3min^{-1}) for all foam-derived samples. The loadings of the foam in the reactor were as follows: 1.5 g (VN-1), 2.5 g (VN-2), and 7.5 g (VN-3) of foam. In the case of vanadium nitride prepared by the standard procedure, the ammonia flow from top to bottom was used (1047 $cm^3\ min^{-1}$) and the reactor was loaded with 6 g of sample.

3.3.7 Catalytic Tests

Cinnamic acid hydrogenation

0.4 g of cinnamic acid (99 %; Adlrich) were dissolved in 16 g of ethanol (99 %). To the substrate 0.24 g of the solid catalyst were added. The mixture was stirred at room temperature (25 ^{o}C) and dynamic hydrogen was used for the reduction (1 bar, 50 $mLmin^{-1}$) directly without any pretreatment of the catalyst. Periodically taken samples were analyzed with a GC/MS. For comparison, the reaction was also carried out using a commercially available Pd/carbon catalyst with the same substrate/catalyst ratio (5 wt% Pd, Escat 103; Aldrich), which is later referred to as C-1.

Propane dehydrogenation

Propane dehydrogenation tests were conducted by Patrizia Laura De Cola in Prof. Weitkamp group at the Institute of Chemical Technology in Stuttgart . The catalytic experiments were carried out at ambient pressure, a constant reaction temperature of T = 525°C and at a weight hourly space velocity of WHSV = $2h^{-1}$ in a flow-type apparatus with a fixed-bed reactor made from quartz glass. Prior to the experiments, the catalyst powders ($m_{cat.}$ = 300mg) were loaded into the reactor between two quartz wool plugs and treated with hydrogen (100$cm^3\ min^{-1}$, 525°C, 1h) to remove the oxide passivation layer. Pure propane (99.95vol.-%, Westfalen) was used as the feed. Samples were periodically taken from the gaseous reactor effluent and analyzed by capillary gas chromatography. Conversions and

selectivities for propene were reproducible within a relative deviation of ±2% and ±1% respectively.

3.3.8 Instruments and Settings

Nitrogen physisorption

Nitrogen physisorption was measured at 77K on a Quantachrome Autosorb 1C or Micromeritics ASAP 2010 aparatus. Prior to the measurement, the samples were evacuated at 150-250 ^{o}C for minimum 5 h. The BET specific surface area was typically calculated in the pressure range of 0.05-0.2 P/Po.

Hydrogen chemisorption

Hydrogen chemisorption was measured at 77K on Quantachrome Autosorb 1C. Prior to the measurement, samples were evacuated at 150-250 ^{o}C for minimum 5 h. Standard measurement procedure was employed (heating in hydrogen to 400°C, cooling down under vacuum and dosing of the hydrogen at 35°C. The physisorption effect was excluded via the secondary adsorption measurements directly after evacuating of the already measured sample.

X-ray diffraction

X-ray powder diffraction patterns were recorded in transmission geometry using a Stoe Stadi-P diffractometer and Cu Kα_1 radiation (λ = 0.15405 nm), with a position sensitive detector (PSD).

Transmisssion Electron Microscopy (TEM)

Transmission electron micrographs were obtained on a Hitachi HF 2000 and Cs-corrected 200kV-TEM FEI Tecnai F20 TEM using a copper grid type sample holder.

X-ray Photoelectron Spectroscopy (XPS)

XPS measurements were carried out with a Kratos HSi instrument using a monochromated Al Kα (1486.5 eV) X-ray source operating at 300 W. A large sample area of 700x300 μm was probed. The pass energy for narrow scans was set to 40 eV. The spectrometer was calibrated using Cu $2p_{3/2}$ and Au $4f_{7/2}$ peaks. The base pressure in the UHV chamber was <10^{-9} Torr. The spectra were charge referenced to the oxygen component set at a binding

energy of 533 eV for O 1s. For the curve fitting, a nonlinear least squares curve fitting algorithm was used.

Coupled Gas Chromatography and Mass Spectroscopy (GC/MS)

Samples taken periodically from the reactor were diluted further with Ethanol (1:1) and injected into the GC/MS (Shimadzu GCMS-QP5000). Prior to measurements, known standard mixtures of educt/product in ethanol were used for calibration. Helium was used as a Carrier gas and capillary column was heated to 350 ^{o}C with a heating ramp of 5 ^{o}Cmin^{-1}.

Elemental analysis

The high temperature combustion method was used to analyze carbon content (LECO C200). For analyses of N,H,O, the hot gas extraction method was used (LECO TCH 600). The chemical analyses of the content of platinum, palladium and vanadium, respectively, were carried out with the ICP-OES (Inductively Coupled Plasma-Optical Emission Spectrometer) Vista (Varian). The samples (amount of about 10 mg) were digested in a mixture of 1.5 ml HCl (37 %), 0.5 ml HNO$_3$ (65 %) and 1 ml HF (40 %) by heating. Generally, the solutions were diluted to a volume of 50 mL using a volumetric flask.

Solid state NMR measurements

Solid-state NMR spectra were measured on a Bruker Avance 500WB spectrometer using a 6-mm MAS (magic angle spinning) probe at a spinning rate of 10 kHz. As reference Tetramethylsilane was used.

Coupled Thermogravimetry and Mass Spectroscopy (TG/MS)

The TG/MS measurements were carried out using a Netzsch STA 409PC thermobalance coupled with a Netzsch QMS 403C mass spectrometer via a capillary heated to 300 ^{o}C. Samples were heated in air up to 700 ^{o}C with a heating rate of 2 ^{o}Cmin^{-1}.

FT-IR-measurements

Samples were measured on the Nicolet MAGMA-IR 550 spectrometer. Prior to the measurement samples were mixed with KBr and pressed in form of pellets.

4. Results and Discussion

4.1 Nanocasting of SBA-15 for the preparation of Mesoporous Silicon Carbide

One of the main aims of this PhD work was to find new synthesis methods of the mesoporous high surface area silicon carbide. Such materials could be interesting high temperature supports for catalysts due to their specific thermal, mechanical and chemical properties (Chapter 2.4). For the first time it was shown here how to synthesize a high surface area mesoporous silicon carbide using ordered mesoporous material as hard inert template. Three different syntheses approaches were used to infilitrate ordered mesoporous silica (SBA-15) with silicon carbide [Scheme 2]. Chemical vapor inlitration (CVI) from simple silanes (dimethyldichlorosilane) in hydrogen (Chapter 0), reaction under autogenic pressures (Chapter 0), and liquid infiltration of preceramic polycarbosilane precursor and its subsequent conversion to SiC (Chapter 4.1.2). All these preparation methods differed significantly and showed their own advantages and disadvantages. For example, in the case of CVI, good control over the chemical composition of SiC was obtained (Si/C ratio), while for the polymer derived materials such control was not possible. On the other hand, polymer derived materials had highly ordered pore structure and a narrow pore size distribution. In the following two chapters all three methods and their influence on the properties of mesoporous SiC are presented and discussed.
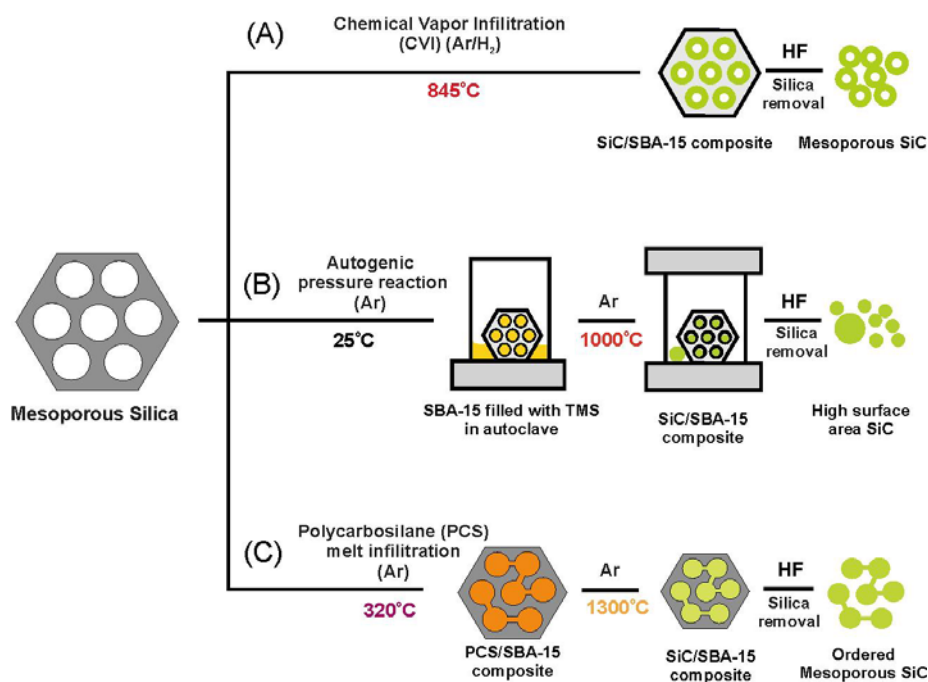
Scheme 2. Synthetic methods for the preparation of mesoporous high surface area silicon carbide via templating of SBA-15. A - chemical vapor infiltration; B – reaction under autogenic pressure of tetramethyl silane (TMS); C – infiltration with preceramic polycarbosilane precursor

4.1.1   High Surface Area Mesoporous SiC via Chemical Vapor Infiltration (CVI)

In the following paragraphs, methods for preparation of silicon carbide via the deposition from volatile simple silanes in mesoporous silica are presented. First, the preparation of the SiC/SBA-15 composites in atmospheric pressure from the dichlorosilane (DDS) in the plug flow reactor (Chapter 3.3.2) is described and then the influence of the composite properties on the properties of the final mesoporous SiC product is discussed. The next part part deals with preparation of SiC/SBA-15 composites in a closed reactor under high autogenic pressures (using tetramethylsilane as SiC precursor). Finally, high temperature structural stability of different SiC materials is compared to ordered mesoporous silica template and ordered mesoporous carbon.

Atmospheric Pressure CVI of Dimethyldichlorosilane (DDS) into SBA-15 and Resulting Mesoporous SiC Materials

The CVI of ordered mesoporous silica with silicon carbide was already investigated in the previous work.[169] MCM-48 and SBA-15 were compared and optimal deposition conditions were estimated. SBA-15 was concluded to be a more suitable material for infiltration, due to the higher thermal stability and larger pores. The deposited SiC was also found to enhance thermal stability of the ordered mesoporous silica host. In the early stage of the deposition process, micropores present in the SBA-15 mesopore walls (Chapter 2.1) were filled. Subsequently a layer of SiC was deposited inside the mesopores until the pore diameter was reduced to around 3 nm [Scheme 3 − 1h40min]. From this point further deposition inside the pores was hindered (limited diffusion of SiC precursor due to small pore diameter) and deposition outside the pores was observed as a dominant process [Scheme 3 − 2h:40].[20, 169] The XPS measurement showed that at the beginning of the deposition silicon oxycarbide species mostly were formed as a coating of silica walls, and on top of it silicon carbide was deposited.[20]

Here, three composite samples with different SiC loadings were prepared using different quantities of SBA-15 (prepared via hydrothermal treatment at 80 $^{\circ}$C) in a reactor [Chapter 3.3.2] and various durations of infiltration [Table 4 − SC-1,2,3]. An additional carbon-rich sample was prepared in argon flow (without hydrogen) [Table 5 − SC-C] in order to investigate the influence of carbon impurities on the properties of mesoporous SiC. At 1118 K, DDS decomposes inside the pores of SBA-15 to form SiC (12) (Scheme 3), but when the

pore diameter is decreased substantially, also deposition of SiC outside the pore system takes place due to limited diffusion of precursor molecules into the pore system.

$$(CH_3)_2SiCl_2 \rightarrow SiC + 2HCl + CH_4 \qquad (12)$$
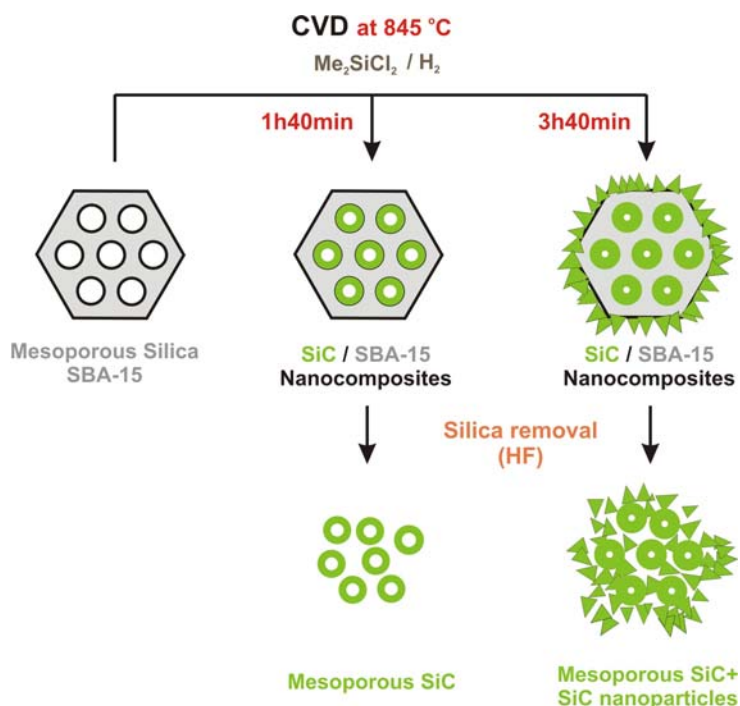
Scheme 3. Chemical vapor infiltration approach to the synthesis of high surface area SiC

The pore diameter of SBA-15 decreased dramatically from 5.5 nm to 3.5 nm already for 1h:40min of deposition time and 30 % of weight gain [Table 4 – SC-3]. Longer deposition times and higher weight gains caused severe reduction of mesopore volume, but the pore diameter did not change further (from 3.5 to around 2.9 and 3.0 nm for 60 and 95 % weight gain) [Table 4 – SC-2, SC-1; Figure 29A]. This result confirmed that too long infiltration times and too high weight gains caused deposition outside the mesopores.

Table 5. SiC/SBA-15 composites: preparation parameters and characterization.

Sample	Infiltration time [h:min]	SBA-15 weight [g]	Weight gain [wt%]	Surface area $[m^2g^{-1}]$	Average pore diameter[b) [nm]	Mesopore volume[c) $[cm^3g^{-1}]$
SC-1	3:40	0.6	95%	130	3.0	0.06
SC-2	3:40	2	60%	213	2.9	0.12
SC-3	1:40	2	30%	294	3.5	0.23
SC-C[a)	3:40	0.6	75%	140	3.4	0.12

a) Sample prepared in Ar/DDS flow – without H_2, b) Average pore diameter (d_p) calculated using total pore volume at 0.95 P/Po (V_p) and measured specific surface area (S_g) according to equation $d_p = 4V_p/S_g$ c) Mesopore volume calculated using the BJH theory for pore size between 2 and 50 nm

After removal of silica from the composite material [Scheme 3], the resulting mesoporous silicon carbide samples had a high specific surface area (higher than that of the SiC/SBA-15 composite material) [Table 5] and showed Type IV nitrogen physisorption isotherms, with a broad adsorption step, suggesting a broad pore size distribution [Figure 29B].

Table 6. Mesoporous SiC prepared by HF treatment of SiC/SBA-15 composites.

Sample	Composite used	Surface area $[m^2g^{-1}]$	Average pore diameter[a)] [nm]	Mesopore volume[b)] $[cm^3g^{-1}]$	Carbon content [wt. %]
SiC-1	SC-1	410	3.1	0.31	25.9
SiC-2	SC-2	578	4.6	0.71	25.2
SiC-3	SC-3	509	7.4	0.96	26.5
SiC-C	SC-C	830	3.1	0.52	36.3

a) Average pore diameter (d_p)calculated using total pore volume at 0.95 P/Po (V_p) and measured specific surface area (S_g) according to equation $d_p=4V_p/S_g$, b) Mesopore volume calculated using the BJH theory for pore size between 2 and 50 nm

The overall nitrogen adsorption capacities were increased, as compared to the composite samples and the highest mesopore volume was measured for SiC-3 with V_p = 0.96 cm^3g^{-1} and a surface area of 509 m^2g^{-1}. A sample prepared with longer infiltration duration (SiC-2) showed a significantly lower mesopore volume (0.71 cm^3g^{-1}), and slightly higher surface area (578 m^2g^{-1}). SiC-1 prepared from the nanocomposite with the highest SiC loading has the lowest surface area and lowest mesopore volume (410 m^2g^{-1} and 0.31 cm^3g^{-1}). This clearly indicates, that too long infiltration duration and too high loadings lead to deposition of SiC outside the pore structure, resulting in agglomerated materials with larger particles.
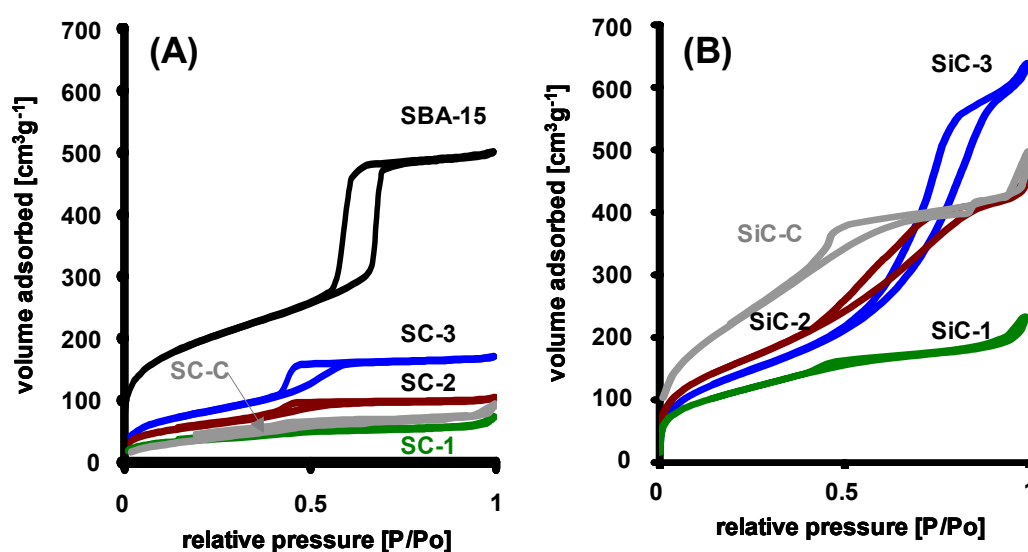

Figure 29. Nitrogen adsorption isotherms (measured at 77K) **(A)** of SiC/SBA-15 materials **(B)** of mesoporous SiC samples derived from SiC-SBA-15 nanocomposites

However, the highest surface area was measured for the carbon-rich sample SiC-C (830 m^2g^{-1}), while the shape of the isotherm was similar to that of SiC-1 (410 m^2g^{-1}). The latter could be due to slightly lower density of carbon materials (1.8-2.2 gcm^{-3}) as compared to the density of silica (2.2-2.6 gcm^{-3}) or silicon carbide (3.2 gcm^{-3}) as well as to the presence of microporosity in deposited carbon. Transmission electron micrographs of porous SiC-3 sample [Figure 30C,D] reveal a slightly ordered structure (short range ordering) in form of one-dimensional tubes/rods. In the case of samples prepared with higher matrix loadings (SiC-2 and SiC-1) this rod structure is less visible due to the material deposited outside the pores during the CVI process [Figure 30A, B]. However, the low angle X-ray measurements did not reveal any long range ordering of all mesoporous SiC samples.
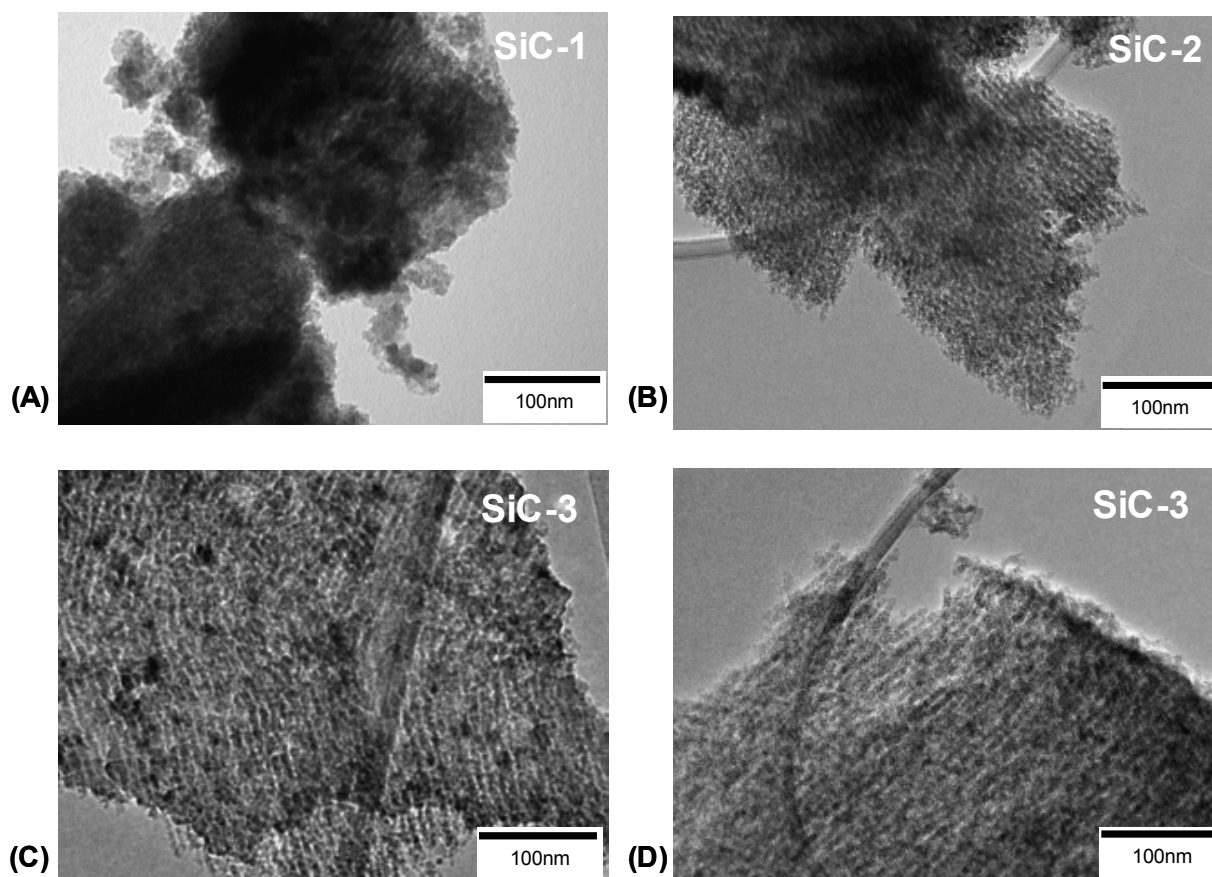
Figure 30. TEM micrographs of mesoporous SiC samples

Wide angle X-ray powder diffraction patterns show that mesoporous silicon carbides prepared with short infiltration duration and low loadings (SiC-2, SiC-3) are X-ray amorphous (as well as SiC-C sample), while the sample with the highest loading (SiC-1) is crystalline and reflections of cubic β-SiC (JCPDS: 73-1665) are detected [Figure 31A]. A small shoulder on the left side of the 111 reflection for SiC-1 sample confirms also the presence of minor

quantities of other SiC polytypes [Figure 31A]. If the amorphous sample (SiC-2) was heated to 1773 K for a short time (1 h), β-SiC reflections were also observed [Figure 31A – SiC-3*].
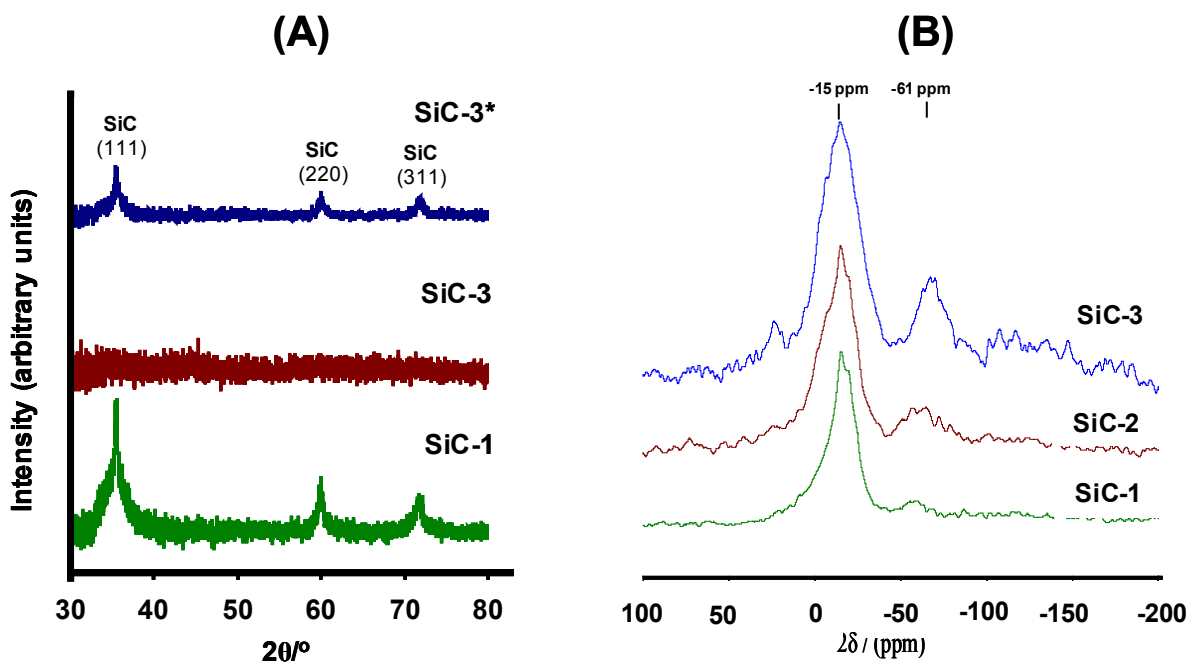
Figure 31. (A) X-ray diffraction patterns of mesoporous SiC samples. SiC-3* is the SiC sample heat treated in argon at 1773 K for SiC crystallization. SiC-2 and SiC-C are X-ray amorphous **(B)** ^{29}Si MAS NMR spectra of mesoporous silicon carbide materials

According to ^{29}Si MAS NMR (Magic Angle Spinning Nuclear Magnetic Resonance) measurements [Figure 31B] the amorphous materials SiC-1 and SiC-2 were found to be composed mainly of SiC (-15 ppm)[170-172] with a small amount of silicon oxycarbide impurities (mainly $SiCO_3$ at –61 ppm, and traces of SiC_2O_2 at –30 ppm and SiC_3O at 15 ppm)[172, 173]. The following chemical shifts were used for the assignment of various SiC_xO_y species: SiC: 0 to –16,[170-172] $SiCO_3$: –60 to –71,[172, 174] SiC_2O_2: –20 to –38,[172, 174] SiC_3O: 5 to 10 ppm.[172, 174] Based on the relative intensities, the lowest amount of oxycarbide species was found for SiC-1 prepared from the composite with the highest weight gain. In SiC-3 the amount of oxycarbides was significantly higher. However, there was no SiO_2 present in any of the measured samples (no peak in the range of –107 to –113 ppm),[174] indicating complete silica removal. This is also confirmed in the FT-IR spectra [Figure 32] with one peak at 819 to 833 cm^{-1} resulting from Si-C bonds vibration for all samples, as well as smaller contribution of Si-O bonds in between 1034 and 1071 cm^{-1}.[175] The relative intensity of the Si-O peak was highest for SiC-3 in agreement with the NMR data. The lowest Si-O peak intensity was observed for the crystalline SiC-1 material.
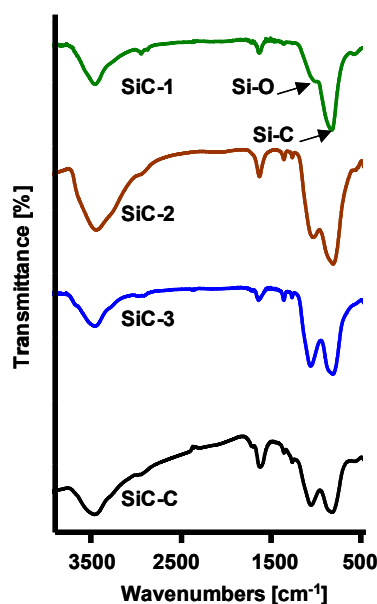
Figure 32. FT-IR spectra of the mesoporous silicon carbide materials

The elemental analysis showed the carbon content in the range of 25-27 wt%, which is slightly lower than the theoretical value of 30 wt% for pure SiC, due to the presence of silicon oxycarbide. However, in the case of SiC-C sample, a higher carbon content (36 wt%) was measured. TG measurements [Figure 33] showed a weight gain of 19 % at 1300 ^{o}C in air (SiC-1) due to the surface oxidation of SiC into SiO_2. Although for complete oxidation 50% weight gain is expected, passivation with silica protects the SiC particles from complete oxidation and process kinetics become significantly slower. In the case of carbon rich SiC-C, a weight loss of 25 wt% was observed due to the burning of the excess free-carbon. According to X-ray diffraction pattern, material resulting from SiC-1 oxidation showed presence of large cristobalite crystallites (JCPDS: 39-1425).
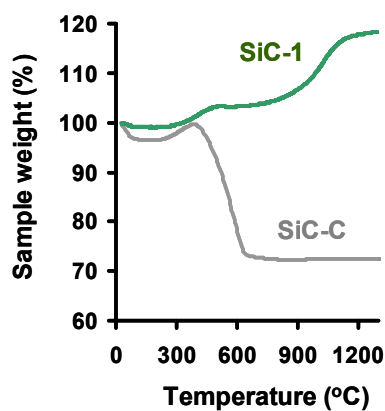
Figure 33. Thermogravimetric measurements of SiC-1 and SiC-C silicon carbide samples in air (heating rate 3 ^{o}Cmin^{-1})

CVI of TMS into SBA-15 under autogenic pressure

In addition to atmospheric pressure deposition of SiC, also formation of SiC under high autogenic pressures in the presence of SBA-15 was studied. The possibility of SiC preparation from simple silanes in an autoclave heated to 1273 K was reported by Pol et al.[138] However, the surface area of such materials did not exceed 150 m^2g^{-1}. Based on the same principle, liquid TMS (tetramethylsilane) was used as a precursor and the decomposition was carried out in a closed Swagelok cell in the presence of SBA-15 [Scheme 4]. TMS has a high vapor pressure and easily condensed inside the pores of the mesoporous silica network. Upon the heat treatment to 1273 K it decomposed to form SiC according to reaction (13):

$$Si(CH_3)_4 \rightarrow SiC + 3CH_4 \tag{13}$$
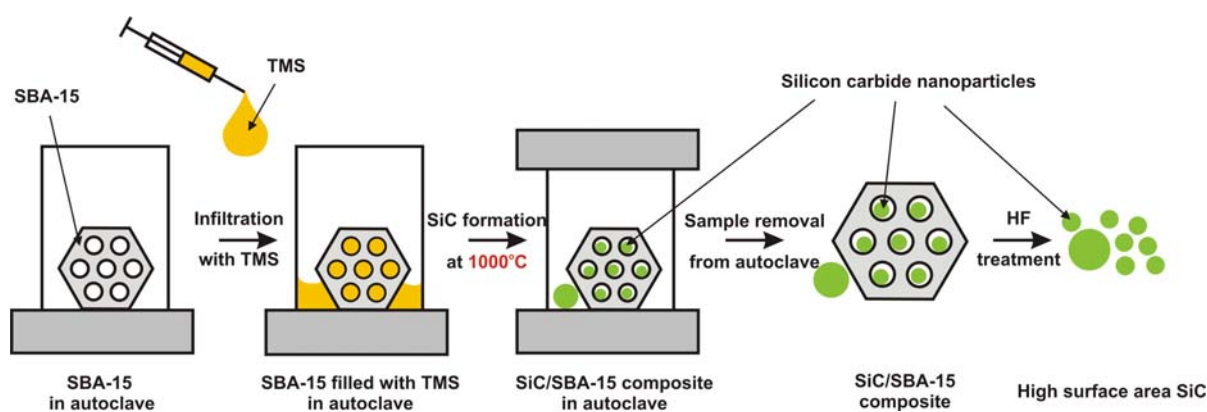
Scheme 4. Preparation of high surface area SiC under autogenic pressure conditions

After synthesis at 1273 K, the autoclave was opened and the resulting product was treated with HF solution in order to dissolve the silica matrix [Scheme 4]. For comparison one sample was prepared without SBA-15 [Table 7 – sample AP-SiC*] (only TMS was present in the autoclave). The X-ray powder patterns showed the presence of cubic β-SiC (JCPDS: 73-1665) [Figure 35] for both samples (AP-SiC: prepared with SBA-15 matrix, and AP-SiC* without SBA-15). In the case of the sample prepared without SBA-15, narrow peaks were observed, indicating the presence of large crystallites. In contrast, the sample prepared in the presence of SBA-15 showed broad peaks, and the crystallite size calculated according to the Scherrer equation was found to be 4 nm. The FT-IR spectra of AP-SiC showed Si-C vibrations at 820 cm^{-1}, and the absence of Si-O bonds [Figure 34].
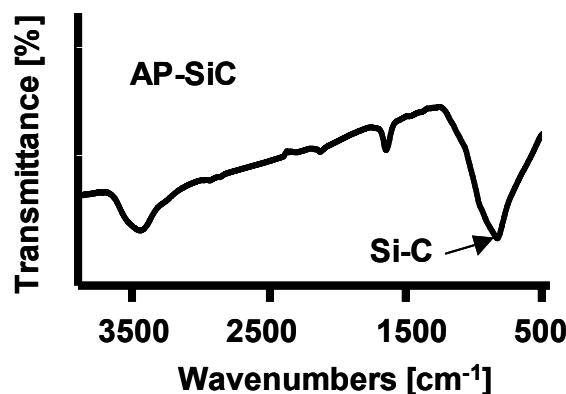
Figure 34. FT-IR spectrum of AP-SiC.

Table 7. High surface area SiC prepared under autogenic pressure conditions – parameters of synthesis and textural characteristics.

Sample	SBA-15 weight [g]	Volume of TMS added [ml]	Surface area $[m^2g^{-1}]$	Average pore diameter [nm]	Mesopore volume[d] $[cm^3g^{-1}]$
[a]AP-SiC*	-	1.50	212	2.3	0.11
[b]AP-SiC-SBA-15	0.225	1.75	387	2.8	0.25
[c]AP-SiC	-	-	636	3.0	0.43

a) SiC prepared in the absence of SBA-15, b) Composite of SiC and SBA-15 before dissolving of the silica matrix, c) SiC prepared by HF treatment of SiC/SBA-15 composite material (AP-SiC-SBA-15), d) Mesopore volume calculated using the BJH theory for pore size between 2 and 50 nm
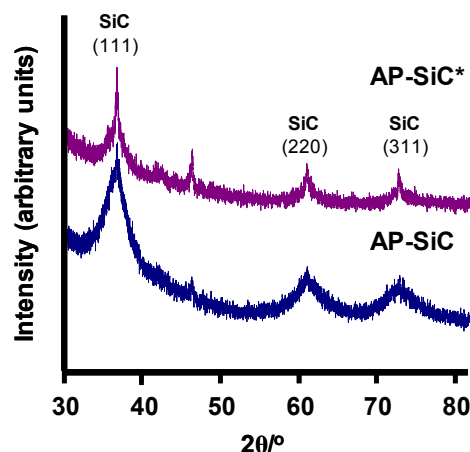
Figure 35. X-ray diffraction patterns of high surface area silicon carbide synthesized under autogenic pressure with (AP-SiC) or without (AP-SiC*) the presence of ordered mesoporous silica SBA-15.

The high specific surface area (636 m^2g^{-1}) confirmed that in the case of AP-SiC, small nanoparticles were synthesized inside the pores of SBA-15. The residual surface area of 387 m^2g^{-1} measured for the composite material AP-SiC-SBA-15, suggested that the pores of SBA-15 were not completely filled [Table 6]. The AP-SiC* material prepared without SBA-15 as a

matrix had significantly lower specific surface area of 212 m^2g^{-1}, which is in good agreement with the X-ray diffractograms showing narrow peaks due to the presence of larger particles. Nitrogen physisorption isotherms [Figure 36] indicated that both the nanocomposite material and the resulting SiC had a broad pore size distribution.
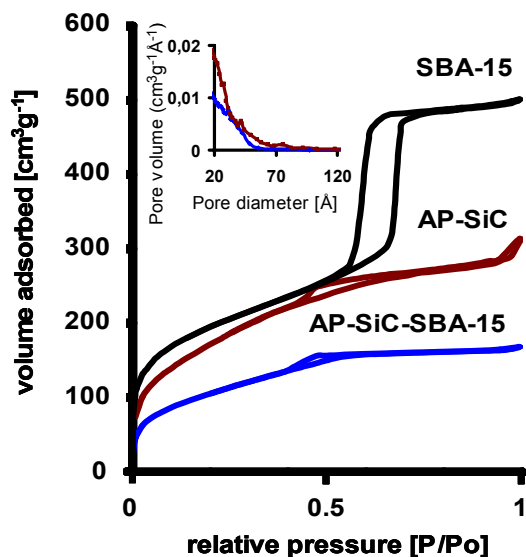
Figure 36. Nitrogen physisorption isotherms (77 K) of materials prepared via TMS infiltration.

The mesopore size distribution was therefore broad (between 2 and 5 nm according to BJH theory) and micropores were present as well. Elemental analysis showed a carbon content of 27 wt%, close to the theoretical value for pure SiC (30 %). This was also in good agreement with TG measurements showing 28 % weight gain due to the oxidation of SiC to SiO_2, the highest value among all samples, confirming that the small particles had only minor impurities of free carbon.

Thermal Stability of SiC, SBA-15 and CMK-1 at 1573 K

For the investigation of the thermal textural stability, silicon carbide samples were compared with the ordered mesoporous carbon CMK-1 and the pure SBA-15 template. The stability of the latter one was already investigated earlier[176], however, for CMK materials only thermogravimetric data were available[177]. All samples were heated to 1573 K in an inert atmosphere (Argon) for a given duration [Table 7]. Mesoporous silicon carbide materials had significantly higher thermal stability in inert conditions [Table 7]. In the first 6 hours of treatment the specific surface area decreased by 23 % for SiC-2 and by 78% for SiC-1, while after 24 hour treatment reduction by 63 % (SiC-3) and 99% (SiC-C) was observed. The latter could be an effect of sintering of nano-sized silicon carbide material, as well as of

decomposition of oxycarbide species into gaseous products (14) or reaction of SiO_2 with SiC and subsequent formation of SiO and CO (15).

$$SiO_xC_y \rightarrow SiO + CO \tag{14}$$

$$SiO_xC_y \rightarrow SiC + SiO_2 \rightarrow SiO + CO \tag{15}$$

Table 8. Specific surface areas of the mesoporous silicon carbide materials, SBA-15 and CMK-1 after heat treatment at 1573 K.

Sample	Original surface area [m^2g^{-1}]	Original mesopore volume[a) [cm^3g^{-1}]	Surface area after 6 h at 1573 K [m^2g^{-1}]	Mesopore volume[a) after 6 h at 1573 K [cm^3g^{-1}]	Surface area after 24 h at 1573 K [m^2g^{-1}]	Mesopore volume[a) after 24 h at 1573 K [cm^3g^{-1}]
SiC-1	410	0.31	92	0.13	8	<0.05
SiC-2	578	0.71	446	0.48	43	<0.05
SiC-3	509	0.96	291	0.51	145	0.29
SiC-C	830	0.52	354	0.22	5	<0.05
AP-SiC	636	0.43	254	0.19	38	<0.05
SBA-15	569	0.75	<1	-	<1	-
CMK-1	1761	1.05	1637	0.82	1528	0.76

a) Mesopore volume calculated using the BJH theory for pore size between 2 and 50 nm

Materials with the lowest amount of silicon oxycarbide (SiC-1, AP-SiC) showed lowest thermal stability and after 6 hours of treatment reduction of the surface area by 78 % (to 92 m^2g^{-1}) and 60 % (to 254 m^2g^{-1}) was observed respectively. On the other hand, these materials have small pore diameters (3.1 and 3.0 nm respectively). The materials with large pores (SiC-3 and SiC-2) showed better thermal stability. For the SiC-2 sample with an average pore diameter of 4.6nm (and medium content of oxycarbide species), after 6 hours treatment, reduction of surface area by 23 % (to 446 m^2g^{-1}) and mesopore volume to 0.48 cm^3g^{-1} was observed [Figure 37]. A longer treatment resulted in a decrease of surface area to 43 m^2g^{-1} (reduction by 92%). SiC-3, with the largest pore diameter (7.4 nm), showed the highest textural thermal stability among all silicon carbide samples, and the remaining surface area of 145 m^2g^{-1} (reduction by 63 %) was measured after 24 hour treatment [Figure 37]. Also a high mesopore volume of 0.29 cm^3g^{-1} was observed after the long treatment. The thermal stability of SiC-2 was also tested in air at 1573 K [Figure 33], but after reaching this temperature the surface area decreased to values lower than 1 m^2g^{-1}. Subsequently, in the X-ray diffractogram narrow reflections of cristobalite were observed (JCPDS: 39-1425) for this sample. This suggests a much lower thermal stability under oxidizing conditions at high temperatures due to the oxidation of SiC to SiO_2. However, such a result was to be expected, since SiC is known to form a silica passivation layer under oxidizing conditions at higher temperatures.[178] In the

case of large micrometer-sized SiC particles such a thin passivation layer protects them from further oxidation, but in the case of nanoparticles, SiC can be completely oxidized.
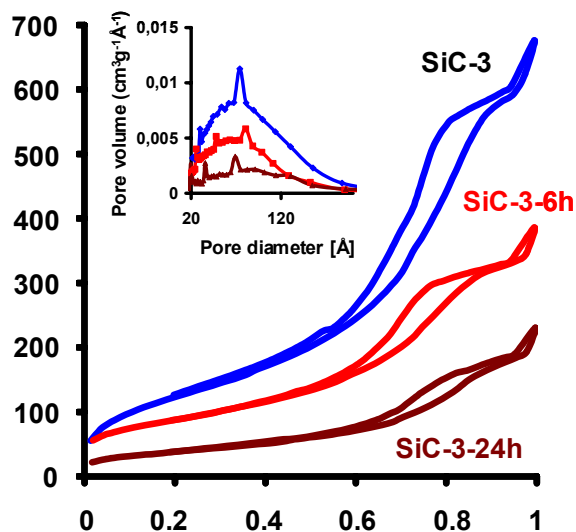
Figure 37. Nitrogen adsorption isotherms (77 K) and pore size distribution of mesoporous SiC-3 sample heat-treated at 1573 K in argon for 6 and 24 h.

The thermal stability of the ordered mesoporous carbon CMK-1 was found to be even higher than that of silicon carbide. The loss of surface area after 6 hours was not significant (from 1761 to 1637 m^2g^{-1}) and the high surface area was observed even after 24 hour treatment (1528 m^2g^{-1}). However, low angle X-ray diffractograms show that already after the short treatment time (6 h), the periodic three dimensional structure of CMK-1 collapsed and no peaks were detected. The high temperature can cause contraction of the mesoporous matrix (significant reduction of mesopore volume without the reduction of overall sorption capacity at 0.95 P/Po).

Conclusions for CVI preparation method

It was shown how different precursors, deposition parameters and loadings of SiC/SBA-15 nanocomposites influence the textural properties of mesoporous silicon carbide prepared from them. High loadings cause deposition outside SBA-15 channels and thus, the obtained SiC material has a low surface area and mesopore volume. Composites with lowest loading produce SiC materials with a high mesopore volume but a broad pore size distribution and high surface area of 510 m^2g^{-1}. As an alternative route to the ambient pressure CVD process also deposition at high autogenic pressures can be employed resulting in materials with even higher surface area (626 m^2g^{-1}). The elemental analysis indicates the formation of silicon oxycarbide on the surface of high surface area SiC. The amount of free carbon deposited was examined using thermogravimetric measurements in air and elemental analysis, and was found to increase the measured specific surface areas if deposited in excess due to lower density of porous carbon materials. High surface area silicon carbide shows a higher thermal stability at 1573 K as compared to pure SBA-15. The thermal stability of ordered mesoporous carbon (CMK-1) is even better than that of porous SiC tested under the same conditions. However, the mesoporous silicon carbide materials prepared via the CVI method did not show any ordering of the pore system in the low angle X-ray diffraction patterns.

4.1.2   Ordered Mesoporous Silicon Carbide (OM-SiC) via Direct Nanocasting of Liquid Polymer Precursors

In the previous chapter, chemical vapor infiltration into SBA-15 was used to prepare mesoporous SiC with surface areas of up to 830 m^2g^{-1} and high temperature stability of up to 1300 °C. However, the as prepared material was poorly ordered on the mesoscopic scale. Here, it is described how a well ordered silicon carbide inverse replica of SBA-15 material is made by infiltration with liquid polymer precursors [Scheme 5 – step 1], subsequent thermal crystallization of SiC [Scheme 5 – step 2] and dissolution of silica [Scheme 5 – step 3].
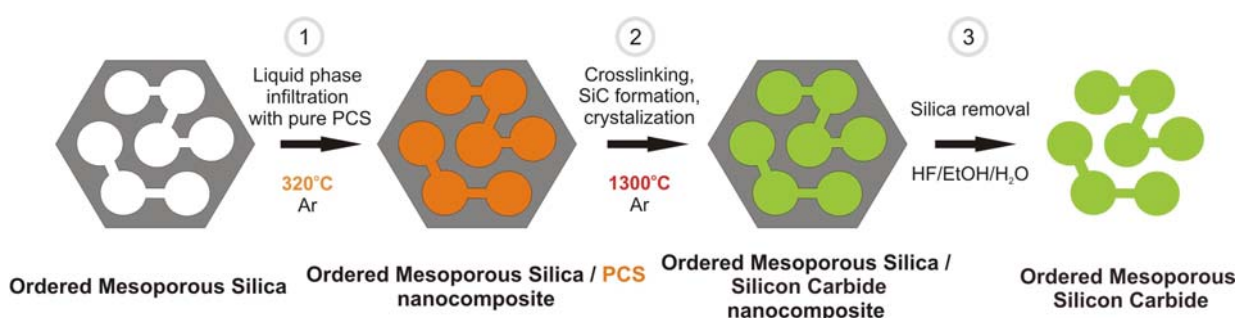
Scheme 5. Preparation of ordered mesoporous SiC via nanocasting

The direct infiltration of liquid low molecular weight precursors into ordered mesoporous silica SBA-15, produces ordered mesoporous SiC with specific surface areas of up to 801 m^2g^{-1}. The possibility of direct melt impregnation was recently discovered as a method for the preparation of ordered mesoporous carbons.[179] In the present investigations, low molecular weight PCS (Polycarbosilane: M_w= 800, m.p. 80 °C) was condensed in the pores of large pore SBA-15 (prepared via hydrothermal treatment at 130 °C). The solvent-free method is essential for a complete infiltration and pore filling, producing highly stable SiC with enhanced surface area. After infiltration, the composite was heated for crosslinking and then transferred to a high temperature furnace and heated in argon to 1300 °C. The composite was washed with HF solution in order to dissolve the mesoporous matrix SiO_2, resulting in highly ordered mesoporous SiC (SiC-800). A second material (SiC-SMPT-10) was obtained using a similar preparation procedure but with a liquid (at room temperature) polycarbosilane precursor (SMPT-10).

In parallel to the work presented here, Shi et al. reported that ordered mesoporous silicon carbide was also prepared via the organic solvent (heptane) assisted nanocasting of SBA-15 and KIT-6 with high molecular weight (M_w= 1500) polycarbosilane.[143]
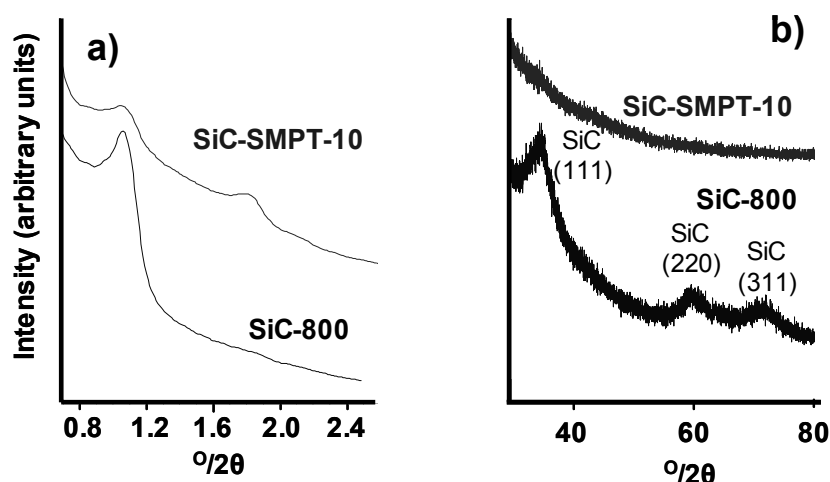
Figure 38. a) Low angle X-ray diffraction patterns of ordered silicon carbide, b) Wide angle X-ray diffraction patterns

According to low angle XRD patterns SiC-800 is ordered on the mesoscopic scale (Figure 38a) and one peak was detected (d = 8.3 nm). However, also nano-crystalline cubic β-SiC was detected in wide angle measurements (Figure 38b). According to nitrogen physisorption measurements (Figure 39a) the material has a high specific surface area of 648 m^2g^{-1} and a narrow pore size distribution with an average pore diameter of 3 nm (Figure 39b).
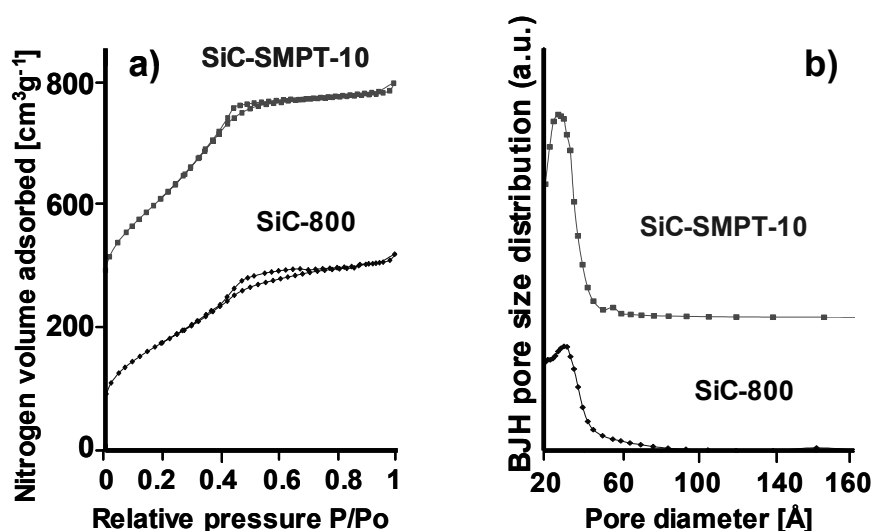
Figure 39. a) Nitrogen physisorption isotherms measured for ordered silicon carbide samples with 200 cm^3g^{-1} offset, b) BJH pore size distribution of silicon carbide samples is calculated from the adsorption branch of the isotherms

An even higher surface area was measured for SiC-SMPT-10 (801 m^2g^{-1}), also with narrow pore size distribution and an average pore diameter of 3nm. In contrast to SiC-800, the

low angle X-ray diffractograms of SiC-SMPT-10 showed two weak peaks at $2\theta = 1.06°$ (d = 8.3 nm, as in the case of SiC-800) and a second one with similar intensity at $2\theta = 1.83°$ (d = 4.8 nm). The presence of the second peak indicated the possibility of tubular structure formation, similar to that reported for CMK-5 (an inverse replica of SBA-15, with hexagonal ordered nanopipes).[77, 180, 181] In the host silica matrix SBA-15, the position of the (100) peak was at 2θ = 0.87 (d = 10.2 nm) which was caused by contraction of the silica host (*by* 18%) due to the high temperature used in the pyrolysis process. The total pore volumes measured (P/Po = 0.95) for both samples were also high: 0.48 cm^3g^{-1} for SiC-800 and 0.58 cm^3g^{-1} for SiC-SMPT-10. Interestingly, the ordered mesoporous SiC-SMPT-10 material was amorphous on atomic scale and wide angle X-ray measurements [Figure 38b] showed no reflections of a crystalline SiC phase.

Significant differences with respect to the precursor used were observed for the SBA-15/SiC composites before HF etching. In the case of SBA-15/SiC-800 composite, the specific surface area was still high (90 $m^2 g^{-1}$), while for the SBA-15/SiC-SMPT-10 composite material, the surface area was extremely low (<10 m^2g^{-1}) and no residual mesoporosity was present demonstrating efficient pore filling. Although the specific surface areas of OM-SiC are higher than for CVD[20]- or autogenic pressure-derived silicon carbides,[21] considerable amounts of free-carbon may be present in polymer-derived SiC increasing the specific surface area due to a lower density of the material. Assuming a density of 3.2 gcm^{-3} for SiC and 2.6 gcm^{-3} for silica, an inverse replica of SBA-15 with a surface area of 610 m^2g^{-1} should yield SiC with a surface area of 496 $m^2 g^{-1}$, which was lower than the observed value.

Thermal gravimetric analysis in air showed that SiC-800 lost 12 wt.% at 600 ^oC due to oxidation of free-carbon. Similarly, oxidation of ordered mesoporous carbons took place at similar temperature.[177] Above this temperature, an additional weight gain of 4 wt% was observed up to 1300 ^oC due to silicon carbide oxidation and silica formation giving a final mass loss of 8 wt.%. Elemental analysis revealed a carbon content of 35 wt.% close to the theoretical value (30 wt.%), but also considerable amounts of oxygen were detected (14 wt.%). The latter was caused by the presence of oxycarbide species on the surface of SiC. The oxycarbide can substantially contribute to the bulk chemical composition in the case of high surface area materials.[175] In IR spectra Si-C bonds are detected in both materials (833 cm^{-1}), and a less intensive peak indicating the presence of Si-O bonds (1046 cm^{-1}) as well (Figure 40). For higher heating rates employed (100 ^oC h^{-1}) the measured amount of carbon was lower (28 wt.%), but

also a lower ceramic yield of 54 % was observed as compared to 77% obtained in the 50 $^{\circ}$C h^{-1} heating ramp.
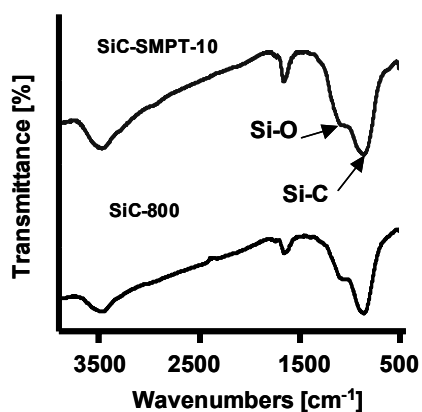
Figure 40. IR spectra of the mesoporous silicon carbide materials
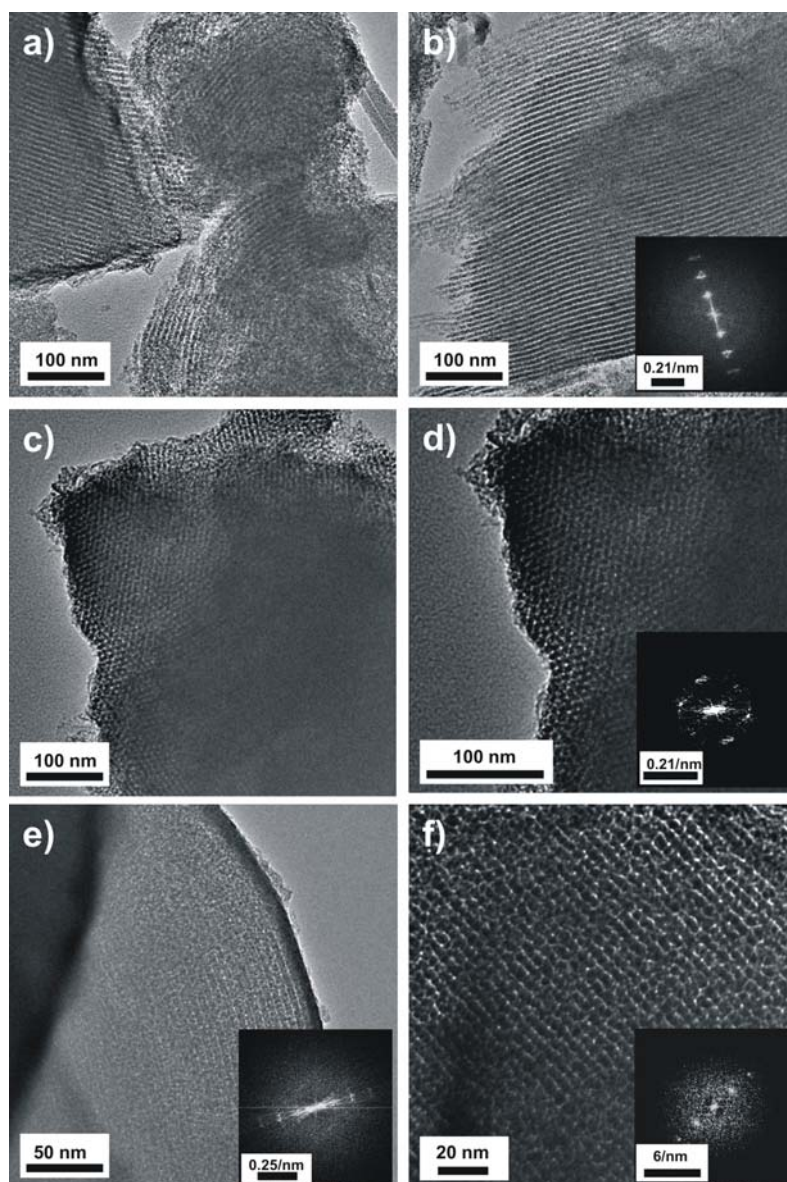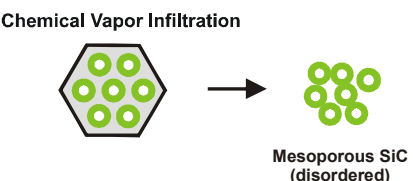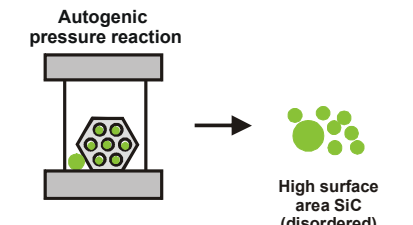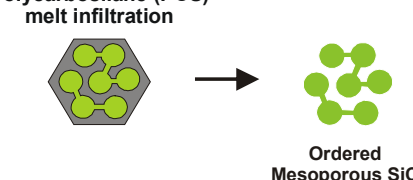
Figure 41. Transmission electron micrographs of the a,b,c,d) SiC-800 sample and e,f) SiC-SMPT-10 sample. Insets show the corresponding Fourier transformations.

Transmission electron micrographs reveal an ordered pore structure of the mesoporous SiC [Figure 41]. Ordering in the SiC-800 sample was detected as being perpendicular [Figure 41a,b,d], and along the pore axis [Figure 41c,d]. The d-spacing was estimated from the Fourier transformed images to be 8.1 nm [Figure 41b]. Figure 41d and the Fourier transformed image confirm the hexagonal pore symmetry. In the case of the SiC-SMPT-10 sample the contrast was low, but in addition to the (100) (Figure 41e) also the (110) d-spacing could be measured (4.6 nm, Figure 41f).

4.1.3 Conclusions

Summarizing, three different methods were developed for the preparation of high surface area mesoporous silicon carbide via nanocasting of the SBA-15 silica [Table 8]. Each of the methods applies different synthesis principles and yields mesoporous silicon carbide materials with different properties and chemical composition.

Table 9. An overview of preparation methods and properties of mesoporous silicon carbide materials via nanocasting of SBA-15 silica.

Preparation method	T [°C]	S_g [m²g⁻¹]	d_m [nm]	C [wt.%]
Chemical Vapor Infiltration Mesoporous SiC (disordered)	850	410-830	2-10	26-35
Autogenic pressure reaction High surface area SiC (disordered)	1000	636	2-4	30
Polycarbosilane (PCS) melt infiltration Ordered Mesoporous SiC	1300	640-800	3	35

T = synthesis temperature; S_g = specific surface area; d_m = mesopore diameter; C = carbon content (30wt% is theoretical value for the stoichiometric SiC)

Chemical vapor infiltration from dimethyldichlorosilane (DMS) resulted in disordered silicon carbide materials with high specific surface area (410-580 m^2g^{-1}), high mesopore volume (up to 0.96 cm^3g^{-1}), but a broad pore size distribution (Chapter 0). Such materials were prepared at relatively low temperature (850 ^oC) from simple silane precursor, with a good control of the chemical composition (C content) by changing the deposition parameters (Ar/H_2 ratio).

Autogenic pressure reaction of tetramethylsilane (TMS) in a stainless steel autoclave at 1000 ^oC allowed to prepare SiC with also high surface area (636 m^2g^{-1}), high chemical purity (carbon content close to theoretical value) and disordered pore system (Chapter 0).

An inverse replica of SBA-15 was obtained in the case of the polycarbosilane derived materials (Chapter 4.1.2). This was confirmed by low angle X-ray diffraction, nitrogen physisorption (narrow pore size distribution with maximum pore diameter of 3 nm) and transmission electron microscopy. Thus specific surface areas for ordered mesoporous silicon carbide were highest reported until now in literature (640-800 m^2g^{-1}), but on the other hand, some free carbon impurities were also detected.

Moreover, the thermal stability of silicon carbide materials was significantly better than that of the silica template (SBA-15), but not as good as that of the ordered mesoporous carbon CMK-1.

In the next paragraph (4.2) it is shown how ordered mesoporous silica can be used for preparation of highly dispersed metal particles. In contrast to nanocasting principle presented here, the aim was not to fill the pores completely but to develop a simple in-situ procedure for the preparation of highly dispersed metal (Pt, Pd, V) species.

4.2   Incorporation of Metal and Metal Oxide Particles into MCM-41 and SBA-15 via Efficient In-situ Procedure

In this chapter, a new approach to prepare in one step well dispersed platinum nanoparticles predominately inside the pores of MCM-41 is presented. A solution of a platinum precursor in a hydrophobic, non-polar solvent ($Pt(acac)_2$ in toluene) was used and injected inside the hydrophobic core of the surfactant micelles used as a template for the MCM-41 structure, before addition of the silica source [Scheme 6 – step 1].
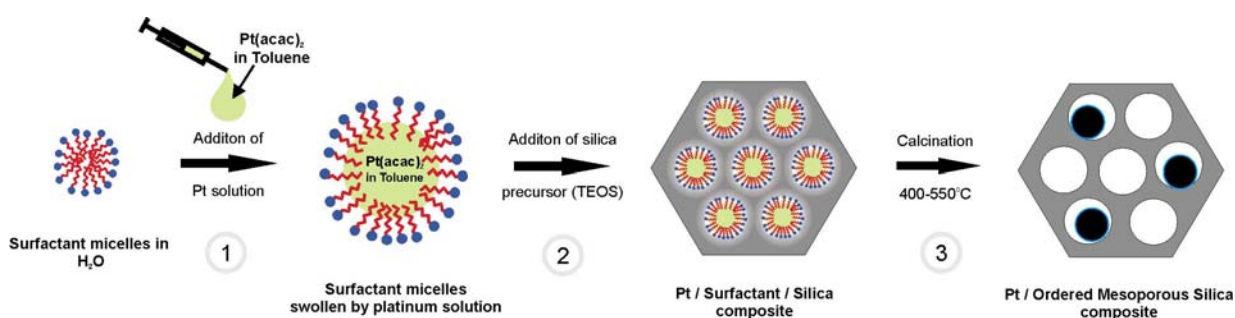
Scheme 6. Schematic illustration of the *in-situ* Pt/MCM-41 preparation.

Since both $Pt(acac)_2$ and toluene did not mix with water, they were dissolved in the inner hydrophobic core of the micelles, which resulted in a high degree of incorporation. Thus, 80-100 % of the precursor was incorporated in the final material. In the as synthesized Pt/surfactant/MCM-41 composite material, surfactant removal was catalytically enhanced due to the presence of platinum resulting in a lower calcination temperature needed as compared to pure MCM-41.[182, 183] Catalytic template removal was also observed by Montes et al.[184] who added platinum to the as synthesized MCM-41 material before calcination. The method presented here is widely applicable to other metal or metal oxide containing silica systems such as Pd/MCM-41, V_2O_5/MCM-41 and Pt-SBA-15, using the same procedure and acetylacetonates as precursors. Especially palladium-loaded MCM-41 was found to be a good hydrogenation catalyst in the cinnamic acid hydrogenation, but also vanadium containing silica was a promising catalyst in a number of reactions.[185-187]

4.2.1   In-situ Pt-incorporation into MCM-41 Materials

In a typical synthesis procedure, a solution of CTABr (surfactant) in H_2O and NH_3 was used. Subsequently, appropriate amounts of Pt(II)acetylacetonate in toluene [Table 9] were added [Scheme 6 – step 1]. After adding TEOS [Scheme 6 – step 2] the solid was isolated by filtration, washed with water and calcined at 450 ^oC [Scheme 6 – step 3]. The choice of Pt(acac)$_2$ as a precursor (acac=acetylacetonate) and toluene as swelling agent was not arbitrary. Due to the lack of solubility in water, Pt(acac)$_2$ preferentially dissolved in the toluene phase. Toluene could dissolve reasonably high amounts of this Pt precursor (up to 3.2 wt% at 70 ^oC) and also did not mix with water. In this approach (depending on the loading and precursor concentration) 80 to 100 % of the platinum was incorporated into MCM-41 [Table 9], avoiding losses of this expensive metal during the synthesis.

Table 10. Synthesis conditions and characterization of platinum containing MCM-41 materials.

Sample code		Amount of Pt solution added[a] [mL]	Theroretical/measured Pt loading [wt%]	Pt Yield[e] [%]	Surface area [m^2g^{-1}]
M-0	MCM-41	-	-		1189
M-1	0.4 wt% Pt	0.4[b]	0.39/0.39	100	1190
M-2	1 wt% Pt	1[c]	0.99/0.79	80	1126
M-3	1 wt% Pt	2[d]	0.99/0.86	87	1098
M-4	2 wt% Pt	2[c]	1.97/1.69	86	1073

a) Per 1.2 g of CTABr and 5 g TEOS used b) 2.4 wt% Pt(acac)$_2$ in toluene solution c) 3.2 wt% Pt(acac)$_2$ in toluene solution d) 1.6 wt% Pt(acac)$_2$ in toluene solution e) Pt yield determined using ICP-OES

For highly saturated solutions of the precursor, a lower platinum incorporation was observed (Table 9, M-2 and M-4), while for more diluted solution of Pt(acac)$_2$ (M-3) and lower loading (M-1) almost all platinum was incorporated. This could be due to the presence of ethanol in the solution after addition of TEOS. Ethanol increased the solubility of Pt(acac)$_2$ outside the micelles and therefore caused leaching of the metal complex. The volume of the Pt(acac)$_2$/toluene solution, that was solubilized by CTABr micelles was limited. Higher loadings (2 wt% - M-4 sample) also caused a decrease in pore ordering. This was clearly visible in low angle X-ray diffractograms [Figure 42a]. For sample M-4 with 2 wt% Pt, only one broad (100) peak could be observed and the (110) and (200) reflections disappeared. However, in the case of 1 wt% loading of platinum (M1) no loss of the ordering was observed as compared to pure MCM-41 and three reflections of the hexagonal structure were discerned. Increasing the Pt/toluene loading also caused a significant increase of the (100) lattice spacing as expected for the addition of swelling agents.[28]
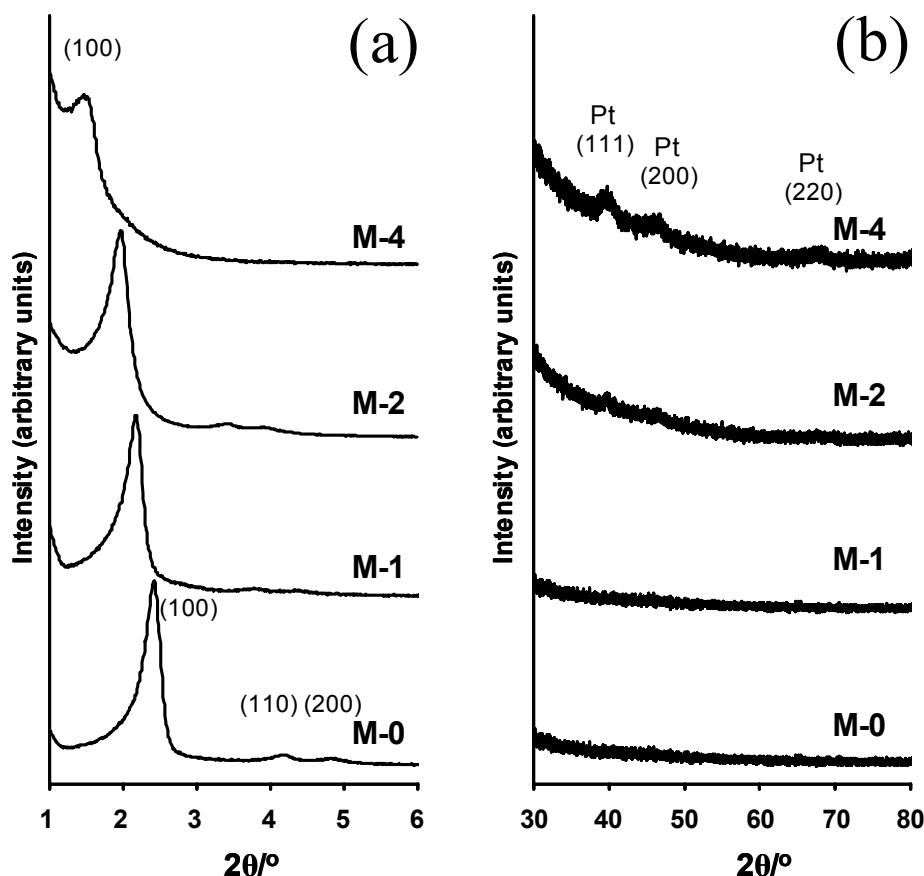
Figure 42. (a) Low and (b) high angle XRD of Pt/MCM-41 samples. M-0 is a pure MCM-41, while M-1, M-2 and M-4 are Pt/MCM-41 materials with different metal loading [Table 9]. The presence of nanocrystalline Pt was detected for M-4 and M-2.

TEM micrographs further confirmed this conclusion. Comparing Figure 43a and Figure 44a, ordering of the pores in sample M-2 was significantly better than that of M-4. The micrographs also showed the incorporated Pt nanoparticles (dark spots) inside the channels of MCM-41 and no large particles were found outside. The average particle size was estimated to be 3.0 nm in the case of M-2 [Figure 43b] and 4.2 nm in the case of M-4 [Figure 44b]. These values were in good agreement with the measured pore diameter of the silica matrix calculated from nitrogen physisorption isotherms measured at 77 K (3.3 nm pore diameter for 1 wt% Pt sample (M2) and 3.7 nm pore diameter for 2 wt% Pt sample (M4) – BJH desorption) [Figure 45]. No significant decrease in the surface area as compared to standard MCM-41 (1190 m^2g^{-1}) was observed in all Pt/MCM-41 samples. For the sample with the highest 2 wt% Pt loading, a surface area of 1073 m^2g^{-1} was measured.
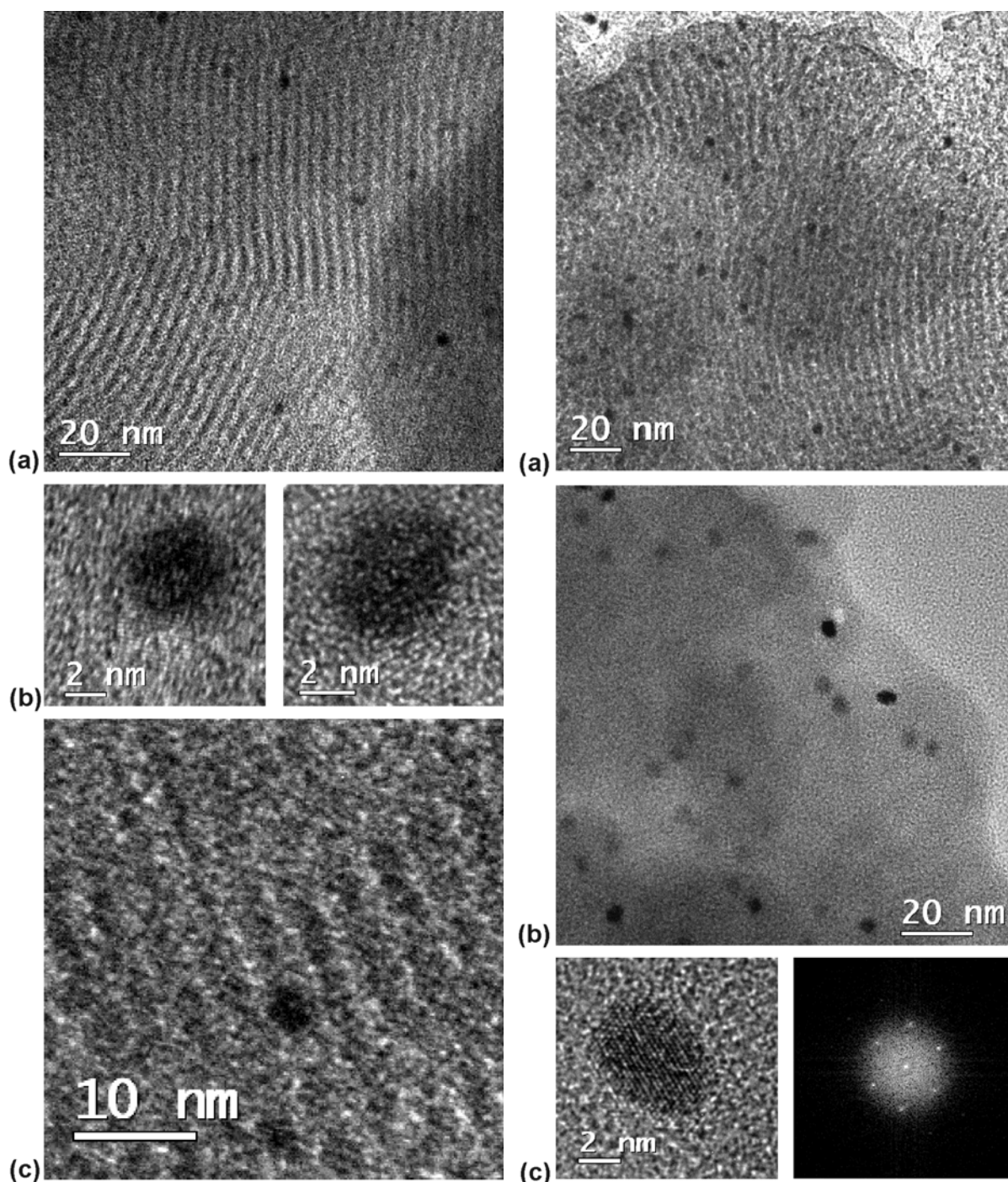
Figure 43. (a) Overview transmission electron micrograph of sample M-2 with 1 wt% Pt/MCM-41. Platinum particles (dark) are statistically embedded within bent silica pore walls (periodicity ~ 3.9 nm).(b)High resolution TEM micrographs of M-2 displaying single platinum nanoparticle with (111) lattice fringes corresponding to about 2.24 Å. (c) Magnified image of a single nanoparticle integrated in the nanoporous host.

Figure 44. (a) Defocused overview TEM image of sample M-4 with 2 wt% Pt/MCM-41 and a periodicity of about 4.4 nm. (b) In-focus overview TEM image of sample M-4 with 2 wt% Pt/MCM-41. Under in-focus conditions only platinum nanoparticles are visible. High-resolution TEM micrograph and fast Fourier transform (FFT) of M-4 displaying a single Pt-nanoparticle with (111) and (200) lattice fringes corresponding to about 2.27 Å and 1.92 Å.
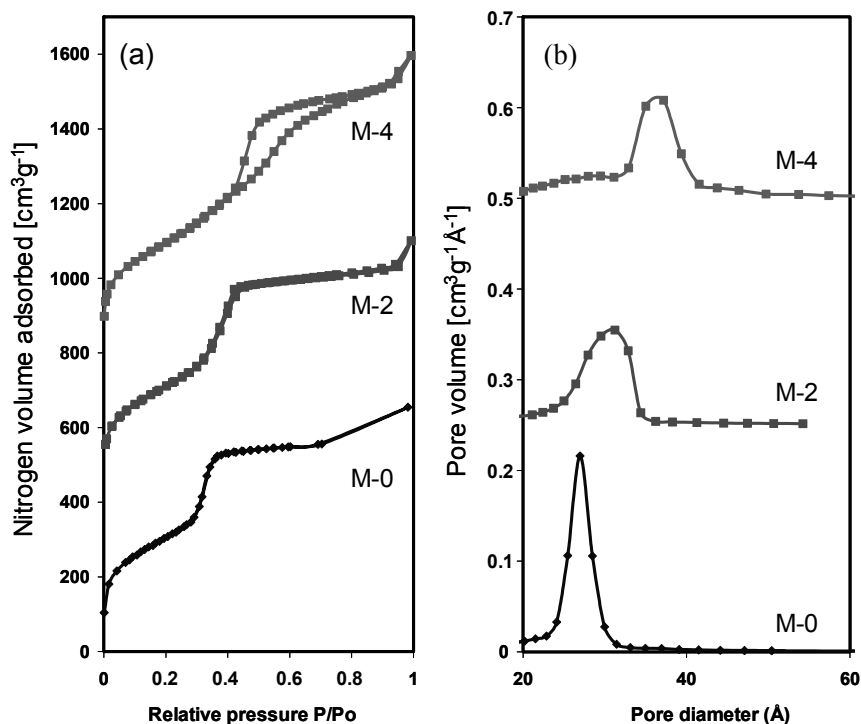
Figure 45. (a) Nitrogen physisorption isotherms of pure MCM-41 (M-0) and Pt/MCM-41 samples (M-2 and M-4) measured at 77K (with 200 cm^3g^{-1} offset). (b) BJH pore size distribution calculated from the desorption branch of the nitrogen physisorption isotherms (with 0.25 $cm^3g^{-1}Å^{-1}$ offset)

Wide angle X-ray diffractograms showed the presence of cubic metallic platinum in samples with high Pt loading [Figure 42b]. Reduction to Pt^0 was also confirmed in the XPS spectra ($Pt4f_{7/2}$: 70.5 eV) [Figure 46].[188]
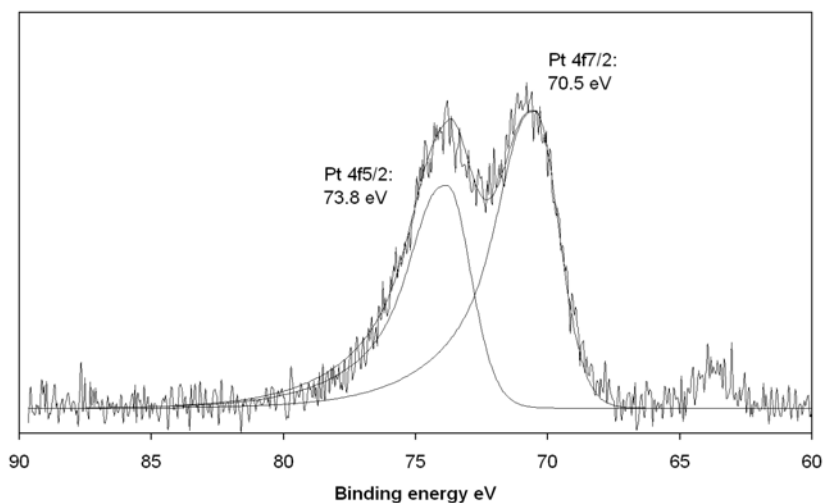
Figure 46. XPS spectra of the M-2 sample (1wt% Pt/MCM-41). The position of Pt $4f_{7/2}$ peak at 70.5 eV suggests complete Pt reduction to Ptº

4.2.2 In-situ Synthesis of Pd/MCM-41, Pt/SBA-15, and V$_2$O$_5$/MCM-41

The general method of injecting the hydrophobic platinum precursor into micelles during the synthesis of MCM-41 materials was extended to other metals (Pd, V) and other ordered mesoporous materials such as SBA-15. In the original synthesis scheme, Pt(acac)$_2$ was replaced by Pd(acac)$_2$ [Scheme 6 – step 1] and Pd/MCM-41 was made according to the same procedure [Scheme 6]. The acetylacetonate of palladium was also insoluble in water and injection using a toluene solution resulted in 88 % of metal incorporation [Table 10 – sample P-1]. On the other hand, less palladium could be dissolved in toluene (1.8 wt% at 70 ^{o}C) and loading of the final composite material was generally lower (0.3 wt%). Another example can be the incorporation of vanadium. In this case V(acac)$_3$ was used as a precursor. However, this compound also dissolves in water. Thus, a direct comparison was made using the precursor dissolved in toluene (V-1) and in the surfactant solution with water (V-2) (Table 10). For sample V-1, the vanadium precursor was dissolved in toluene and a high incorporation of vanadium (96 %) was measured after the synthesis. However, solubilization of the same vanadium precursor in water (sample V-2) resulted in an incorporation as high as 81 %. This was due to the nature of vanadium integrating into the silica network in contrast to platinum, even for low concentrated solutions.[187, 189-191] Interestingly, vanadium containing materials showed color changes with changing temperature and atmosphere. Directly after calcination in air materials were white, but after a few hours of exposing to air, the color was changed to yellow (due to coordination of water to silica incorporated vanadium oxide species). Such samples if heated in vacuum at 80 ^{o}C changed color to green and then grey, suggesting a change of the oxidation state of vanadium.

**Table 11.** Synthesis conditions and characterization of mesoporous composite materials. Pure SBA-15 (S-0) and platinum incorporated SBA-15 samples are marked as samples S-1 and S-2). Vanadium (V-1 and V-2) and Palladium (P-1) containing MCM-41 materials are also listed.

Sample code		Amount of metal solution added [mL]	Theoretical/measured metal loading[e] [wt%]	Metal yield[e] [%]	Surface area [m^{2}g^{-1}]
S-0	SBA-15	-	0	-	786
S-1	1 wt% Pt	1[a]	0.99/0.48	48	825
S-2	2 wt% Pt	2[a]	1.99/1.17	59	824
V-1	1.4 wt% V	1[b]	1.35/1.33	96	1187
V-2	1.4 wt% V	-[c]	1.35/1.13	81	1056
P-1	0.3 wt% Pd	1.8[d]	0.34/0.30	88	1100

a) Per 2.41 g of P123 block copolymer and 5 g TEOS used. 3.2 wt% Pt(acac)$_2$ solution in toluene was added, b) Per 1.2 g of CTABr and 5 g TEOS used. As vanadium source 13.8 wt% V(acac)$_3$ solution in toluene was added, c) 0.14 g of V(acac)$_3$ added directly to water/surfactant mixture before synthesis – without toluene, d) 1.8 wt% Pd(acac)$_2$ solution in toluene was added, e) metal loading after synthesis was confirmed by ICP-OES (from Si/V ratio, assuming the V$_2$O$_5$ formation)

In wide angle X-ray diffraction patterns no crystalline particles of vanadium oxide were detected, confirming a high dispersion of vanadium oxide on silica support.

Incorporation of platinum into the pores of SBA-15 was less successful. Addition of platinum caused severe decrease of pore ordering as compared to the toluene-free system, and only one reflection at low angle could be observed in X-ray diffractograms. Even for S-1 with only 1 ml of platinum/toluene solution added, the (110) and (200) reflections of the hexagonal structure were not observed. However, the position of the (100) peak was shifted to lower 2θ values, if the precursor solution was added. The specific surface area (S-2: 824 m^2g^{-1}, S-1: 825 m^2g^{-1}) was comparable to that of pure SBA-15 (S-0: 786 m^2g^{-1}). The lower incorporation could be attributed to the extended time needed for the synthesis of SBA-15 (28 h), as compared to the synthesis of platinum containing MCM-41 (1 h). The long time required for SBA-15 synthesis allowed the Pt(acac)$_2$ precursor to diffuse from toluene to ethanol/water mixture resulting from tetraethylorthosilicate hydrolysis. A platinum incorporation of 48 % for sample S-1 and 59 % for S-2 was achieved. However, the surface areas of these materials were high [Table 10] and comparable to those of pure SBA-15. Nitrogen adsorption isotherms [Figure 47] of platinum containing samples, show hysteresis loops much broader than in the case of Pt-free SBA-15 (S-0). This may be caused by pore blocking by Pt particles or by structural changes (due to the presence of swelling agent) in the SBA-15, leading to the formation of a bottle-neck-like pore geometry.
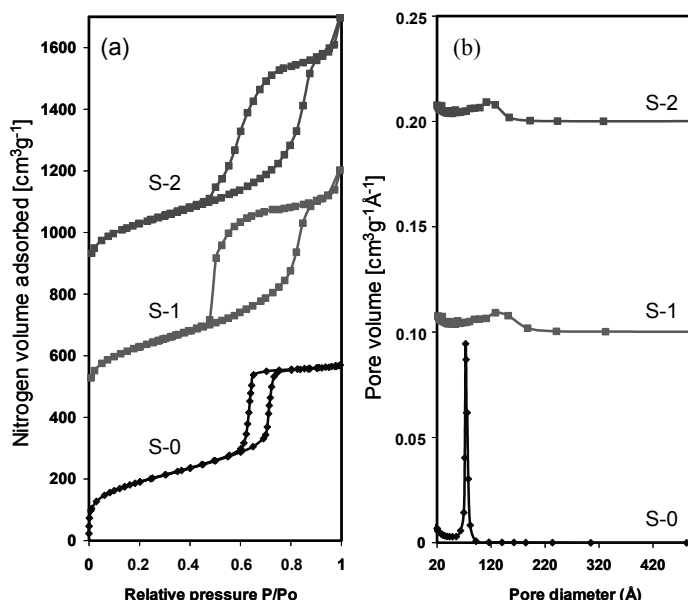
Figure 47. (a) Nitrogen physisorption isotherms of the pure SBA-15 and Pt/SBA-15 samples with different metal loadings (S-1, S-2), measured at 77K (with 200 cm^3g^{-1} offset), (b) BJH pore size distribution calculated from the adsorption branch of the isotherm (with 0.1 $cm^3g^{-1}Å^{-1}$ offset)

4.2.3 Pt-catalyzed Template Removal

For a Pt-free MCM-41 material, the surfactant was typically removed by calcination at a temperature of 540 °C[1, 167] [Scheme 6 – step 3]. There are other known template removal procedures[192] such as solvent extraction,[193, 194] or ozone treatment,[195] but often complete removal was not achieved. The calcination behavior critically depends on parameters such as the surfactant chain length, the type of oxide phase and the atmosphere.[182, 196] According to TG/MS and DSC measurements in air, three steps are distinguished.[182, 183] In the first decomposition step, at temperatures between 150 and 250 °C, Hofmann degradation of the template into trimethyl amine and hexadecane occurs. In the range of 250 and 300 °C exothermic cracking of the long chain hydrocarbons takes place followed by oxidation at temperatures exceeding 320 °C. Typically, the template removal is complete at 550 °C. Comparing the calcination process for M-0 and M-4 [Figure 48A and Figure 48B], the removal of the template in the platinum-containing sample started at the same temperature as for the platinum-free material, but complete removal was achieved at significantly lower temperatures (400 °C) as compared to M-0 (550 °C).
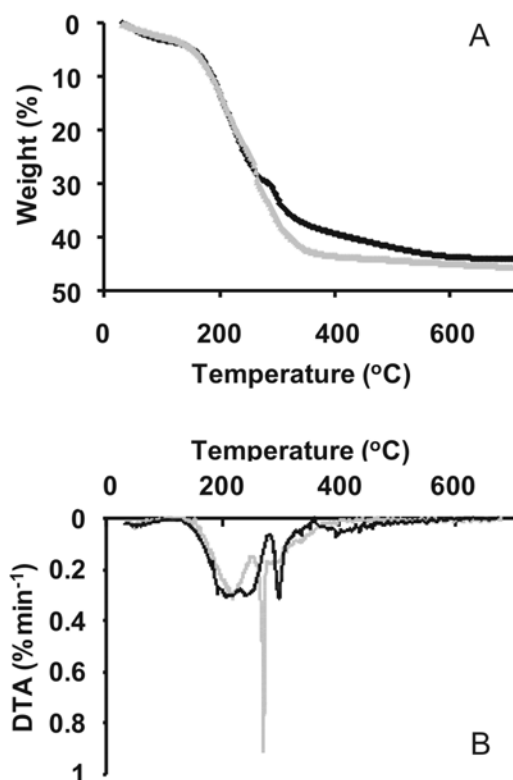
Figure 48. TG (A) and DTG (B) calcination curves of pure MCM-41 (M-0, black) and 2 wt% platinum containing MCM-41 (M-4, grey) in air (heating rate of 3 °Cmin[-1]).

Species evolving during heat treatment were also released at different temperatures. Fragments resulting from cracking of the large chain hydrocarbons were released up to 350 ^{o}C[182] (C_3H_6: m/z=42, C_4H_7: m/z=55). This was also observed in the case of the M-0 sample [Figure 49]. One or two broad overlapping peaks are present on m/z=42 and 55 in between 150 and 290 ^{o}C and one centered at 320 ^{o}C. This was observed for all cracking products in the case of all surfactant hydrocarbon chain lengths.[182] However, in the case of platinum-containing material (M-4) only one peak in between 150 and 260 ^{o}C was present [Figure 49 m/z=55, 42]. At 270 ^{o}C large amounts of CO_2 (m/z=44) were detected as compared to M-0, suggesting that the cracking products were immediately oxidized by the integrated platinum-catalyst to form CO_2, or direct oxidation of long chain alkanes took place. Also H_2O formation increased at this temperature. The TG/MS experiments show that platinum, located inside the pores, acts as an oxidation catalyst. The lower calcination temperatures feasible due to the presence of the Pt-particles could provide a new way for the manufacture of mesoporous transition metal oxides that often tend to collapse at higher temperatures due to crystallization processes or low melting temperatures. The method could also improve the preparation of mesoporous silica films due to the decrease of stress and strain in between the substrate and porous silica layer developing in the calcination process. However, in the case of silica, low calcination temperatures may result in lower densification of silica and subsequently lower hydrothermal stability.
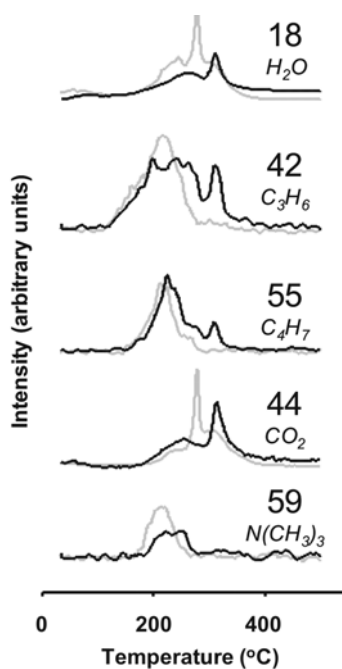
Figure 49. Combustion products detected by mass spectrometry during the TG measurements in air as a function of temperature. Black lines correspond to the M-0 (pure MCM-41) and grey curves to the M-4 (with 2 wt% Pt) sample. Numbers indicate the m/z ratio of species evolved and the corresponding product.

4.2.4 Catalytic Properties: Hydrogenation of Cinnamic Acid

Hydrogen chemisorption studies on in-situ synthesized Pt/MCM-41 demonstrated the principle accessibility of the platinum inside the mesoporous channels. A metal dispersion (fraction of active surface metal atoms) of 24 % was measured for M-2 with 1 wt% Pt loading. Further catalytic characterization was performed using a model hydrogenation reaction of cinnamic acid to hydrocinnamic acid under heterogeneous conditions [Scheme 7].

Scheme 7. Hydrogenation of cinnamic acid

After 90 minutes of reaction, the platinum containing MCM-41 (M-2) showed 16 % conversion and 100 % selectivity towards hydrocinnamic acid. The time required for full conversion was 660 min. However, in the case of the Pd/MCM-41 catalyst (P-1 - Table 11) this reaction was much faster and after the same time (90 min) 100 % of conversion of the acid was observed (with 100 % selectivity). In comparison, a commercially available catalyst (5 wt% palladium supported on carbon – C-1), showed full conversion (with 100 % selectivity) already after 18 min, but in that case the metal loading was also 16 times higher than in the case of P-1. A blank experiment carried out without catalyst showed no conversion, even after one day of hydrogen treatment. The highest specific reaction rate (calculated per gram of metal catalyst) was observed for Pd/MCM-41 (P-1, 0.70 mmolg^{-1}s^{-1}) and was significantly higher than that for the commercial C-1 catalyst (5 wt% Pd/carbon, 0.21 mmolg^{-1}s^{-1}). For the platinum containing sample M-1 a lower specific reaction rate was observed (0.05 mmolg^{-1}s^{-1}) as compared to both palladium catalysts.
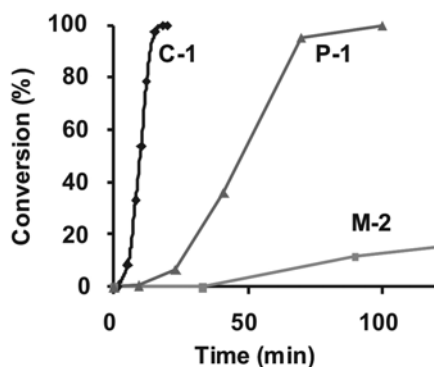
Figure 50. Catalytic conversion of cinnamic acid under heterogeneous conditions (at 25 ^{o}C). Samples containing platinum (M-2 – 1 wt%) and palladium (P-1 – 0.3 wt%) were compared to commercially available (C-1) 5 wt% palladium supported on carbon catalyst.

4.2.5   Conclusions

Summarizing, a new one-step, in-situ preparation procedure for platinum-containing MCM-41 was developed. The highly porous material shows well dispersed platinum metal predominately confined inside the pores of the mesoporous silica. Particles outside the pore system were not detected using transmission electron microscopy. The confined Pt particles catalyze the removal of surfactant from the MCM-41 and allow calcination at lower temperatures. The in situ method presented can be widely applied for the incorporation of other metals or oxides (such as Pd or V_2O_5) into MCM-41 and large pore silica such as SBA-15. A high catalytic activity was observed for Pd/MCM-41 catalyst in the hydrogenation of cinnamic acid under heterogeneous conditions. Moreover, this method can be easily applied for other metal/mesoporous oxide systems since no interaction between metal oxide and platinum precursor exists during the synthesis.

In the next chapter it will be shown that in-situ prepared V_2O_5/MCM-41 materials are suitable substrates for the preparation of highly dispersed VN/MCM-41 catalysts via nitridation in ammonia flow. Compared to supported nitrides prepared from V_2O_5/MCM-41 materials, via the ex-situ procedure they show similar high catalytic activity in propane dehydrogenation, despite significantly lower vanadium content.

4.3 Supported Vanadium Nitride and Carbide Catalysts Prepared from V₂O₅/Ordered Meosporous Silica (OMS) Composite Substrates

In the previous chapter, an efficient method for the preparation of supported metals and metal oxides was developed. Here it is shown how such V_2O_5/OMS composite materials can be used for the preparation of supported nitrides and carbides. For comparison different preparation procedures (in-situ, ex-situ) of supported vanadium oxide were used [Scheme 8].
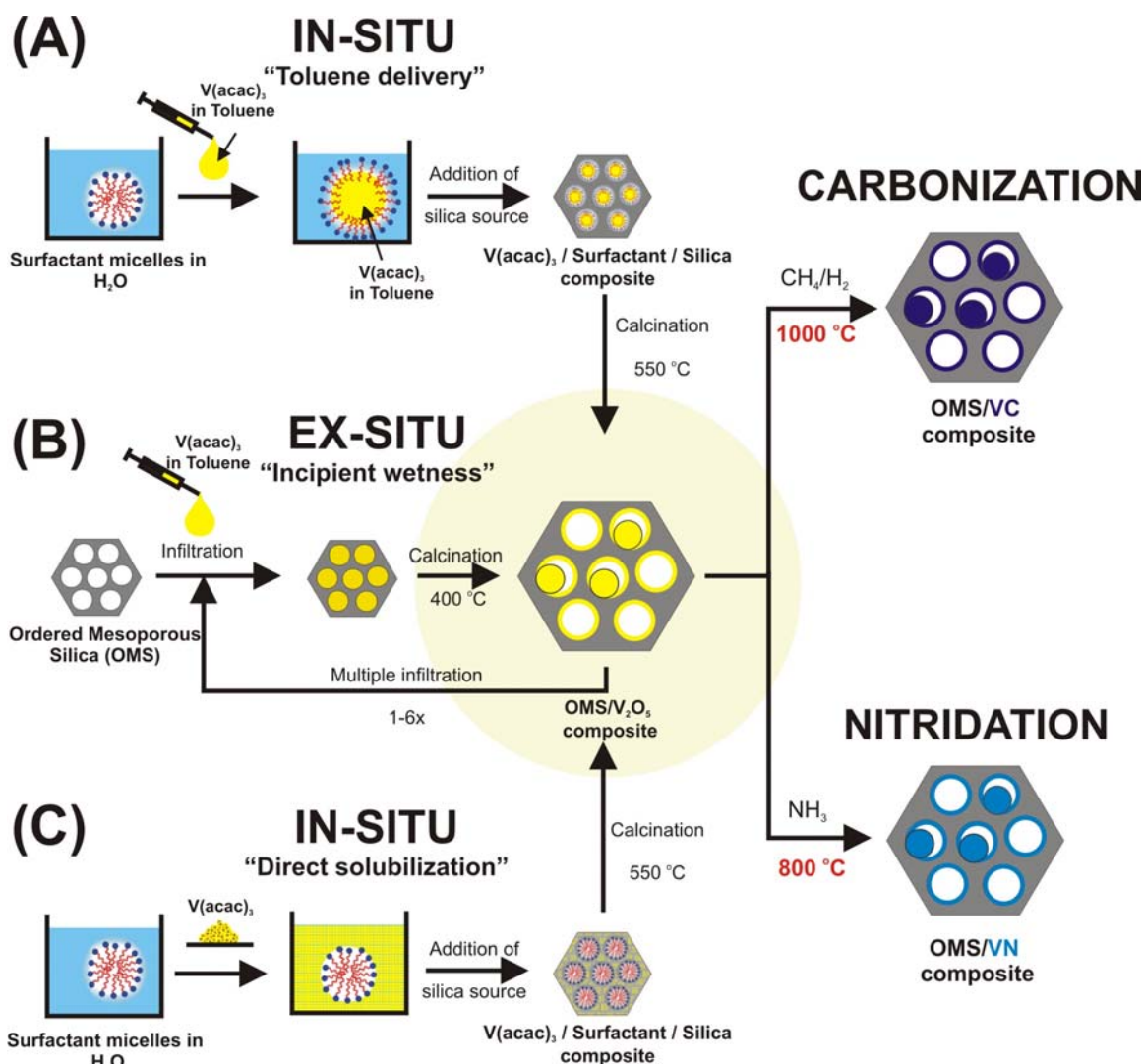
Scheme 8. Supported vanadium nitride and carbide prepared from the in-situ and ex-situ synthesized V_2O_5/OMS.

The in-situ procedure presented in chapter 4.2 used toluol as a transport medium for V(acac)₃ [Scheme 8A] or direct solubilization of the same vanadium precursor in the surfactant/water solution [Scheme 8C]. The ex-situ procedure (by incipient wetness impregnation of porous silica - Scheme 8B) was used for comparison as a method for

preparation of materials with high vanadium oxide content. Moreover, the ex-situ procedure was also tested for the preparation of vanadium nitride and carbide supported on large pore silica SBA-15 and activated carbon NORIT-A. After synthesis and characterization, some of the materials were tested as catalysts for non-oxidative propane dehydrogenation.

4.3.1 VN/MCM-41 via Nitridation of In-situ Prepared V_2O_5/MCM-41 Composites

In-situ preparation and characterization of V_2O_5/MCM-41

In-situ prepared V_2O_5/MCM-41 composites were used as substrates for the preparation of supported VN/MCM-41. Two different procedures to incorporate the vanadia species into the mesoporous silica matrix during synthesis and two different amounts of V_2O_5 precursor ($V(acac)_3$) were used [Table 11]. In the first one, toluene was employed as an efficient delivery agent for the vanadia precursor during synthesis (samples IVN-1 and IVN-3)[Scheme 8A] while in the second one the vanadia precursor was dissolved directly in the surfactant/water solution before synthesis of ordered mesoporous silica (samples IVN-2 and IVN-4)[Scheme 8C]. One additional sample was prepared combining both procedures in order to maximize the vanadium loading in the composite materials (IVN-5). The toluene assisted delivery method was more efficient and vanadium yields were higher by 15 (for IVN-1) and 20% (for IVN-3) as compared to the samples prepared via direct solubilization of the same amount of precursor in water/surfactant solution (IVN-2 and IVN-4 respectivly) [Table 11]. Material prepared via the combined procedure (toluene delivery + solubilization in water) showed also a high yield of vanadium incorporation (89%) and the highest vanadium content (4.95 wt.%) among the in-situ prepared V_2O_5/MCM-41 materials.

Table 12. Preparation of VN/MCM-41 materials from in-situ synthesized V_2O_5/MCM-41 substrates

Sample code	$V_{solution}$[a) [ml]	m_{metal}[b) [g]	Theoretical/measured vanadium content[c) [wt.%]	Vanadium yield [%]	S_g^{oxide} [m^2g^{-1}]	$S_g^{nitride}$ [m^2g^{-1}]	N content after nitridation [wt.%]
IMCM-41	-	-	-	-	1075	1062	3.2*
IVN-1	1	-	1.35/1.33	96	1097	750	n.a.[d)
IVN-2	-	0.14	1.35/1.13	81	1056	644	n.a.[d)
IVN-3	2	-	2.78/2.52	91	1226	964	0.9**
IVN-4	-	0.28	2.78/1.98	71	1292	810	3.6*
IVN-5	2	0.28	5.56/4.95	89	1057	664	1.4**

a) Volume of 13.8 wt% $V(acac)_3$ in toluene (1ml solution contains 0.14g $V(acac)_3$) added during the synthesis, b) mass of the $V(acac)_3$ precursor added during the synthesis c) vanadium content measured via ICP-OES and calculated from the V/Si ratio, assuming the V_2O_5 formation on SiO_2, d) data not available
*   measured via hot gas extraction method 1-2 weeks after synthesis (stored in air atmosphere)
**   measured via hot gas extraction method 50-55 weeks after synthesis (stored in air atmosphere)

The specific surface areas for the oxide materials were in the range of 1056-1292 m^2g^{-1}. Surprisingly, materials with an average vanadium content (IVN-3 and IVN-4) had a higher specific surface area (1226 and 1292 m^2g^{-1}) than the vanadium-free MCM-41 materials [Table

11]. Lower surface areas were measured for the samples with highest (INV-5: 1057 m^2g^{-1}) and lowest vanadium content (IVN-1 and IVN-2: 1097 and 1056 m^2g^{-1}). Physisorption measurements showed also that the materials prepared via the toluene route had a broader pore size distribution and larger pores [Figure 51 – IVN-3] than the samples prepared via the direct solubilization procedure [Figure 51 – IVN-4].
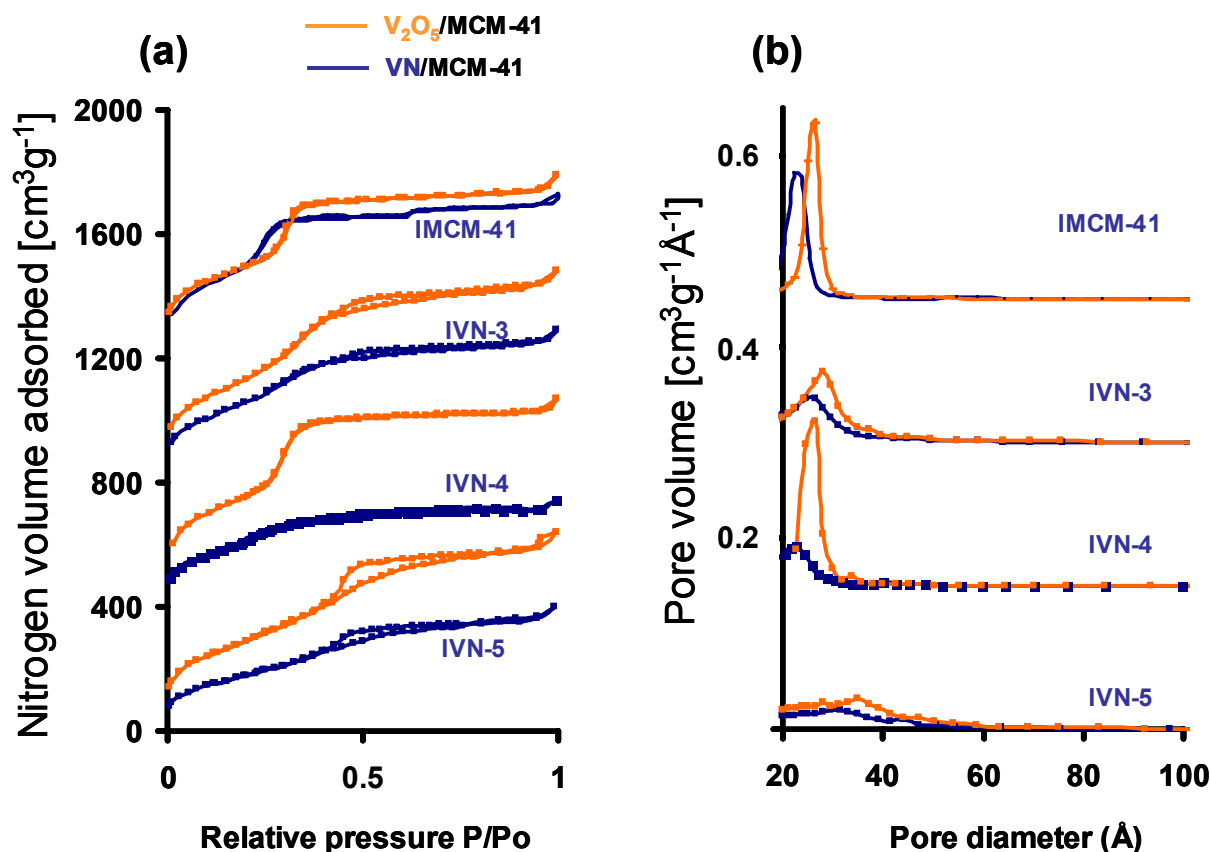
Figure 51. (a) Nitrogen physisorption isotherms of MCM-41 and supported vanadium oxides before (orange) and after (dark blue) nitridation (with 400, 800 and 1200 cm^3g^{-1} offset). BJH pore size distribution calculated from the adsorption branch of the nitrogen physisorption isotherms (with 0.15 $cm^3g^{-1}Å^{-1}$ offset)

Similar conclusions could be drawn by the analysis of the low angle X-ray diffraction patterns [Figure 52]. Well ordered hexagonal pore symmetry with three reflections in the diffraction pattern was detected for IVN-4 prepared via direct vanadium precursor solubilization. If, toluene was used as delivery agent, for the same amount of vanadia precursor, ordering of the pores significantly decreased and only one broader reflection was observed [Figure 52 – IVN-3]. This was reasonable due to high amount of the swelling agent present in the solution. The lowest pore ordering was observed for the material synthesized via the combined direct solubilization and toluene delivery method. Only a very broad peak with the lowest intensity among all samples could be observed [Figure 52 – IVN-5]. According to

the high angle X-ray diffraction measurements, all V_2O_5/MCM-41 composites were amorphous and no reflection of any crystalline phase was detected, suggesting uniform incorporation of V_2O_5 inside the MCM-41 pores.
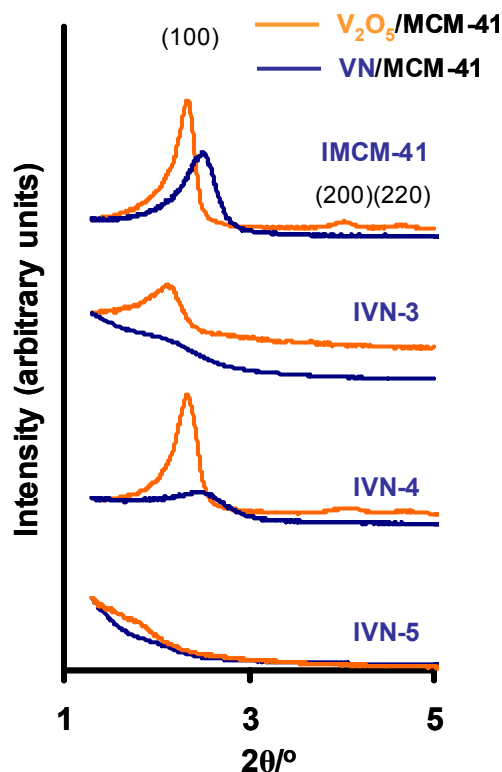
Figure 52. Low angle X-ray diffraction patterns of pure MCM-41 and V_2O_5/MCM-41 composites before (orange) and after (blue) nitridation.

Nitridation of in-situ synthesized V_2O_5/MCM-41 for the preparation of VN/MCM-41 materials

As prepared V_2O_5/MCM-41 composites were subjected to nitridation in ammonia flow at 800°C. After cooling down to room temperature the materials were passivated in O_2/N_2 gas mixture (1%O_2) in order to prevent rapid oxidation in contact with air. For comparison, also vanadium-free MCM-41 was nitrided in the same conditions. An elemental analysis of sample IVN-4 made shortly after nitridation, showed a nitrogen content of 3.6 wt.%, while for nitridation of pure silica (IMCM-41) a lower amount of nitrogen was detected (3.2 wt.%) [Table 11]. This was in good agreement with the results of Asefa et al. who studied ammonolysis of MCM-41 and periodic mesoporous organosilica in similar conditions.[197] For two other samples, the elemental analysis was performed after one year storage in air atmosphere, showing significantly lower nitrogen content due to oxidation and hydrolysis (0.9 wt.% N for IVN-3 and 1.4 wt.% N for IVN-5). However, the basic relation between the

vanadium loading and nitrogen content was similar (the sample with higher vanadium loading – IVN-5, had also a higher nitrogen content). The oxidized samples changed also color from the initial black-gray to almost white after one year showing that the oxidation state of metal or its coordination chemistry was changed.

According to nitrogen physisorption measurements [Figure 51a] in high temperature specific surface areas of all vanadium containing materials decreased due to nitridation by 15 to 39 % [Table 11]. Materials prepared via toluene delivery retained relatively high surface areas as compared to V_2O_5/MCM-41 oxide precursors (reduction by 15 and 31 % of the original surface area for IVN-3 and IVN-1 respectively), while samples prepared via direct solubilization were prone to more severe sintering (reduction by 38 and 39 % of the original surface area for respectiviely IVN-4 and IVN-2). A similar decrease of surface area was observed for IVN-5 with the highest vanadium loading (reduction of supported oxide surface area by 37 %) For the nitridation of vanadium-free MCM-41, the specific surface area did not change significantly (decreased by 1%).

According to the BJH calculations [Figure 51b], during the nitridation process, the pore diameter decreased in the case of all samples to lower values. For pure MCM-41, the diameter changed from 2.6 to 2.3 nm. In the case of vanadium containing materials, the degree of pore shrinkage was dependent on the preparation method and vanadium content. For materials with low vanadium content, the shrinkage of the pore diameter by 10 and 11 % for IVN-1 and IVN-2 was observed, while for materials with high vanadium content shrinkage of 6 and 14% for IVN-3 and IVN-4 was measured. Materials prepared by direct solubilization method showed a higher degree of shrinkage, especially for high vanadium content (IVN-4), than the ones prepared via toluene delivery (IVN-3).

This could be an effect of different nature of vanadium incorporation. For vanadium directly dissolved in the water/surfactant mixture (IVN-2 and 4), one can expect that vanadium was uniformly incorporated in the bulk silica pore walls of MCM-41 materials. In the case of toluene delivery, one could expect that metal species were incorporated iniside the pores after the calcination of surfactant and were distributed as particles or as the pore wall coating (therefore not incorporating uniformly in the bulk pore wall). The presence of vanadium in the pore walls could significantly lower the thermal stability of mesoporous material and destabilize it under reducing conditions. Therefore, materials prepared via toluene delivery route showed a lower degree of sintering (loss of surface area and decrease of the pore diameter) during the nitridation process.

These conclusions were confirmed by low angle X-ray diffraction patterns where ordering of the IVN-4 sample prepared via direct solubilization was significantly reduced due to nitridation process [Figure 52]. The nitrided sample showed a reduced structural ordering and shrinkage as compared to IVN-3 [Figure 52]. The material prepared via combined procedures showed only extremely broad reflections before and after nitridation. In the high angle area of X-ray diffraction patterns no reflections were observed, excluding the formation of large VN particles outside the pore system.

4.3.2 Supported VN and VC via Nitridation/Carbonization of V_2O_5 supported on Mesoporous Silica and Activated Carbon via Ex-situ Preparation Procedure

In order to obtain a higher loading of VN in MCM-41, a multiple ex-situ infiltration procedure was also used to prepare the V_2O_5/MCM-41 composites [Scheme 8B]. Additionally in this papragraph, V_2O_5 was also supported on the large pore SBA-15 silica and microporous activated carbon NORIT-A. These were also tested for preparation of supported VC materials via carbonization in CH_4/H_2 gas mixture at 1000^oC.

Ex-situ supported V_2O_5 characterization

Materials were prepared via multiple incipient wetness impregnation of porous supports with $V(acac)_3$ in toluene (as an exception in the case of EM-VN-3 sample, a solution of NH_4VO_3 in H_2O_2 was used). In the case of MCM-41 materials, infiltration with V_2O_5 resulted in a decrease of the specific surface area [Table 12]. Higher loadings resulted in lower specific surface areas (EM-VN-1 and EM-VN-2), while the sample prepared via infiltration from H_2O_2 solution showed pore blocking and even more drastic reduction of the surface area $134 m^2g^{-1}$ (as compared to EM-VN-2 sample with similar vanadium loading and $673 m^2g^{-1}$ surface area). This was probably an effect of a vanadium precursor solution which was pushed out from the mesopores due to the constant decomposition of H_2O_2 to gaseous O_2 and H_2O in the presence of vanadium species. It is known that vanadium forms peroxocompounds like $V(O_2)_4^{3-}$, $VO_2(O_2)_2^{3-}$ when reacted with H_2O_2.

Table 13. Ex-situ prepared VN and VC supported on ordered mesoporous silica and activated carbon supports

Sample code	Support	$S_g^{support}$ [m^2g^{-1}]	Vanadium content[a] [wt.%]	$S_g^{V2O5 / support}$ [m^2g^{-1}]	$S_g^{nitride\ or\ carbide}$ [m^2g^{-1}]	N content [wt.%]	C content [wt.%]	O content [wt.%]
EM-VN-1	MCM-41	1076	11.6	802	617	6.38*	-	45.4*
EM-VN-2	MCM-41	1076	15.0	673	430	3.59**	-	48.5**
EM-VN-3	MCM-41	1076	14.7	134	199	2.75**	-	47.3**
ES-VN-1	SBA-15	690	11.1	416	311	4.85*	-	45.9*
ES-VC-1	SBA-15	690	11.1	416	342	0.06**	4.15**	44.2**
EC-VN-1	NORIT-A	896	8.8	442	757	1.10**	75.0**	11.1**
EC-VC-1	NORIT-A	896	8.8	442	250	0.29*	89.5*	3.60*

a) vanadium content measured via ICP-OES (calculated from the Si/V ratio assuming the V_2O_5 formation on SiO_2).
* measured via hot gas extraction method 1-2 weeks after synthesis (stored in air atmosphere)
** measured via hot gas extraction method 50-55 weeks after synthesis (stored in air atmosphere)
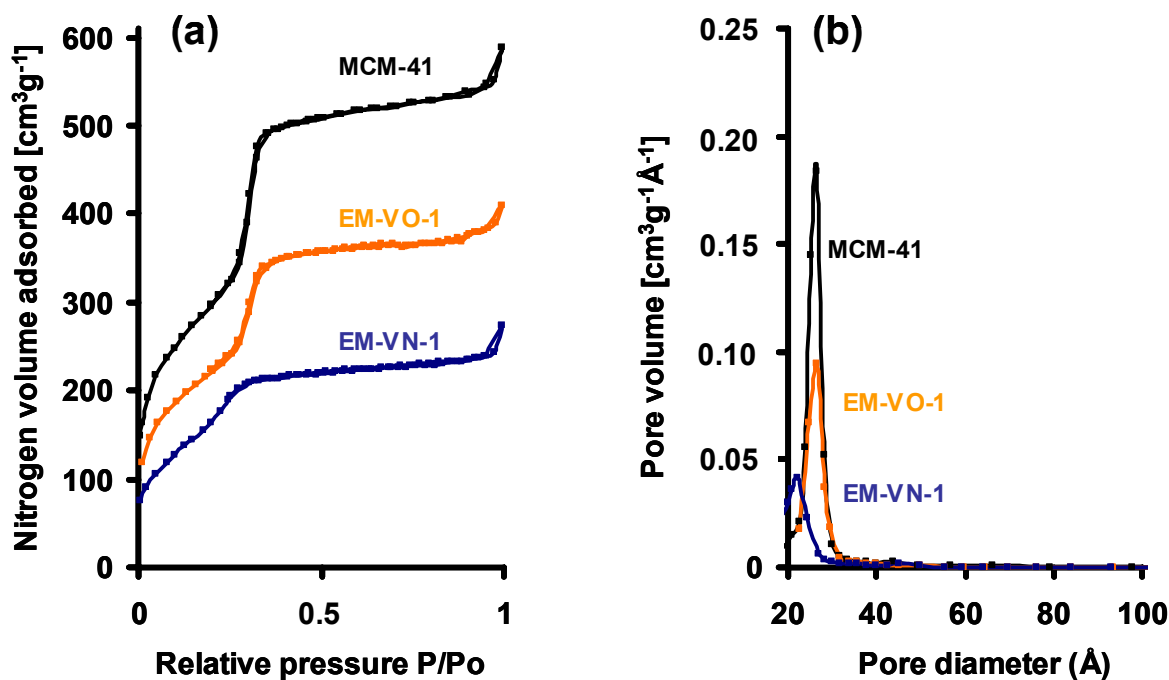
Figure 53. (a) Nitrogen physisorption isotherms of MCM-41 (black), MCM-41 supported vanadium oxide before (orange) and after (dark blue) nitridation; (b) BJH pore size distribution calculated from the adsorption branch of the nitrogen physisorption isotherms.
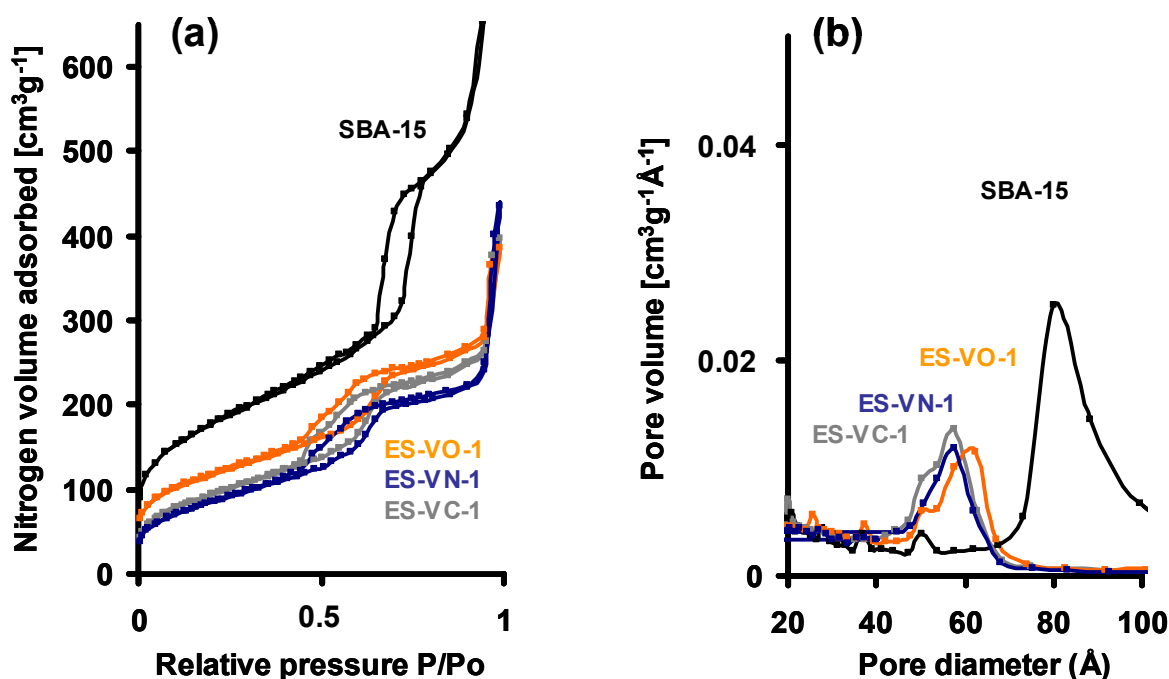
Figure 54. Nitrogen physisorption isotherms of SBA-15 (black), SBA-15 supported vanadium oxide before (orange), after nitridation (dark blue) and after carbonization (grey); (b) BJH pore size distribution calculated from the adsorption branch of the nitrogen physisorption isotherms.

The surface area was also reduced in the case of SBA-15 and NORIT-A infiltration [Table 12]. However, in the case of SBA-15 also the pore diameter was significantly decreased [Figure 54], whereas for V_2O_5/MCM-41 materials after the infiltration, the pore diameter remained constant [Figure 53]. Moreover, the pore size distribution became broader for infiltrated SBA-15 materials, suggesting significant reduction of the pore ordering. In the case of NORIT-A infiltration, no significant change in the isotherm shape was observed, only the overall volumes of gas adsorbed were lower [Figure 55].
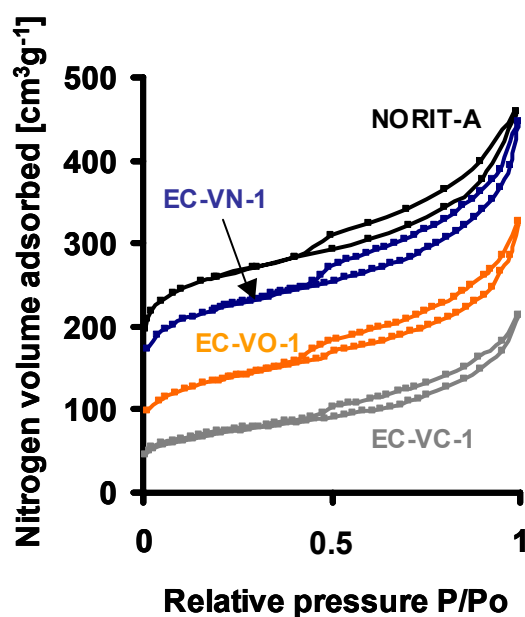
Figure 55. Nitrogen physisorption isotherms of vanadium nitride (EC-VN-1), carbide (EC-VC-1) and oxide (EC-VO-1) supported on activated carbon NORIT-A.

Low angle X-ray diffraction measurements of MCM-41 supports showed no significant structural changes [Figure 56a] as compared to vanadium-free supports. The intensity of the (100) reflection was lower and (110) and (200) reflections disappeared, but this was a typical effect when additional substance was present in the mesopores reducing the electron density contrast between pore wall and the empty pore. In contrast, infiltration of SBA-15 resulted in significant reduction of the pore ordering [Figure 56]. As compared to the original SBA-15 diffractogram, only one very broad peak could be observed.
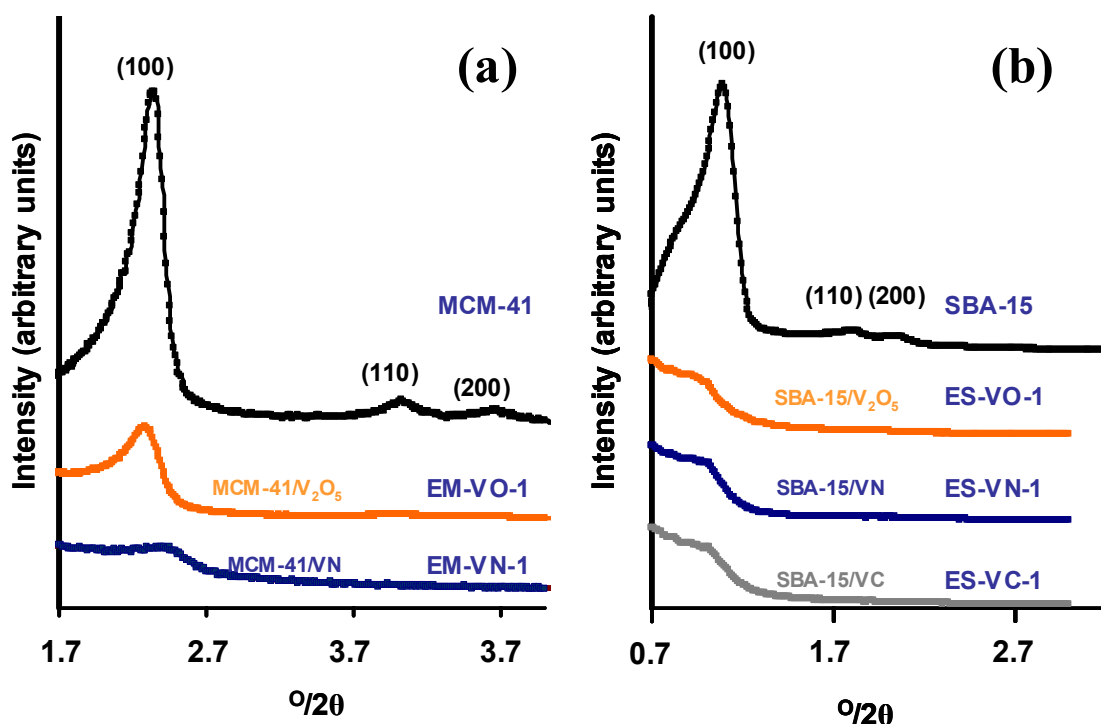
Figure 56. Low angle X-ray diffraction patterns of ordered mesoporous silica (black),V_2O_5/OMS composites (orange), V_2O_5/OMS composites after nitridation (blue) or V_2O_5/OMS composites after carbonization (grey); (a) composites prepared using MCM-41 and (b) SBA-15 silica.

Nitridation of ex-situ supported V_2O_5 materials

In the case of ex-situ prepared materials with high loading, the general trend of decreasing surface area upon nitridation was observed not for all of the samples (in contrast to the in-situ supported MCM-41 materials). The EM-VN-1, EM-VN-2 and ES-VN-1 samples reduced their surface area by 23, 36 and 25 % respectively [Table 12, Figure 53, Figure 54]. However, for the EM-VN-3 and EC-VN-1 samples the specific surface area increased significantly by 48 and 71 % [Figure 55, Table 13]. In the first case (EM-VN-3), where MCM-41 silica was used as a support, blocking of pores from the outside was suspected (large reduction of surface area after V_2O_5 infiltration). Upon nitridation, larger oxide particles blocking the pores were transformed into smaller vanadium nitride and more of the pore volume became accessible (higher surface area).

For vanadium nitride supported on activated carbon (EC-VN-1) the increase of surface area as compared to oxide was even larger (from 442 to 757 m^2g^{-1}) [Figure 55, Table 13]. To some degree, such effect could have been also assigned to vanadium oxide blocking the pores

before nitridation, but on the other hand, the oxide loading was not so high. The obtained surface area of supported vanadium nitride (757 m^2g^{-1}) reached almost the surface area of pure NORIT-A substrate (896 m^2g^{-1}) which was not in the case of EM-VN-3 sample (surface area of pure MCM-41 was 1076 m^2g^{-1}, while the VN/MCM-41 composite had only 199 m^2g^{-1}). This effect was very interesting and could be connected with the possibility of carbon removal in ammonia flow in the presence of nitrides. This was observed by Dibandjo et al. who prepared ordered mesoporous boron nitride using the CMK-3 as template (which was removed at 1000 ^oC in ammonia flow).[16]

Low angle X-ray diffraction patterns showed some degree of shrinkage and slightly disordered structure (broader (100) peak) for EM-VN-1 sample upon nitridation [Figure 56a]. In the case of SBA-15, support nitridation did not change significantly the already quite disordered structure of the oxide educt [Figure 56b]. In wide angle area of diffractograms no reflections were observed for all samples.

Nitrogen elemental analyses indicate the formation of VN since 6.4 wt.% of nitrogen was detected for EM-VN-1 sample after synthesis [Table 12] (nitridation of pure silica in same conditions yields materials with only 3.2 wt.% nitrogen: Table 12). The SBA-15 materials with slightly lower vanadium loading showed a lower nitrogen content of 4.9 wt.%. This is significantly more than for the in-situ prepared VN/MCM-41 materials with low vanadium loading. Also materials analysed after one year of storage in air, had significant amounts of incorporated nitrogen atoms. Elemental analysis of EC-VN-1 showed a reduced carbon content from 81.7 wt.% (for V_2O_5/NORIT-A composite) to 75.0 wt.% upon nitridation. This supports the concept of carbon removal at high temperatures in ammonia flow in the presence of nitrides, introduced already in several reports.[16, 25]

Carbonizationn of ex-situ supported V_2O_5 materials

In contrast to nitridation, carbonization was performed at higher temperatures (1000^oC). V_2O_5 supported on SBA-15 and on NORIT-A were tested as precursors [Table 12]. In both cases significant reduction of the specific surface area was observed (by 18% for ES-VC-1 and 43% for EC-VC-1 samples). Surprisingly, the reduction of surface area in the case of SBA-15 supported VC material (by 18%: ES-VC-1) was not as strong as in the case of SBA-15 supported VN (by 25%: ES-VN-1) [Figure 54]. However, for VC supported on NORIT-A a more severe surface area reduction (by 43%) was measured for the carbide material as compared to the nitride (which increased its surface area by 71%). This significant difference

could further confirm the hypothesis of the ammonia-carbon interactions during nitridation of V_2O_5 supported on NORIT-A.

The low angle diffraction patterns recorded for the SBA-15 supported materials showed that no significant structural changes took place in this already quite disordered material [Figure 56]. The wide angle measurements also did not confirm presence of any crystalline phase in all carbide samples.

Elemental analysis performed for the ES-VC-1 sample revealed a carbon content of 4.15 wt.% indicating VC formation. Carbonization of pure SBA-15 under similar conditions resulted in material with only 0.09 wt.% of carbon. Due to carbonization of the V_2O_5/NORIT-A material, carbon content increased from 81.7 (for V_2O_5/NORIT-A composite) to 89.5 wt% (for EC-VC-1).

4.3.3 **Propane Dehydrogenation over Supported VN**

In order to test the accessibility of vanadium nitride species, supported materials were preliminarily tested in the non-oxidative propane dehydrogenation reaction [Figure 57]. In the case of all catalysts, a deactivation with time was observed. The highest activity was observed for the EC-VN-1 (supported VN on NORIT-A) with moderate vanadium loading (8.8 wt%). On the other hand, it was measured that the activity of the vanadium-free NORIT-A support was much higher than that of the mesoporous silica [Figure 57: NORIT-A and SBA-15]. Among the materials supported on ordered mesoporous silica, the highest conversions were observed for the IVN-1 sample prepared via the in-situ procedure and ES-VN-1 sample prepared via the ex-situ method. Although having similar activity, both samples had substantially different vanadium content. The IVN-1 calatyst had only 5 wt.% of vanadium, while ES-VN-1 twice as much (11.1 wt.%). This demonstrates that the in-situ method allows to prepare highly dispersed vanadium species as compared to the ex-situ method.

It was further confirmed by the EM-VN-1 sample which had similar vanadium content as ES-VN-1 sample and showed even lower activity. When vanadium content was increased further to 14.7 (EM-VN-3) and 15.0 wt% (EM-VN-2), the activity of the catalyst further decreased and became equal to the in-situ prepared materials with only 2.5 wt.% vanadium.
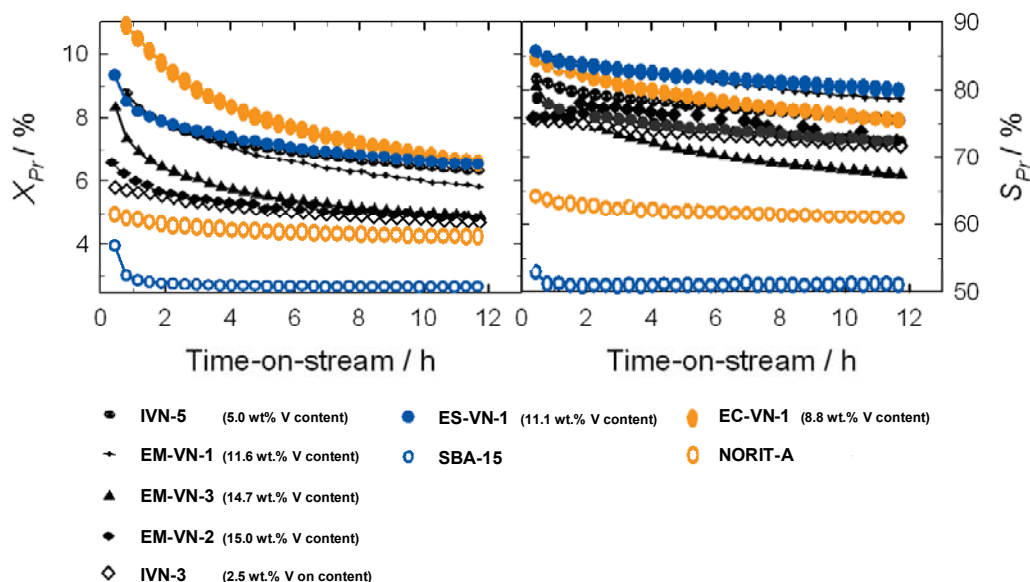
Figure 57. Conversion and selectivity (towards propene) of propane over supported vanadium nitride catalysts (T = 525 °C, WHSV = 2 h^{-1}). In brackets, measured vanadium loading for supported oxide before nitridation is given [Table 11, Table 13]. Black marks and lines were used for MCM supported materials, blue for SBA-15 supports and orange for activated carbon NORIT-A support.

4.3.4   Conclusions

In this paragraph it was shown how the in-situ vanadium incorporation method was used to prepare highly dispersed vanadium nitride and carbide species inside the mesoporous silica materials. Significant structural differences were observed for materials prepared via "direct solubilization" and "toluene delivery" routes. The first one resulted in vanadium incorporation in the bulk pore wall, while in the second, probably pore wall coating and particles were obtained, which had a significant influence on the nitridation process. Incorporation of vanadium species directly into the pore wall via direct solubilization of vanadium precursor resulted in well ordered oxide materials, although the material was more sensitive to the ammonolysis process as compared to pure MCM-41 and material prepared via toluene delivery method. In turn, the ex-situ method allowed to prepare materials with higher vanadium loadings and on different supports (like activated carbons). The catalytic activity of the ex-situ prepared materials was similar to that of in-situ prepared materials, although the latter ones had significantly lower vanadium content. On the other hand, if the vanadium content was increased to around 15 wt.% for ex-situ materials, catalytic activity decreased.

The next chapter (Chapter 4.4) will present an alternative method to prepare bulk VN (support-free) nanocrystalline vanadium nitride material with high surface areas and high catalytic activity in propane dehydrogenation.

4.4 Amine Intercalated Oxide Foams for the Preparation of High Surface Area Transition Metal Nitride Catalysts

A common method for preparation of vanadium nitride with a surface area up to 90 m^2g^{-1} is nitridation of vanadium oxide in an ammonia flow.[26] However, commercially available V_2O_5 powders consist of particles several micrometers in size with low specific surface area (S_g = 4-5 m^2g^{-1}) and little control was achieved over particle sizes of the final powder. A specific surface area of 90 m^2g^{-1} and particle sizes of 12 to 20 nm were obtained by employing low heating rates (100-300 Kh^{-1}) and extremely high ammonia flows[26, 151] (300 h^{-1}-1300 h^{-1} molar space velocity). The use of vanadium oxide aerogels as precursors allowed the enhancement of the surface area of VN (120 m^2g^{-1}) but even higher space velocities (1870 h^{-1}) had to be applied.[157, 198] In the following, a new method to prepare nanocrystalline (6-8 nm) vanadium nitride with a high specific surface area (S_g = 80-190 m^2g^{-1}) using temperature programmed reduction of a high volume vanadium oxide foam is presented.[25] Oxide foams are new precursors for preparation of nitrides with specific surface areas and particle sizes unattained so far. Furthermore, this method could be extended to other ternary transition metal nitrides as well.
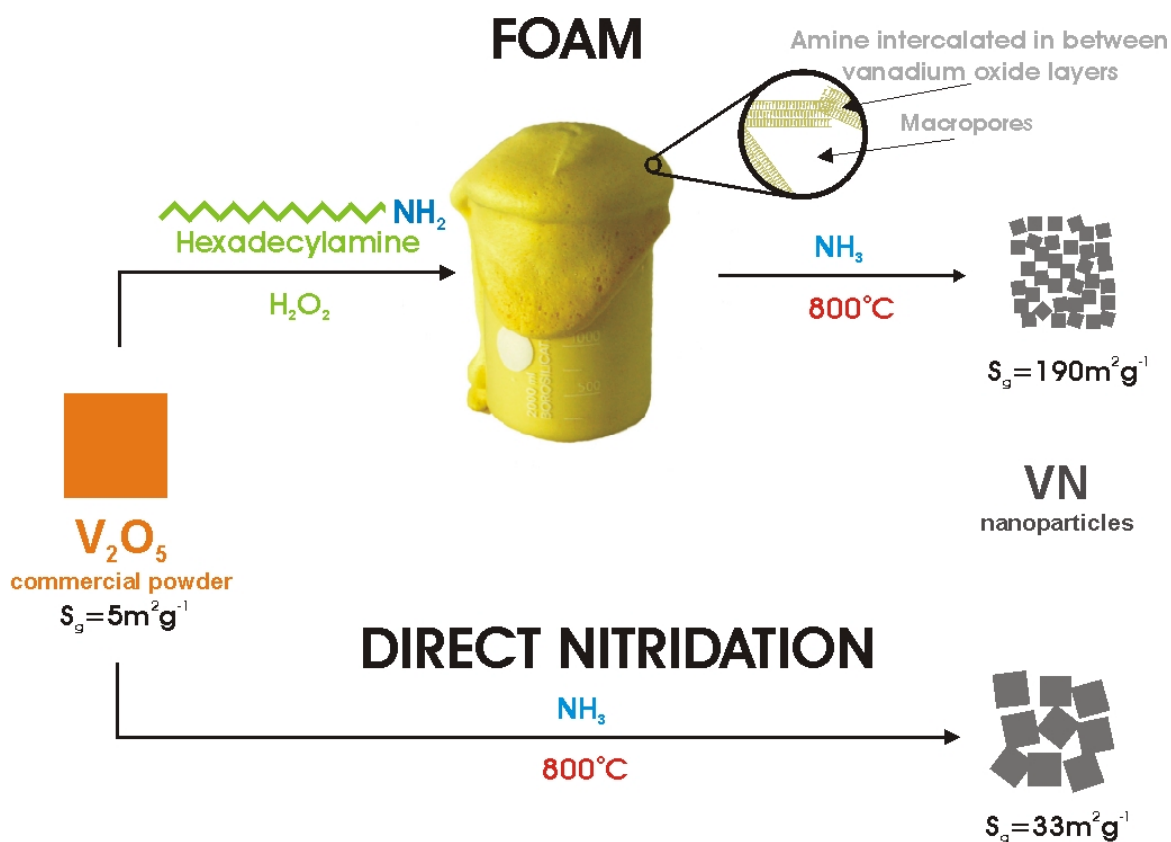
Scheme 9. Preparation of high surface area vanadium nitride via foam and direct nitridation procedure

Foam-derived high surface area vanadium nitrides were tested in the non-oxidative dehydrogenation of propane. They show a considerably higher activity as compared to vanadium nitride synthesized directly from V_2O_5. Conversion of *n*-butane on vanadium nitrides and carbides as well as conversion of propane over supported molybdenum carbide have been reported previously.[151, 199] The catalytic potential of transition metal nitrides for non-oxidative dehydrogenation of propane is still largely unexplored.

4.4.1　High Surface Area Vanadium Nitride

Recently, a novel method for generation of oxide foams was developed by Livage.[200, 201] This method produced a macroporous solid, a composite of V_2O_5 and hexadecylamine with the latter intercalated in between the oxide layers. The foaming process allowed the preparation of a high-volume precursor (1 g of V_2O_5 produced up to 2.5 L of foam). In the following, it is shown how this V_2O_5 foam is transformed in a reaction with ammonia into nano-crystalline vanadium nitride. Not only is the macroporosity of the foam beneficial, but also amine separating oxide layers in the composite and thus sintering or aggregation of particles during nitridation process is avoided.

The space velocity of ammonia used in nitridation of the foam strongly affected the amine removal. Low space velocities (33 h^{-1}) favored the formation of pyrolitic carbon. Three foam-derived vanadium nitride samples [Table 13] were prepared using different loadings of foam in the reactor (1.5g, 2.5g and 7.5 g), while the ammonia flow was kept constant. For comparison, one vanadium nitride sample (VN-S) was prepared via direct nitridation of a commercially available V_2O_5 ($S_g = 5$ m^{2}g^{-1}).

Table 14. Preparation conditions and properties of VN materials (VN-1, VN-2, VN-3 prepared from V_2O_5 foam using different ammonia space velocities, VN-S prepared from V_2O_5 powder).

Sample code	Ammonia Space velocity [a] h^{-1}	Specific Surface area m^{2}g^{-1}	Average crystallite size [b] nm	Nitrogen content[c] wt.-%	Carbon content[d] wt.-%
VN-1	168	80	8.1	17.8	2.8
VN-2	101	146	7.2	11.5	10.2
VN-3	33	190	6.3	9.4	17.3
VN-S	118	33	23.0	16.8	-

a) mol(NH$_3$)/mol(V$_2$O$_5$), b) Average crystallite diameter estimated from XRD using the Scherrer equation.[202]
c) Measured by hot gas extraction d) measured by combustion method

A high space velocity of ammonia (for sample VN-1: 168 h^{-1}) allowed almost complete removal of amine and only 2.8 wt.-% of carbon was observed as an impurity. Decreasing the space velocity to 101 and 33 h^{-1} (VN-2 and VN-3) caused an increase of the carbon content to 10.2 and 17.3 wt.-%, respectively. The increasing surface area (from 80 to 190 m^{2}g^{-1}) with increasing carbon content (from 2.8 to 17.3 wt.-%) suggested a significant contribution of pyrolytic carbon to the specific surface area [Table 13]. The smallest (6.3 nm in diameter) vanadium nitride crystallites were detected in the sample with the highest carbon content (VN-3) [Table 13, Figure 58], while for the samples with lower carbon residue (2.8 wt.-% and 10.2 wt.-%), the crystallite diameter was estimated to be slightly larger (7.2 nm and 8.1 nm respectively). The measured surface area of the VN-2 sample (146m^{2}g^{-1}) corresponded well to the one calculated from the crystallite size (138 m^{2}g^{-1}, ρ=6.04 gcm^{-3} [144]). For VN-1 the surface area estimated from the crystallite size was higher (123 m^{2}g^{-1}) as compared to the value measured by nitrogen physisorption (80 m^{2}g^{-1}) indicating agglomeration. For VN-3 the measured surface area (190 m^{2}g^{-1}) exceeded the estimated value (158 m^{2}g^{-1}) indicating contributions from carbon residues formed during pyrolysis. Thus, the role of amine was to prevent nitride particles from sintering and agglomerating. This mechanism was effective during the early stages of V$_2$O$_5$ reduction, since V$_2$O$_5$ due to its low melting point (690 ^{o}C) is very susceptible to densification. All of the foam-derived samples had substantially higher surface areas and consisted of much smaller (6 to 8 nm in diameter) particles compared to the sample synthesized via direct nitridation of V$_2$O$_5$ powder (VN-S, 23 nm), although the synthesis conditions were similar.
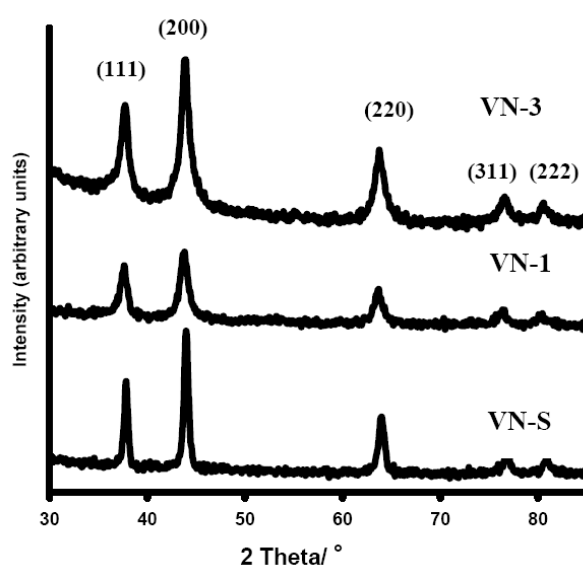
Figure 58. X-ray diffraction patterns of vanadium nitride-based samples derived from foam (VN-1, VN-3) and via the standard procedure (VN-S)

Nitrogen analyses showed a variation of the nitrogen content with the reaction conditions [Table 13]. The calculated value for pure $VN_{1.0}$ is 21.4 wt.-%. Since our samples contain significant amounts of residual carbon (2.8 to 17.3 wt.-%), the relative nitrogen content is lower (17.8 to 9.4 wt.-%). Additionally, nitrides tend to form oxidic passivation layers, which should also be taken into account. Although this effect was minimized by passivation with oxygen (1vol.-% O_2 in N_2),[26] due to the very small crystallite size (6-8 nm) and large specific surface area (80-190 m^2g^{-1}), a layer of oxide could have significantly contributed to the overall composition. For VN-3, the oxides VO_2 (29 %) and V_2O_5 (31%) were clearly identified in $V2p_{3/2}$ X-ray photoelectron spectra [Figure 59],[203] whereas the VN signal (40 %) was observed at 513.6 eV.[204] For VN-1, the nitrogen content was close to the theoretical value (17.8 wt.-%). This sample had both the lowest carbon content (2.8 wt.-%) and the largest particles (8.3 nm). The other VN-2 and VN-3 samples had a lower nitrogen content (11.5 and 9.4 wt.-%), since the amount of residual carbon was higher (10.2 and 17.3 wt.-%), and the particle size was smaller (7.2 and 6.1 nm) enhancing the amount of surface oxide.
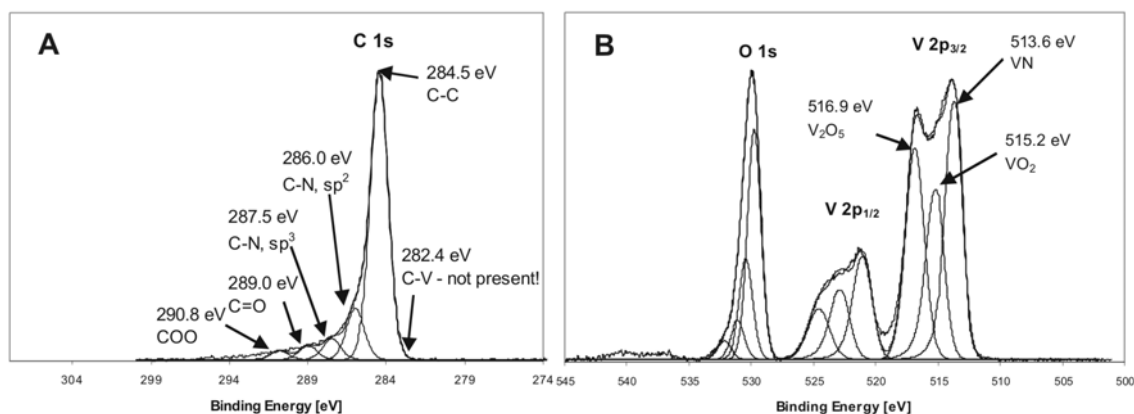
Figure 59. (A) C1s XPS spectra of VN-3 after passivation with 1% oxygen/nitrogen mixture (B) $V 2p_{3/2}$ spectra of the same VN-3 sample

A more in-depth analysis of the X-ray diffraction patterns [Figure 58] indicates that in the case of VN-S, the lattice parameter was smaller (4.113 Å) than in the case of foam-derived samples (4.125 Å for VN-3 and 4.134 Å for VN-1). In pure nitride, the lattice parameter was 4.138 Å,[144] and a slight decrease to 4.125 and 4.13 Å indicated substitution of oxygen into the lattice. This was consistent with the elemental analyses of VN-1, with a slightly lower nitrogen content than expected (17.8 wt.-% instead of 21.4 wt.-%). In the case of finely dispersed vanadium oxide foam, nitridation proceeded faster as compared to pure V_2O_5 powder, but in the nitride oxygen was not only present in a surface oxide layer, but also substituted in the bulk material. Substitution of nitrogen by carbon in foam-derived VN was

not observed. For carbon-substituted materials an increased lattice parameter is expected ($a(VC_{0.88})$ = 4.164 Å, $a(VC_{0.96})$ = 4.182 Å).[26, 144] The absence of V-C bonds was further confirmed by XPS showing no signals at 282.4 eV in the C1s spectra.[205] According to XPS studies, carbon was present as elemental carbon (75% C-C among carbon species for VN-3) but signals at 287.5 and 286.0 eV indicated the presence of C-N bonds.[206]

Kapoor and Oyama[26] used V_2O_5 as a precursor with a specific surface area of 19 m^2g^{-1} and extremely high space velocities of ammonia (1300 h^{-1}). The vanadium nitride received had a particle size of 14 nm and a surface area of 90 m^2g^{-1}, while in the method reported here, space velocities were considerably lower (168 h^{-1} for the sample VN-1 and 33 h^{-1} for the sample VN-3). Thus, the foam route yields materials with small particle sizes (6-8nm) that can be produced from low surface area substrates (S_g < 5 m^2g^{-1}), using orders of magnitude ammonia flows (33 to 168 h^{-1}) than reported in the literature.[26, 151, 157]

A transmission electron micrograph of VN-1 [Figure 60] showed powders composed of agglomerates of crystalline particles, with sizes in between 5 and 10nm.
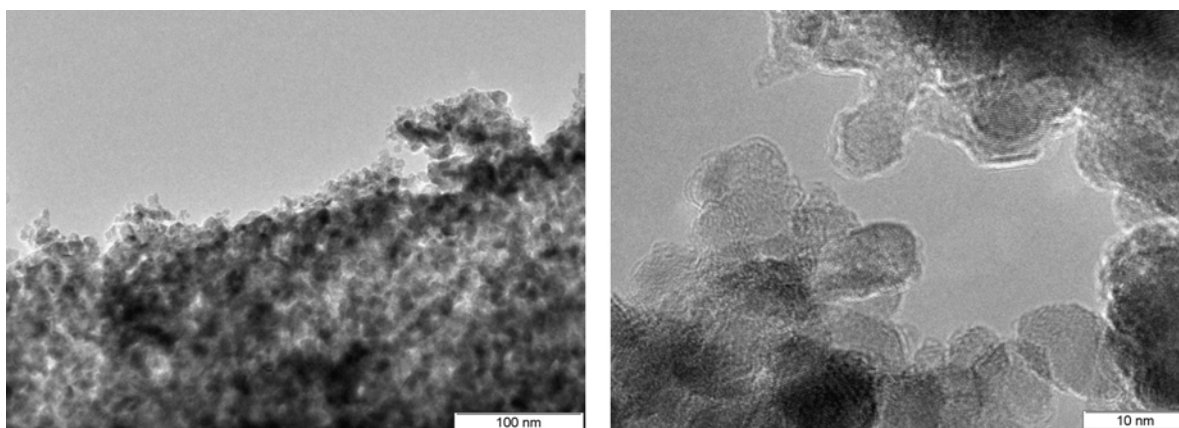
Figure 60. Transmission electron micrographs of VN-1

4.4.2 Propane Dehydrogenation over High Surface Area Vanadium Nitride Catalysts

Vanadium nitride materials prepared from vanadium oxide foams were tested in the non-oxidative dehydrogenation of propane [Figure 61]. Compared to the sample synthesized via direct nitridation of dense V_2O_5 powder, the foam-derived catalysts showed considerably enhanced activity. The propane conversion increased with the specific surface area of the materials. All catalyst samples were prone to a rapid deactivation during the first 2hours of experiments. However, after 2hour time-on-stream, the gravimetric reaction rate over the

sample with the highest specific surface area (VN-3, 76 µmol g^{-1} s^{-1}) was 2.5 times higher than that observed on the sample with the lowest specific surface area (VN-S, 31 µmol g^{-1} s^{-1}).
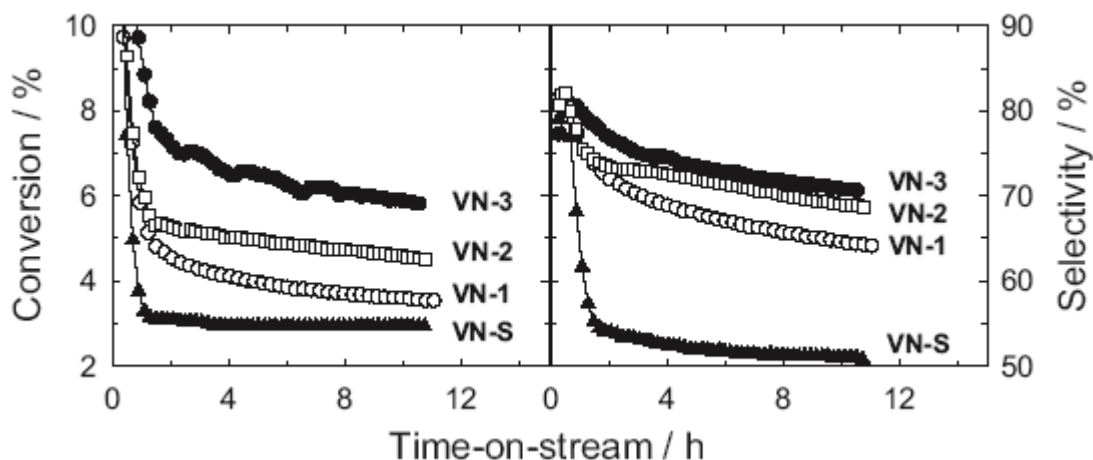
Figure 61. Conversion and selectivity (towards propene) of propane over vanadium nitride catalysts (T = 525 °C, WHSV = 2 h^{-1}).

The higher gravimetric reaction rates over the foam-derived samples were mainly due to a higher rate of propene formation over these catalysts. The relative increase of propene yield passing from the catalyst with S_g = 33 m^{2}g^{-1} to that with 190 m^{2}g^{-1} was 3.3 %, whereas the combined yields of methane, ethane and ethene increased by 0.5 % only. The latter products resulted from propane cracking and hydrogenolysis as side reactions of propane dehydrogenation. As a consequence of higher dehydrogenation rate, selectivity of high surface area nitrides for propene was higher than that of the conventionally prepared sample VN-S (> 70 % for VN-2 and VN-3 vs. < 55 % for VN-S compared after the initial deactivation period of 2h time-on-stream). The areal rate was similar over VN-1, VN-2 and VN-3 (0.54 µmol m^{-2} s^{-1}), but lower than that observed over VN-S (1.08 µmol m^{-2} s^{-1}). This indicated that, with respect to VN-S, the foam-derived samples exhibited a lower density of active sites or sites with a lower activity. These sites could have been more selective for the dehydrogenation of propane. Moreover, although the areal rate for the foam-derived samples with different specific surface areas was similar, the propene selectivities were slightly different. This indicated the presence of different types of active sites on the catalyst surface. This may be related to a change of the surface composition with increasing specific surface area or to a different local coordination of active sites on the surface of smaller and larger crystallites (e.g., defect positions), respectively. However, the nature of these sites is still unknown. A possible role of the higher residual carbon content in the materials with higher specific surface area could also not be excluded. In conclusion, although the results depicted in Figure 61 showed that higher conversions were achieved on materials with larger specific surface areas, the different selectivities observed

over VN-1, VN-2 and VN-3 implied that the surface properties and, thus, the active sites might have been affected as well. Similar effects of the specific surface area on the areal rate were also observed by Y. Zhang et al.[207] during the hydrogenation of cyclohexene over Mo_2N catalysts. These authors correlated the higher specific activities of the samples with lower specific surface areas with a higher ratio of (111)- relative to (200)-crystal planes as determined from the corresponding intensities of XRD reflections.

For a comparison, propane conversion over the foam-derived vanadium nitride with the highest specific surface area (VN-3) was also carried out under the conditions applied by Solymosi *et al.* in an investigation of a Mo_2C catalyst supported on Cab-O-Sil (high surface area silica).[199] Also, the Mo_2C catalyst was reported to deactivate within the first 2 h of the experiment. The catalytic activity of both VN-3 and the supported Mo_2C was in a similar range. Upon closer analysis of the propane conversion, the vanadium nitride catalyst was less active than the Mo_2C supported on Cab-O-Sil in the initial stage of the experiment (initial areal rate: 0.27 vs. 0.47 $\mu mol \, m^{-2} \, s^{-1}$ as calculated based on the specific surface area of the Cab-O-Sil support). However, after 3h time-on-stream, the areal rate was equal on both catalysts (0.22 $\mu mol \, m^{-2} \, s^{-1}$) and after 12h time-on-stream slightly higher over VN-3 than over the supported Mo_2C catalyst (0.21 $\mu mol \, m^{-2} \, s^{-1}$ vs. 0.15 $\mu mol \, m^{-2} \, s^{-1}$). Moreover, the selectivity for propane dehydrogenation was significantly higher ($S_{Pr} > 63\%$) over the vanadium nitride catalyst throughout the whole catalytic experiment. This was due to a higher activity of the Mo_2C catalyst for propane cracking and aromatization which was particularly pronounced at the early stages of the catalytic conversion ($S_{Pr} < 49\%$, $S_{Methane+Ethane+Ethene} > 36\%$, $Y_{Aromatics} > 15\%$, $Y_{Methane+Ethane} > 30\%$ in the first 2h time-on-stream).

At similar experimental conditions, the initial reaction rate observed over the most active vanadium nitride catalyst (VN-3) was lower than that observed over a silica supported Pt-Sn-catalyst (gravimetric rate: 150 vs. 450 $\mu mol \, g^{-1} \, s^{-1}$, areal rate 0.8 vs. 1.03 $\mu mol \, m^{-2} \, s^{-1}$ as calculated based on the specific surface area of the silica support). Nevertheless, the foam-derived VN catalysts reported here appeared to be more efficient catalysts than all the transition metal nitrides and carbides for the non-oxidative dehydrogenation of propane reported up to now in the literature. Although the reasons for the rapid deactivation of these catalysts are still unknown, the higher activity obtained through the new foam-derived materials showed that there is still significant room for improvement of their stability and conversion levels. As these materials are less costly than noble metals, they might offer an interesting alternative as catalysts in the non-oxidative dehydrogenation of lower alkanes.

4.4.3   High Surface Area Ternary V-Mo Nitrides via Foam Procedure

In the previous chapter, the preparation of high surface area vanadium nitride via foam procedure was demonstrated. In principle, such method could be extended to any other nitride and carbide materials if the corresponding oxides form foams in the presence of amines. Here, it is attempted to prepare the foam of MoO_3 according to the same procedure as for the V_2O_5 foam (Molybdenym oxide in presence of hexadecylamine and H_2O_2). However, due to low decomposition rate of H_2O_2 on pure MoO_3, no high-volume product was obtained. Nevetherless, it was discovered that ternary foams can be prepared in the V-Mo system. In principle, different approaches were used for the preparation of such foams [Scheme 10].
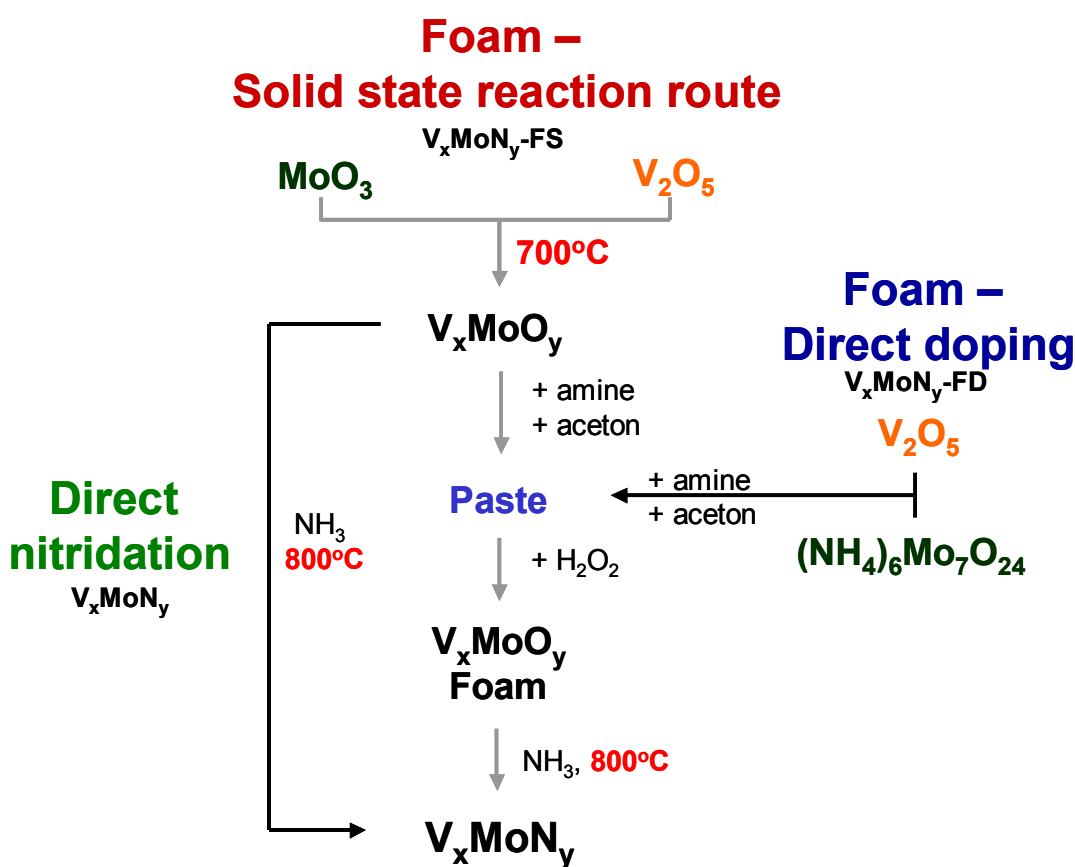
Scheme 10. Preparation procedures for foam-derived ternary nitrides.

In the case of the "solid state reaction route" [Scheme 10 – Solid state reaction route] first a mixed oxide of V_xMoO_y was prepared with different V/Mo ratios by heating appropriate amounts of V_2O_5 and MoO_3 precursors up to 700 °C and cooling down to room temperature. According to X-ray diffraction patterns, the resulting ternary oxides were composed mainly of V_2MoO_8 (JCPDS: 20-1377) with some impurities of unidentified vanadia rich phase [Figure

62]. The relative amount of the unknown phase was increasing with the increasing vanadium content. Although the unkown reflections were not clearly identified in the crystallographic database, the phase diagram of the V_2O_5-MoO_3 system suggested that beside V_2MoO_8, Mo doped V_2O_5 phase (($V_{1-y}Mo_y)_2O_5$) should be present in the vanadium rich samples.[208]
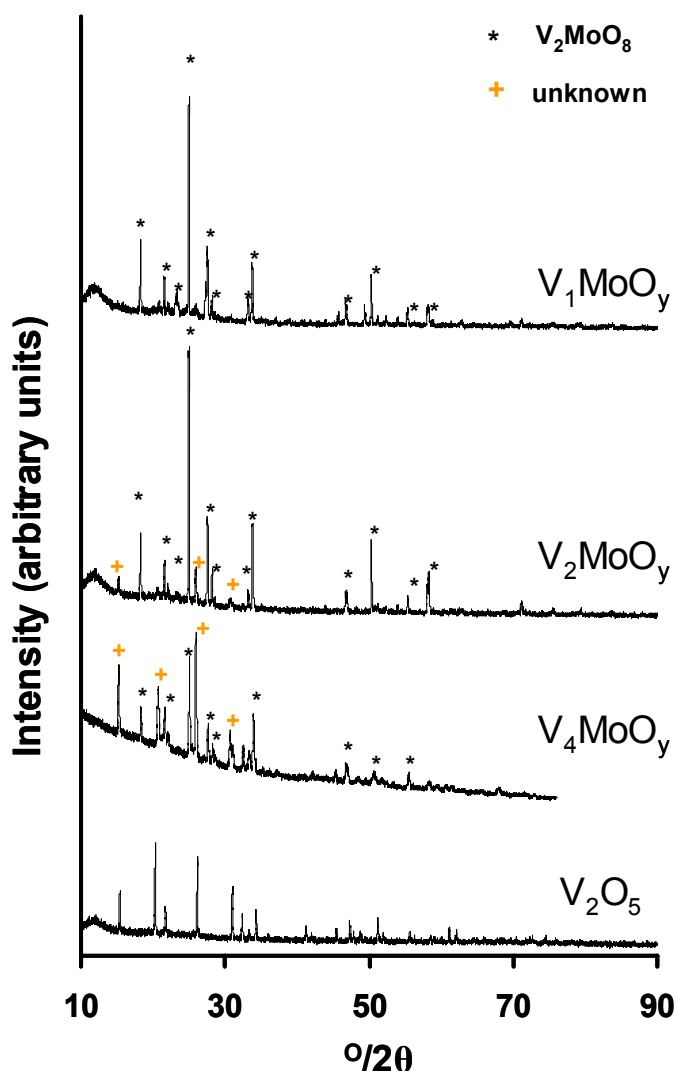
Figure 62. X-ray diffractograms of selected ternary V_xMoO_y materials and V_2O_5 precursor.

After synthesis of the ternary oxides, the resulting product was mixed with amine and acetone to form a paste. The prepared paste was then treated with H_2O_2 to start the foaming process. The as prepared foam was left for drying and placed in the reactor in ammonia flow at 800 ^{o}C for nitridation. The samples prepared via this procedure are marked as V_xMoN_y-FS. A "direct doping" [Scheme 10 – direct doping] procedure was also employed to prepare foam derived ternary nitrides. In the latter, instead of ternary oxides, a mixture of V_2O_5 and a molybdenum precursor dissolving in H_2O_2 was used (ammonium heptamolybdate tetrahydrate:

($NH_4)_6Mo_7 \cdot 4H_2O$). High surface area ternary V-Mo-N nitrides were also proposed by Oyama as interesting materials as heterogeneous catalysts due to their high surface reactivity.

The preparation of V-Mo foams was successful for materials with V/Mo ratio higher than one. If lower amounts of vanadium were used, the foaming process was slow and the foam tended to collapse before reaching high volumes. Preparation of foams via the "solid state reaction route" resulted in more homogeneous and higher-volume materials, as compared to the foams prepared via "direct doping". Also the nitridation experiments of such foams indicated that in the case of foam precursors prepared via the "solid state reaction route" the received nitride materials had higher surface areas than those prepared from directly doped foams. In the case of V_4MoN_y-FS sample, a surface area of 198 m^2g^{-1} was measured, while for the same composition prepared via the direct doping procedure, a lower surface area of 151 m^2g^{-1} was observed (V_2MoN_y-FD) [Table 14]. The same trend was observed for materials with lower V/Mo ratio. For example, V_2MoN_y-FS prepared via solid state reaction foam route had a surface area of 83 m^2g^{-1}, while for the sample prepared via direct doping of the foam, only 37 m^2g^{-1} was measured (V_2MoN_y-FD) [Table 14]. Therefore, other foam-derived samples with different stoichiometry were prepared only via the "solid state reaction route".

Table 15. Surface areas and preparation procedures of foam-derived ternary nitrides compared to materials prepared by direct nitridation

Material	Foam preparation	Surface area[b] (V_xMoN_y-FS V_xMoN_y-FD)	Surface area: non-foamed material[c] (V_xMoN_y)	Crystallite size[d] (V_xMoN_y-FS V_xMoN_y-FD)	Crystallite size: non-foamed material[e] (V_xMoN_y)
VN	-	190	33	6.1	23.0
V_4MoN_y	SSRR[a] (FS)	198	55	6.3	16.3
V_3MoN_y	SSRR[a] (FS)	127	66	6.8	14.7
V_2MoN_y	SSRR[a] (FS)	83	90	8.0	13.3
V_1MoN_y	SSRR[a] (FS)	45	100	10.2	5.6
Mo_2N	-	-	120	-	6
V_4MoN_y	Direct doping (FD)	151	55	6.9	16.3
V_2MoN_y	Direct doping (FD)	37	90	9.1	13.3

a) SSRR – solid state reaction route of foam preparation, b) BET specific surface area of samples prepared from foams [Scheme 10 – foam – direct doping, solid state reaction route] c) BET specific surface area of samples prepared via direct ternary oxide nitridation procedure [Scheme 10 – direct nitridation] d) Calculated according to the Scherrer equation e) Calculated according to the Scherrer equation for samples prepared via direct alloy nitridation procedure

In order to investigate if the presence of amine and foam formation had a crucial influence on the preparation of the high surface area material, additional samples were prepared via direct nitridation of non-foamed ternary oxides [Scheme 7 – Direct nitridation].

The surface area of pure VN and Mo_2N prepared via direct nitridation of ternary oxides is also given for comparison [Table 14]. The highest surface areas were observed for foam derived materials with high vanadium content (VN: 190m^2g^{-1} and V_4MoN_y-FS: 198m^2g^{-1}). If the amount of molybdenum was increased, the specific surface area decreased down to 45m^2g^{-1} for the sample with the lowest vanadium content (V_1MoN_y-FS). The inverse relation was observed for the materials prepared via direct nitridation procedure [Scheme 10 – Direct nitridation]. In it, the surface area was increasing from the 33m^2g^{-1} (pure VN sample) to 100m^2g^{-1}, measured for V_1MoN_y-FS sample with low vanadium content. The graphical form of specific surface area values with changing stoichiometry and preparation procedure is presented in Figure 63.
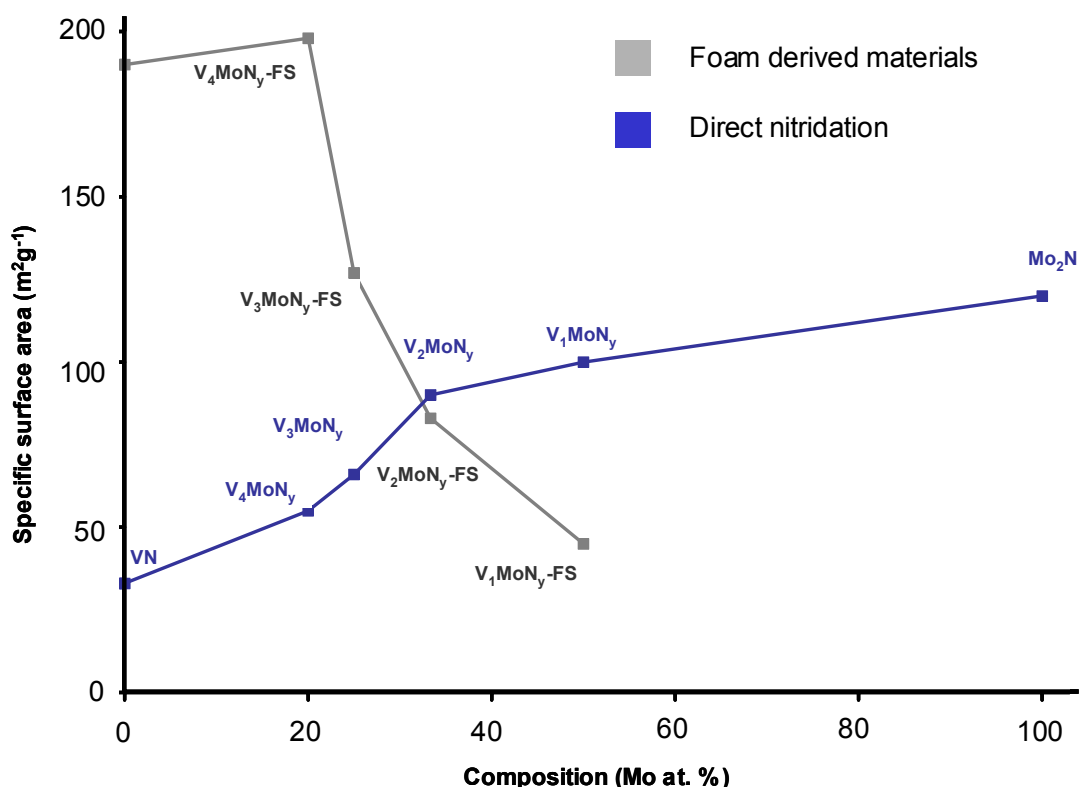
Figure 63. Specific surface areas of ternary and binary nitrides prepared via direct nitridation (blue line) and nitridation of foam derived via solid state reaction route (grey line)

Both γ-Mo_2N and VN crystallize in the face centered cubic unit cell (fcc) with different unit cell size. In the case of γ-Mo_2N the lattice constant is 4.126 Å while for the VN it is 4.138 Å. Ternary V-Mo nitrides were reported by Oyama to have the same fcc unit cell symmetry. The V atoms are substituted by Mo in the VN crystal and Mo atoms by V in γ-Mo_2N so that VN-Mo_2N solid solutions are formed. The X-ray diffraction patterns confirmed the face centered cubic structure of ternary nitrides with peaks located in between the corresponding peaks of γ-Mo_2N and VN [Figure 64].
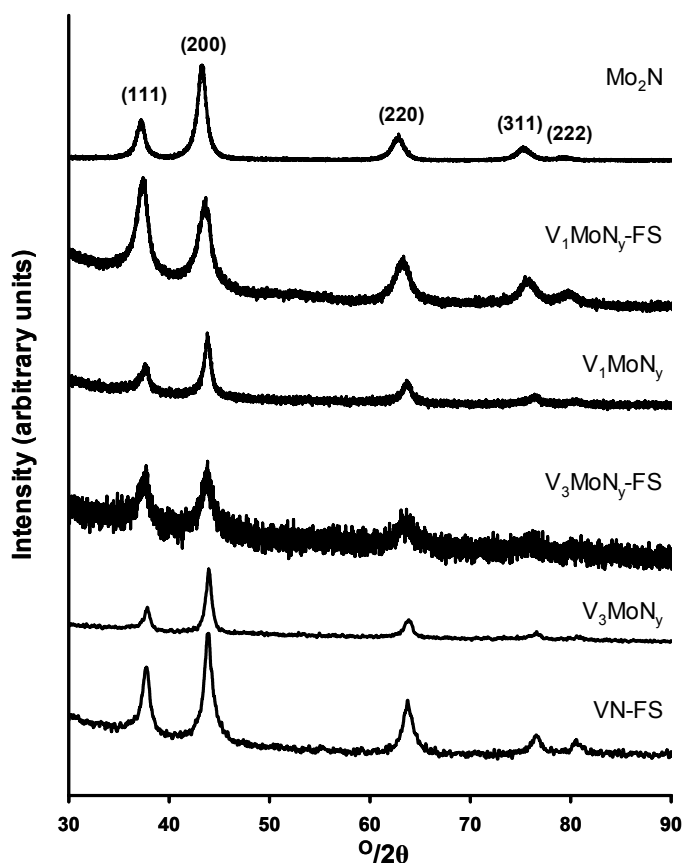
Figure 64. X-ray diffractograms of selected ternary nitrides (foam derived – V_xMoN_y-FS and prepared via direct alloy nitridation – V_xMoN_y)

Interestingly, for materials prepared via the foam procedure, different (111) and (200) peak intensity ratios were observed. In the case of samples prepared via direct nitridation, the (111) reflection had much lower intensity than (200) (Figure 64 – V_1MoN_y and V_3MoN_y), while for the foam derived samples, the (111) intensity was significantly increased (Figure 64 - V_1MoN_y-FS and V_3MoN_y-FS). The lattice constant increased with increasing molybdenum content. However, for foam derived ternary nitrides, the lattice constant was always higher as compared to samples prepared via direct alloy nitridation, indicating incorporation of carbon into the crystal lattice. Although, carbide formation was excluded for foam derived vanadium nitride sample, (based on the XPS measurements and due to the fact that temperatures higher than 1000 °C were typically used to prepare vanadium carbide), in the case of ternary nitrides additional measurements are to be made since molybdenum is known to form carbides easily even at temperatures lower than 800 °C.[148] Another reason could be that highly dispersed foams were nitrided faster than the bulk micro-meter sized crystals and less oxygen is present in the lattice.
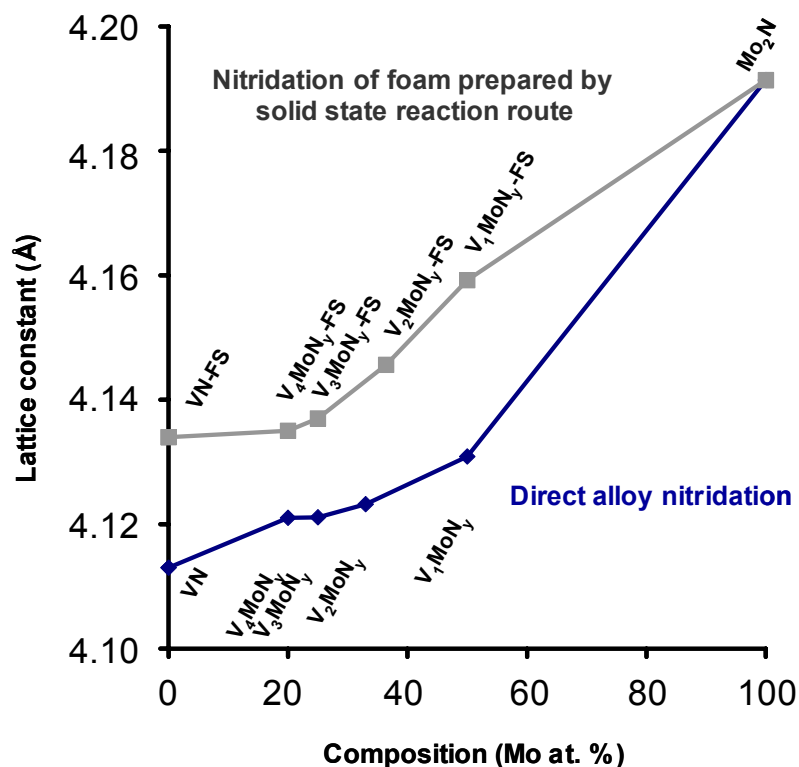
Figure 65. Lattice constants of ternary nitrides as a function of chemical composition.

The VMo_xN_y materials prepared from foams and via the direct nitridation were also preliminary tested in the propane dehydrogenation reaction. However, they had lower conversions and selectivities than the high surface area VN with $190 m^2 g^{-1}$ prepared from foam. Although the V_2O_5 foam synthesis procedure could not be directly applied for the preparation of MoO_3 foams (at least without major modification), the intercalation of amine into the molybdic acid was recently reported.[209] Also preparation of TiO_2 foam in presence of amine is described with the similar procedure to the V_2O_5 foam preparation. Such foams can be interesting for the preparation of other nitride nanomaterials.[210]

4.4.4   Conclusions

In summary, a novel method for preparation of vanadium nitride and doped vanadium nitride nanoparticles (6-8 and 6-10 nm) was presented. A pre-structured foam precursor containing highly dispersed, amine intercalated V_2O_5 was used as a precursor. The residual carbon content and particle size was controlled by changing the space velocity of ammonia. The foam route should be in principle applicable to many other systems such as carbides and oxides, not only of vanadium but also of other transition metals. Preliminary experiments showed that also high surface area ternary nitrides could be prepared via this method. In comparison to vanadium nitride obtained through the conventional V_2O_5 nitridation route, these high surface area materials exhibited a significantly improved catalytic activity in the non-oxidative dehydrogenation of propane. In contrast to supported vanadium nitrides, (Chapter 4.3) preparation of foam nitrides was simpler and the materials obtained were crystalline according to X-ray diffraction patterns. Due to their mechanical and tribological properties the bulk not supported nanocrystalline nitrides may be an interesting material for nanocomposites with increased hardness or plasticity.

5   Summary

In the present work new methods were developed for preparation of novel nanosized and nanostructured ceramic materials [Scheme 11].

Ordered mesoporous silica SBA-15 was found to be useful as a hard template for the nanocasting of silicon carbide and allowed the preparation of high temperature stable mesoporous silicon carbide ceramics [Scheme 11 – NANOCASTING]. Chemical vapor infiltration of SBA-15 with dimethyldichlorosilane at elevated temperatures yields SiC/SBA-15 nanocomposites. The subsequent HF treatment of those composites resulted in silica removal and preparation of mesoporous silicon carbide with surface areas between 410 and 830 m^2g^{-1} and high mesopore volume (up to 0.9 cm^3g^{-1}). The pore size (between 3 and 7nm in diameter) and surface area of mesoporous silicon carbide were controlled by adjusting the infiltration conditions (time, atmosphere). The mesoporous silicon carbide prepared via this method showed high structural thermal stability at 1300 ^{o}C, exceeding that of the SBA-15 template. However, the ordering on the mesoscopic scale was low.
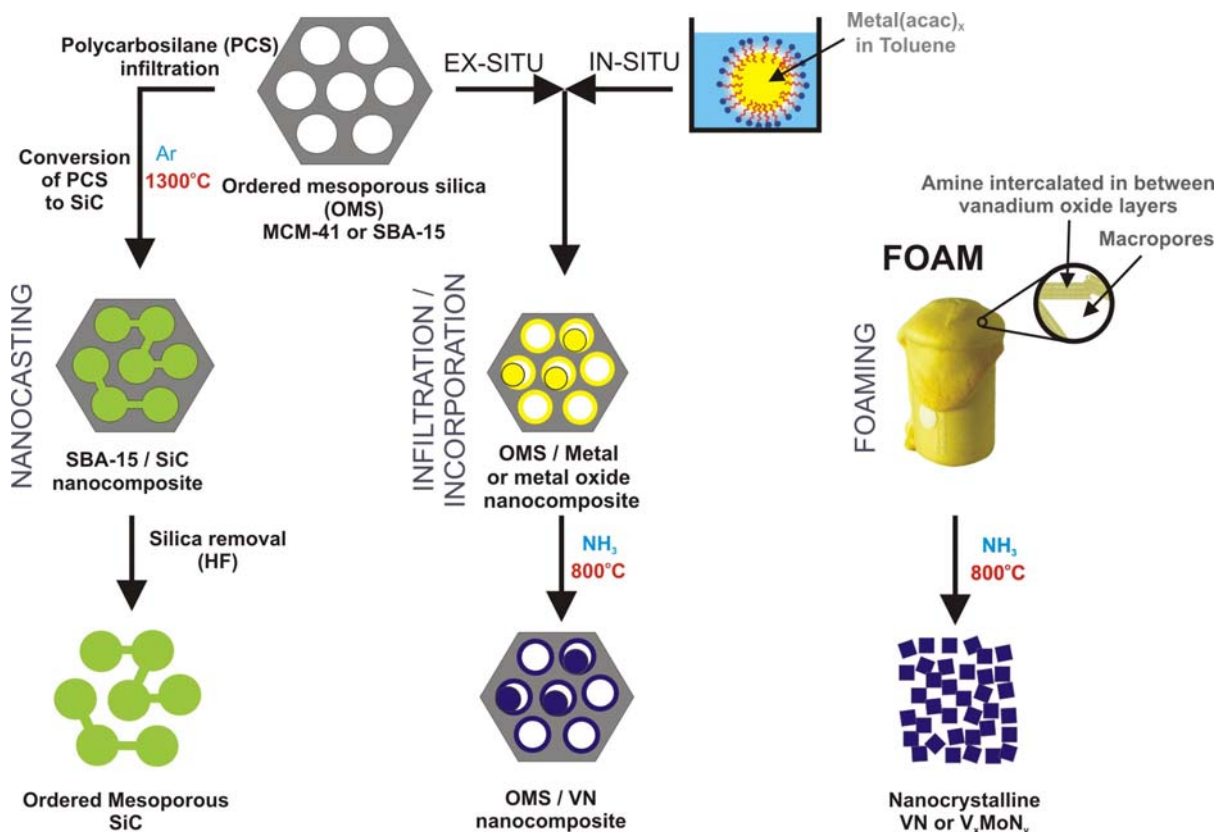
Scheme 11. Preparation of new high surface area nanostructured ceramics

Nevertheless, highly ordered mesoporous silicon carbide materials were obtained via polymer melt infiltration in SBA-15. The low molecular weight polycarbosilane used as a

preceramic precursor was converted at 1300 $^{\circ}$C to silicon carbide inside the SBA-15, and after subsequent silica removal by HF, a highly ordered mesoporous material was obtained. Ordered mesoporous silicon carbide prepared by the methods reported here, may be an interesting material as a support due to its high temperature stability, chemical inertness, high thermal conductivity and semiconductor properties.

In contrast to the nanocasting approach, based on the complete pore filling, also a new in-situ procedure for the preparation of finely dispersed metal and metal oxide particles inside ordered mesoporous silica was developed [Scheme 11 – IN-SITU and INFILTRATION/INCORPORATION]. A swelling agent (toluene) was used to deliver a hydrophobic platinum precursor into the surfactant micelles before addition of silica source. Such an in-situ method resulted in very high platinum incorporation (80-100%), not achieved for any other in-situ preparation procedures. Additionally, the presence of platinum allowed to decrease the template removal temperatures. Moreover, the method was also extended to other metal or metal oxide/ordered mesoporous silica systems. This may be especially interesting for the preparation of ordered mesoporous materials with low melting points, where typically the structure collapses during the high temperature calcinations process.

The in-situ synthesized V_2O_5/MCM-41 materials were used to prepare VN/MCM-41 composites via nitridation in ammonia at 800°C [Scheme 11 – OMS / VN nanocomposite]. This method allowed to prepare highly dispersed, X-ray amorphous vanadium nitride species, with high activity in the propane dehydrogenation. Compared to nitridation of supported vanadium oxide prepared via the ex-situ procedure, in-situ synthesized materials showed similar catalytic activity, in spite of having significantly lower vanadium loading.

As an alternative for the preparation of supported nitride materials, a novel preparation procedure of bulk not supported nanocrystalline vanadium nitride with high surface area was presented. Instead of pure oxide powder (which was typically used in the preparation of high surface area vanadium nitride catalysts), a macroporous amine intercalated V_2O_5 was used as the starting material [Scheme 11 – FOAMING]. The obtained nitride consisted of small crystallites and had a surface area up to 198 m^{2}g^{-1}. Moreover, this foam-derived VN showed significantly improved activity as a catalyst in propane dehydrogenation. This novel preparation method could also be extended to other systems such as ternary VMo_xN_y nitrides.

6 Glossary

M41S   Family of mesoporous MCM materials "**M**obile **C**omposition of **M**atter"

    MCM-41 Hexagonal mesoporous phase (p6m)

    MCM-48 Cubic mesoporous phase (Ia3d)

    MCM-50 Lamellar mesoporous phase (p2)

FSM   Mesoporous materials prepared form kanemite

APM   **A**cid **P**repared **M**esostructures

SBA   Mesoporous materials derived by APM method "**S**anta **B**arbara **A**cid prepared materials"

    SBA-1   Cubic mesoporous phase (Pm3n)

    SBA-3   Hexagonal mesoporous phase (P6m)

    SBA-15   Hexagonal mesoporous large pore phase prepared using block copolymer (P6m)

    SBA-16   Cubic mesoporous large pore phase prepared using block copolymers (Pm3n)

    KIT-6   Cubic mesorporous large pore phase using block copolymers (Ia3d)

KIT   Materials synthesized by **K**orea Advanced **I**nstitute of **T**echnology (KAIST)

CMK   **C**arbons **M**esotructured by **K**AIST

    CMK-1   Carbon inverse replica of MCM-48 with $I4_132$ symmetry

    CMK-2   Carbon inverse replica of SBA-1 with unknown cubic symmetry

    CMK-3   Carbon inverse replica of SBA-15 with P6m symmetry

    CMK-5   Tubular carbon (nanopipe) replica of SBA-15 with P6m symmetry

    CMK-8   Carbon inverse replica of KIT-6 with Ia3d or $I4_132$ symmetry

7   References

[1]   C. T. Kresge, M. E. Leonowicz, W. J. Roth, J. C. Vartuli, J. S. Beck, *Nature* **1992**, *359*, 710-712.

[2]   J. S. Beck, J. C. Vartuli, W. J. Roth, M. E. Leonowicz, C. T. Kresge, K. D. Schmitt, C. T. W. Chu, D. H. Olson, E. W. Sheppard, S. B. McCullen, J. B. Higgins, J. L. Schlenker, *J. Am. Chem. Soc.* **1992**, *114*, 10834-10843.

[3]   A. Taguchi, F. Schüth, *Microporous Mesoporous Mater.* **2005**, *77*, 1-45.

[4]   Y. J. Ying, C. P. Mehnert, M. S. Wong, *Angew. Chem. Int. Ed.* **1999**, *38*, 56-77.

[5]   U. Ciesla, F. Schüth, *Microporous Mesoporous Mater.* **1999**, *27*, 131-149.

[6]   A. Vinu, V. Murugesan, O. Tangermann, M. Hartmann, *Chem. Mater.* **2004**, *16*, 3056-3065.

[7]   D. Y. Zhao, J. L. Feng, Q. S. Huo, N. Melosh, G. H. Fredrickson, B. F. Chmelka, G. D. Stucky, *Science* **1998**, *279*, 548-552.

[8]   D. Y. Zhao, Q. S. Huo, J. L. Feng, B. F. Chmelka, G. D. Stucky, *J. Am. Chem. Soc.* **1998**, *120*, 6024-6036.

[9]   F. Schüth, *Chem. Mater.* **2001**, *13*, 3184-3195.

[10]   A. Sayari, P. Liu, *Microporous Mater.* **1997**, *12*, 149-177.

[11]   R. Ryoo, S. H. Joo, S. Jun, *J. Phys. Chem. B* **1999**, *103*, 7743-7746.

[12]   S. Jun, S. H. Joo, R. Ryoo, M. Kruk, M. Jaroniec, Z. Liu, T. Ohsuna, O. Terasaki, *J. Am. Chem. Soc.* **2000**, *122*, 10712-10713.

[13]   R. Ryoo, S. H. Joo, M. Kruk, M. Jaroniec, *Adv. Mater.* **2001**, *13*, 677-681.

[14]   A. H. Lu, W. Schmidt, A. Taguchi, B. Spliethoff, B. Tesche, F. Schüth, *Angew. Chem. Int. Ed.* **2002**, *41*, 3489-3492.

[15]   J. Roggenbuck, M. Tiemann, *J. Am. Chem. Soc.* **2005**, *127*, 1096-1097.

[16]   P. Dibandjo, L. Bois, F. Chassagneux, D. Cornu, J. M. Letoffe, B. Toury, F. Babonneau, P. Miele, *Adv. Mater.* **2005**, *17*, 571-574.

[17]   K. A. Schwetz in *Handbook of Ceramic Hard Materials*, Vol. 1 (Ed: R. Riedel) Wiley-VCH, Weinheim **2000**, 683-740.

[18]   M. J. Ledoux, C. Pham-Huu, *Cattech* **2001**, *5*, 226-246.

[19]   M. Sternitzke, *J. European Ceram. Soc.* **1997**, *17*, 1061-1082.

[20]   P. Krawiec, C. Weidenthaler, S. Kaskel, *Chem. Mater.* **2004**, *16*, 2869-2880.

[21]   P. Krawiec, S. Kaskel, *J.Solid State Chem.* **2006**, *179*, 2281-2289.

[22] P. Krawiec, D. Geiger, S. Kaskel, *Chem.Commun.* **2006**, *23*, 2469-2470.

[23] R. B. Levy, M. Boudart, *Science* **1973**, *181*, 547-549.

[24] S. T. Oyama in *The Chemistry of Transition Metal Carbides and Nitrides*, (Ed: S. T. Oyama) Blackie Academic & Professional, London **1996**,

[25] P. Krawiec, P. L. De Cola, R. Gläser, J. Weitkamp, C. Weidenthaler, S. Kaskel, *Adv.Mater.* **2006**, *18*, 505-508.

[26] R. Kapoor, S. T. Oyama, *J. Solid State Chem.* **1992**, *99*, 303-312.

[27] P. Krawiec, E. Kockrick, G. Auffermann, P. Simon, S. Kaskel, *Chem.Mater.* **2006**, *18*, 2663-2669.

[28] A. Lind, J. Andersson, S. Karlsson, P. Agren, P. Bussian, H. Amenitsch, M. Linden, *Langmuir* **2002**, *18*, 1380-1385.

[29] K. S. W. Sing, D. H. Everett, R. A. W. Haul, L. Moscou, R. A. Pierotti, J. Rouquerol, T. Siemieniewska, *Pure Appl. Chem.* **1985**, *57*, 603-619.

[30] J. Weitkamp, *Solid State Ion.* **2000**, *131*, 175-188.

[31] Y. Ma, W. Tong, H. Zhou, S. L. Suib, *Microporous Mesoporous Mater.* **2000**, *37*, 243-252.

[32] O. M. Yaghi, M. O'Keeffe, N. W. Ockwig, H. K. Chae, M. Eddaoudi, J. Kim, *Nature* **2003**, *423*, 705-714.

[33] S. Kitagawa, R. Kitaura, S. Noro, *Angew. Chem. Int. Ed.* **2004**, *43*, 2334-2375.

[34] J. L. C. Rowsell, O. M. Yaghi, *Microporous Mesoporous Mater.* **2004**, *73*, 3-14.

[35] S. Kaskel in *Handbook of Porous Solids*, (Ed: Schüth F., Sing K. S. W. and W. J) Wiley VCH, Weinheim **2002**, 1190-1249.

[36] E. Auer, A. Freund, J. Pietsch, T. Tacke, *Appl. Catal. A-Gen.* **1998**, *173*, 259-271.

[37] G. Chaplais, K. Schlichte, O. Stark, R. A. Fischer, S. Kaskel, *Chem. Commun.* **2003**, 730-731.

[38] V. C. Menon, S. Komarneni, *J. Porous Mater.* **1998**, *5*, 43-58.

[39] J. L. C. Rowsell, A. R. Millward, K. S. Park, O. M. Yaghi, *J. Am. Chem. Soc.* **2004**, *126*, 5666-5667.

[40] A. C. Dillon, M. J. Heben, *Appl. Phys. A-Mater. Sci. Process.* **2001**, *72*, 133-142.

[41] P. Krawiec, M. Kramer, M. Sabo, R. Künschke, H. Fröde, S. Kaskel, *Adv.Eng.Mater* **2006**, *8*, 293-296.

[42] Z. Y. Yuan, B. L. Su, *J. Mater. Chem.* **2006**, *16*, 663-677.

[43] S. Polarz, B. Smarsly, *J. Nanosci. Nanotechnol.* **2002**, *2*, 581-612.

[44] C. M. Soukoulis, *Nanotechnology* **2002**, *13*, 420-423.

[45]   J. M. Thomas, W. J. Thomas, *Principles and Practice of Heterogeneous Catalysis*, VCH, Weinheim, **2005**.

[46]   A. Firouzi, D. Kumar, L. M. Bull, T. Besier, P. Sieger, Q. Huo, S. A. Walker, J. A. Zasadzinski, C. Glinka, J. Nicol, D. Margolese, G. D. Stucky, B. F. Chmelka, *Science* **1995**, *267*, 1138-1143.

[47]   Q. S. Huo, D. I. Margolese, G. D. Stucky, *Chem. Mater.* **1996**, *8*, 1147-1160.

[48]   Q. S. Huo, R. Leon, P. M. Petroff, G. D. Stucky, *Science* **1995**, *268*, 1324-1327.

[49]   J. M. Kim, S. K. Kim, R. Ryoo, *Chem. Commun.* **1998**, 259-260.

[50]   A. Corma, *Chem. Rev.* **1997**, *97*, 2373-2419.

[51]   S. Gontier, A. Tuel *Stud. Surf. Sci. Catal.* **1995**, *97*, 157-164.

[52]   S. Che, Z. Liu, T. Ohsuna, K. Sakamoto, O. Terasaki, T. Tatsumi, *Nature* **2004**, *429*, 281-284.

[53]   F. P. Matthae, D. Genske, C. Minchev, H. Lechert *Stud. Surf. Sci. Catal.* **1998**, *117*, 223-230.

[54]   J. C. Vartuli, K. D. Schmitt, C. T. Kresge, W. J. Roth, M. E. Leonowicz, S. B. McCullen, S. D. Hellring, J. S. Beck, J. L. Schlenker, D. H. Olson, E. W. Sheppard, *Chem. Mater.* **1994**, *6*, 2317-2326.

[55]   Q. S. Huo, D. I. Margolese, U. Ciesla, D. G. Demuth, P. Y. Feng, T. E. Gier, P. Sieger, A. Firouzi, B. F. Chmelka, F. Schüth, G. D. Stucky, *Chem. Mater.* **1994**, *6*, 1176-1191.

[56]   F. Kleitz, S. H. Choi, R. Ryoo, *Chem. Commun.* **2003**, 2136-2137.

[57]   A. Galarneau, N. Cambon, F. Di Renzo, R. Ryoo, M. Choi, F. Fajula, *New J. Chem.* **2003**, *27*, 73-79.

[58]   C. Booth, D. Attwood, *Macromol. Rapid Commun.* **2000**, *21*, 501-527.

[59]   J. N. Israelachvili, H. Wennerstrom, *J. Phys. Chem.* **1992**, *96*, 520-531.

[60]   G. Wanka, H. Hoffmann, W. Ulbricht, *Macromolecules* **1994**, *27*, 4145-4159.

[61]   D. M. Antonelli, J. Y. Ying, *Angew. Chem. Int. Ed.* **1995**, *34*, 2014-2017.

[62]   U. Ciesla, S. Schacht, G. D. Stucky, K. K. Unger, F. Schüth, *Angew. Chem. Int. Ed.* **1996**, *35*, 541-543.

[63]   Q. S. Huo, D. I. Margolese, U. Ciesla, P. Y. Feng, T. E. Gier, P. Sieger, R. Leon, P. M. Petroff, F. Schüth, G. D. Stucky, *Nature* **1994**, *368*, 317-321.

[64]   P. Liu, I. L. Moudrakovski, J. Liu, A. Sayari, *Chem. Mater.* **1997**, *9*, 2513-2520.

[65]   P. D. Yang, D. Y. Zhao, D. I. Margolese, B. F. Chmelka, G. D. Stucky, *Nature* **1998**, *396*, 152-155.

[66]   P. V. Braun, P. Osenar, V. Tohver, S. B. Kennedy, S. I. Stupp, *J. Am. Chem. Soc.* **1999**, *121*, 7302-7309.

[67]   V. Tohver, P. V. Braun, M. U. Pralle, S. I. Stupp, *Chem. Mater.* **1997**, *9*, 1495-1498.

[68]   P. Osenar, P. V. Braun, S. I. Stupp, *Adv. Mater.* **1996**, *8*, 1022-1025.

[69]   D. Farrusseng, K. Schlichte, B. Spliethoff, A. Wingen, S. Kaskel, J. S. Bradley, F. Schüth, *Angew. Chem. Int. Ed.* **2001**, *40*, 4204-4207.

[70]   S. Kaskel, D. Farrusseng, K. Schlichte, *Chem. Commun.* **2000**, 2481-2482.

[71]   S. Kaskel, K. Schlichte, B. Zibrowius, *Phys. Chem. Chem. Phys.* **2002**, *4*, 1675-1681.

[72]   G. S. Attard, C. G. Goltner, J. M. Corker, S. Henke, R. H. Templer, *Angew. Chem.Int. Ed.* **1997**, *36*, 1315-1317.

[73]   W. P. Guo, X. S. Zhao *Stud. Surf. Sci. Catal.* **2005**, *156*, 551-556.

[74]   T. W. Kim, F. Kleitz, B. Paul, R. Ryoo, *J. Am. Chem. Soc.* **2005**, *127*, 7601-7610.

[75]   S. H. Joo, S. J. Choi, I. Oh, J. Kwak, Z. Liu, O. Terasaki, R. Ryoo, *Nature* **2001**, *412*, 169-172.

[76]   M. Kruk, M. Jaroniec, T. W. Kim, R. Ryoo, *Chem. Mater.* **2003**, *15*, 2815-2823.

[77]   A. H. Lu, W. C. Li, W. Schmidt, W. Kiefer, F. Schüth, *Carbon* **2004**, *42*, 2939-2948.

[78]   M. Kang, S. H. Yi, H. I. Lee, J. E. Yie, J. M. Kim, *Chem. Commun.* **2002**, 1944-1945.

[79]   N. S. Yao, C. Pinckney, S. Y. Lim, C. Pak, G. L. Haller, *Microporous Mesoporous Mater.* **2001**, *44*, 377-384.

[80]   A. Jentys, W. Schiesser, H. Vinek, *Catal. Today* **2000**, *59*, 313-321.

[81]   U. Junges, W. Jacobs, I. Voigtmartin, B. Krutzsch, F. Schüth, *J. Chem. Soc., Chem. Commun.* **1995**, 2283-2284.

[82]   C. Yang, U. Wüstefeld, M. Kalwei, F. Schüth *Stud. Surf. Sci. Catal.* **2004**, *154*, 2574-2580.

[83]   C. M. Yang, H. S. Sheu, K. J. Chao, *Adv. Funct. Mater.* **2002**, *12*, 143-148.

[84]   C. M. Yang, P. H. Liu, Y. F. Ho, C. Y. Chiu, K. J. Chao, *Chem. Mater.* **2003**, *15*, 275-280.

[85]   H. Araki, A. Fukuoka, Y. Sakamoto, S. Inagaki, N. Sugimoto, Y. Fukushima, M. Ichikawa, *J. Mol. Catal. A-Chem.* **2003**, *199*, 95-102.

[86]   R. M. Rioux, H. Song, J. D. Hoefelmeyer, P. Yang, G. A. Somorjai, *J. Phys. Chem. B* **2005**, *109*, 2192-2202.

[87]   M. A. Aramendia, V. Borau, C. Jimenez, J. M. Marinas, F. J. Romero, *Chem. Commun.* **1999**, 873-874.

[88]   M. Chatterjee, T. Iwasaki, Y. Onodera, T. Nagase, *Catal. Lett.* **1999**, *61*, 199-202.

[89]   J. Zhu, Z. Konya, V. F. Puntes, I. Kiricsi, C. X. Miao, J. W. Ager, A. P. Alivisatos, G. A. Somorjai, *Langmuir* **2003**, *19*, 4396-4401.

[90]   K. J. Lin, L. J. Chen, M. R. Prasad, C. Y. Cheng, *Adv. Mater.* **2004**, *16*, 1845-1848.

[91]   Z. Konya, V. F. Puntes, I. Kiricsi, J. Zhu, P. Alivisatos, G. A. Somorjai, *Catal. Lett.* **2002**, *81*, 137-140.

[92]   T. Yamada, H. S. Zhou, D. Hiroishi, M. Tomita, Y. Ueno, K. Asai, I. Honma, *Adv. Mater.* **2003**, *15*, 511-513.

[93]   C. M. Yang, M. Kalwei, F. Schüth, K. J. Chao, *Appl. Catal. A-Gen.* **2003**, *254*, 289-296.

[94]   U. Junges, F. Schüth, G. Schmid, Y. Uchida, R. Schlogl, *Phys. Chem. Chem. Phys.* **1997**, *101*, 1631-1634.

[95]   A. Y. Khodakov, A. Griboval-Constant, R. Bechara, V. L. Zholobenko, *J. Catal.* **2002**, *206*, 230-241.

[96]   J. Panpranot, J. G. Goodwin, A. Sayari, *Catal. Today* **2002**, *77*, 269-284.

[97]   J. Panpranot, J. G. Goodwin, A. Sayari, *J. Catal.* **2002**, *211*, 530-539.

[98]   J. Panpranot, J. G. Goodwin, A. Sayari, *J. Catal.* **2003**, *213*, 78-85.

[99]   A. Lewandowska, S. Monteverdi, M. Bettahar, M. Ziolek, *J. Mol. Catal. A-Chem.* **2002**, *188*, 85-95.

[100]   V. R. Choudhary, S. K. Jana, B. P. Kiran, *J. Catal.* **2000**, *192*, 257-261.

[101]   V. R. Choudhary, S. K. Jana, *J. Mol. Catal. A-Chem.* **2002**, *180*, 267-276.

[102]   J. M. Clacens, Y. Pouilloux, J. Barrault, *Appl. Catal. A-Gen.* **2002**, *227*, 181-190.

[103]   A. Maldotti, A. Molinari, G. Varani, M. Lenarda, L. Storaro, F. Bigi, R. Maggi, A. Mazzacani, G. Sartori, *J. Catal.* **2002**, *209*, 210-216.

[104]   T. Ookoshi, M. Onaka, *Chem. Commun.* **1998**, 2399-2400.

[105]   F. Schüth, A. Wingen, J. Sauer, *Microporous Mesoporous Mater.* **2001**, *44*, 465-476.

[106]   L. Zhang, G. C. Papaefthymiou, J. Y. Ying, *J. Phys. Chem. B* **2001**, *105*, 7414-7423.

[107]   E. R. Rivera-Munos, D. Lardizabal, G. Alonso, A. Aguilar, M. H. Siadati, R. R. Chianelli, *Catal. Lett.* **2003**, *85*, 147-151.

[108]   L. Vradman, M. V. Landau, M. Herskowitz, V. Ezersky, M. Talianker, S. Nikitenko, Y. Koltypin, A. Gedanken, *J. Catal.* **2003**, *213*, 163-175.

[109]   H. Koch, W. Reschetilowski, *Microporous Mesoporous Mater.* **1998**, *25*, 127-129.

[110]   A. Auroux, *Top. Catal.* **2002**, *19*, 205-213.

[111]   A. Corma, M. S. Grande, V. GonzalezAlfaro, A. V. Orchilles, *J. Catal.* **1996**, *159*, 375-382.

[112]   J. P. G. Pater, P. A. Jacobs, J. A. Martens, *J. Catal.* **1999**, *184*, 262-267.

[113]   X. X. Yan, C. Z. Yu, X. F. Zhou, J. W. Tang, D. Y. Zhao, *Angew. Chem. Int. Ed.* **2004**, *43*, 5980-5984.

[114]   X. X. Yan, H. X. Deng, X. H. Huang, G. Q. Lu, S. Z. Qiao, D. Y. Zhao, C. Z. Yu, *J. Non-Cryst. Solids* **2005**, *351*, 3209-3217.

[115]   X. X. Yan, X. H. Huang, C. Z. Yu, H. X. Deng, Y. Wang, Z. D. Zhang, S. Z. Qiaoc, G. Q. Lu, D. Y. Zhao, *Biomaterials* **2006**, *27*, 3396-3403.

[116]   Q. H. Shi, J. F. Wang, J. P. Zhang, J. Fan, G. D. Stucky, *Adv. Mater.* **2006**, *18*, 1038-1042.

[117]   F. Hoffmann, M. Cornelius, J. Morell, M. Fröba, *Angew. Chem. Int. Ed.* **2006**, *45*, 3216-3251.

[118]   T. Asefa, M. J. MacLachan, N. Coombs, G. A. Ozin, *Nature* **1999**, *402*, 867-871.

[119]   S. Inagaki, S. Guan, T. Ohsuna, O. Terasaki, *Nature* **2002**, *416*, 304-307.

[120]   D. J. Macquarrie, D. B. Jackson, *Chem. Commun.* **1997**, 1781-1782.

[121]   Y. Q. Wang, C. M. Yang, B. Zibrowius, B. Spliethoff, M. Linden, F. Schüth, *Chem. Mater.* **2003**, *15*, 5029-5035.

[122]   Y. Q. Wang, B. Zibrowius, C. M. Yang, B. Spliethoff, F. Schuth, *Chem. Commun.* **2004**, 46-47.

[123]   M. Raczka, G. Gorny, L. Stobierski, K. Rozniatowski, *Mater. Charact.* **2001**, *46*, 245-249.

[124]   L. Stobierski, A. Gubernat, *Ceram. Int.* **2003**, *29*, 287-292.

[125]   I. A. Ibrahim, F. A. Mohamed, E. J. Lavernia, *J. Mater. Sci.* **1991**, *26*, 1137-1156.

[126]   T. P. D. Rajan, R. M. Pillai, B. C. Pai, *J. Mater. Sci.* **1998**, *33*, 3491-3503.

[127]   M. Mitomo, Y. W. Kim, H. Hirotsuru, *J. Mater. Res.* **1996**, *11*, 1601-1604.

[128]   R. Moene, M. Makkee, J. A. Moulijn, *Appl. Catal. A* **1998**, *167*, 321-330.

[129]   M. J. Ledoux, S. Hantzer, C. P. Huu, J. Guille, M. P. Desaneaux, *J. Catal.* **1988**, *114*, 176-185.

[130]   C. Phamhuu, P. Delgallo, E. Peschiera, M. J. Ledoux, *Appl. Catal. A* **1995**, *132*, 77-96.

[131]   M. B. Kizling, P. Stenius, S. Andersson, A. Frestad, *Appl. Catal. B-Env.* **1992**, *1*, 149-168.

[132]   M. A. Vannice, Y. L. Chao, R. M. Friedman, *Appl. Catal.* **1986**, *20*, 91-107.

[133]   P. H. Cuong, S. Marin, M. J. Ledoux, M. Weibel, G. Ehret, M. Benaissa, E. Peschiera, J. Guille, *Appl. Catal. B-Env.* **1994**, *4*, 45-63.

[134]   G. Q. Jin, X. Y. Guo, *Microporous Mesoporous Mater.* **2003**, *60*, 207-212.

[135]   J. Parmentier, J. Patarin, J. Dentzer, C. Vix-Guterl, *Ceram. Int.* **2002**, *28*, 1-7.

[136]   Z. C. Liu, W. H. Shen, W. B. Bu, H. R. Chen, Z. L. Hua, L. X. Zhang, L. Li, J. L. Shi, S. H. Tan, *Microporous Mesoporous Mater.* **2005**, *82*, 137-145.

[137]   A. H. Lu, W. Schmidt, W. Kiefer, F. Schüth, *J. Mater. Sci.* **2005**, *40*, 5091-5093.

[138]   V. G. Pol, S. V. Pol, A. Gedanken, *Chem. Mater.* **2005**, *17*, 1797-1802.

[139]   C. L. Bowes, A. Malek, G. A. Ozin, *Chem. Vapor Depos.* **1996**, *2*, 97-103.

[140]   E. Chomski, O. Dag, A. Kuperman, N. Coombs, G. A. Ozin, *Chem. Vapor Depos.* **1996**, *2*, 8-13.

[141]   O. Dag, G. A. Ozin, H. Yang, C. Reber, G. Bussiere, *Adv. Mater.* **1999**, *11*, 474-480.

[142]   I. Golecki, *Mater. Sci. Eng. R-Rep.* **1997**, *20*, 37-124.

[143]   Y. F. Shi, Y. Meng, D. H. Chen, S. J. Cheng, P. Chen, T. F. Yang, Y. Wan, D. Y. Zhao, *Adv. Funct. Mater.* **2006**, *16*, 561-567.

[144]   W. Lengauer in *Handbook of Ceramic Hard Materials*, Vol. 1 (Ed: R. Riedel) Wiley-VCH, Weinheim **2000**, Ch. 7.

[145]   W. S. Williams, *JOM* **1997**, *49*, 38-42.

[146]   R. Sanjines, P. Hones, F. Levy, *Thin Solid Films* **1998**, *332*, 225-229.

[147]   S. T. Oyama, *Catal. Today* **1992**, *15*, 179-200.

[148]   S. Z. Li, J. S. Lee, T. Hyeon, K. S. Suslick, *Appl. Catal. A: Gen.* **1999**, *184*, 1-9.

[149]   E. Furimsky, *Appl. Catal. A:Gen.* **2003**, *240*, 1-28.

[150]   M. Nagai, T. Suda, K. Oshikawa, N. Hirano, S. Omi, *Catal. Today* **1999**, *50*, 29-37.

[151]   H. Kwon, S. Choi, L. T. Thompson, *J. Catal.* **1999**, *184*, 236-246.

[152]   S. Kaskel, K. Schlichte, G. Chaplais, M. Khanna, *J. Mater. Chem.* **2003**, *13*, 1496-1499.

[153]   J. R. Groza, *Nanostruct. Mater.* **1999**, *12*, 987-992.

[154]   J. R. Groza, *Int. J. Powder Metall.* **1999**, *35*, 59-66.

[155]   J. A. J. Rodrigues, G. M. Cruz, G. Bugli, M. Boudart, G. DjegaMariadassou, *Catal. Lett.* **1997**, *45*, 1-3.

[156]   R. Kapoor, S. T. Oyama, *J. Solid State Chem.* **1995**, *120*, 320-326.

[157]   S. T. Oyama, R. Kapoor, H. T. Oyama, D. J. Hofmann, E. Matijevic, *J. Mater. Res.* **1993**, *8*, 1450-1454.

[158]   L. Volpe, S. T. Oyama, M. Boudart, *Stud. Surf. Sci. Catal.* **1983**, *16*, 147-158.

[159]   M. Nagai, R. Nakauchi, *Silic. Ind.* **2004**, *69*, 61-67.

[160]   C. Shi, A. M. Zhu, X. F. Yang, C. T. Au, *Appl. Catal. A-Gen.* **2005**, *293*, 83-90.

[161]   F. Rouquerol, J. Rouquerol, K. Sing, *Adsorption by Powders & Porous Solids*, Academic Press, San Diego, **1998**.

[162]   E. P. Barrett, L. G. Joyner, P. P. Halenda, *J. Am. Chem. Soc.* **1951**, *73*, 373-380.

[163]   I. Langmuir, *J.Am.Chem.Soc* **1918**, *40*, 1361.

[164]   S. Brunauer, P. Emmett, E. Teller, *J.Am.Chem.Soc* **1938**, *60*, 309.

[165]   J. H. Deboer, B. G. Linsen, Vanderpl.T, Zonderva.Gj, *J. Catal.* **1965**, *4*, 649-&.

[166]   M. Choi, W. Heo, F. Kleitz, R. Ryoo, *Chem. Commun.* **2003**, 1340.

[167]   M. Grün, I. Lauer, K. K. Unger, *Adv. Mater.* **1997**, *9*, 254.

[168]   M. Grün, K. K. Unger, A. Matsumoto, K. Tsutsumi, *Microporous Mesoporous Mater.* **1999**, *27*, 207-216.

[169]   P. Krawiec, *Master Thesis* **2002**, *Max-Planck Institute in Mülheim an Der Ruhr*, Germany.

[170]   J. R. Guth, W. T. Petuskey, *J. Phys. Chem.* **1987**, *91*, 5361-5364.

[171]   G. Roewer, U. Herzog, K. Trommer, E. Müller, S. Frühauf, *Struct. Bond.* **2002**, *101*, 60-127.

[172]   H. M. Williams, E. A. Dawson, P. A. Barnes, B. Rand, R. M. D. Brydson, A. R. Brough, *J. Mater. Chem.* **2002**, *12*, 3754-3760.

[173]   V. Belot, R. J. P. Corriu, D. Leclercq, P. H. Mutin, A. Vioux, *J. Non-Cryst. Solids* **1992**, *144*, 287-297.

[174]   Y. ElKortobi, J. B. E. delaCaillerie, A. P. Legrand, X. Armand, N. Herlin, M. Cauchetier, *Chem. Mater.* **1997**, *9*, 632-639.

[175]   T. Merlemejean, E. Abdelmounim, P. Quintard, *J. Mol. Struct.* **1995**, *349*, 105-108.

[176]   K. Cassiers, T. Linssen, M. Mathieu, M. Benjelloun, K. Schrijnemakers, P. Van Der Voort, P. Cool, E. F. Vansant, *Chem. Mater.* **2002**, *14*, 2317-2324.

[177]   M. Kruk, M. Jaroniec, R. Ryoo, S. H. Joo, *J. Phys. Chem. B* **2000**, *104*, 7960-7968.

[178]   C. Raynaud, *J. Non-Cryst. Solids* **2001**, *280*, 1-31.

[179]   H. F. Yang, Y. Yan, Y. Liu, F. Q. Zhang, R. Y. Zhang, Y. Meng, M. Li, S. H. Xie, B. Tu, D. Y. Zhao, *J. Phys. Chem. B* **2004**, *108*, 17320.

[180]   L. A. Solovyov, T. W. Kim, F. Kleitz, O. Terasaki, R. Ryoo, *Chem. Mater.* **2004**, *16*, 2274.

[181]   S. N. Che, K. Lund, T. Tatsumi, S. Iijima, S. H. Joo, R. Ryoo, O. Terasaki, *Angew. Chem.Int. Ed.* **2003**, *42*, 2182.

[182]   F. Kleitz, W. Schmidt, F. Schüth, *Microporous Mesoporous Mater.* **2003**, *65*, 1-29.

[183]   M. T. J. Keene, R. D. M. Gougeon, R. Denoyel, R. K. Harris, J. Rouquerol, P. L. Llewellyn, *J. Mater. Chem.* **1999**, *9*, 2843-2850.

[184]   A. Montes, E. Cosenza, G. Giannetto, E. Urquieta, R. A. de Melo, N. S. Gnep, M. Guisnet, *Stud. Surf. Sci. Catal.* **1998**, *117*, 237.

[185] V. Fornes, C. Lopez, H. H. Lopez, A. Martinez, *Appl. Catal. A: Gen.* **2003**, *249*, 345-354.

[186] S. Shylesh, A. P. Singh, *J. Catal.* **2004**, *228*, 333-346.

[187] J. George, S. Shylesh, A. P. Singh, *Appl. Catal. A: Gen.* **2005**, *290*, 148-158.

[188] L. Abis, D. B. Dell' Amico, C. Busetto, F. Calderazzo, R. Caminiti, C. Ciofi, F. Garbassi, G. Masciarelli, *J. Mater. Chem.* **1998**, *8*, 751-759.

[189] K. M. Reddy, I. Moudrakovski, A. Sayari, *J. Chem. Soc.,Chem. Commun.* **1994**, 1059-1060.

[190] J. S. Reddy, P. Liu, A. Sayari, *Appl. Catal. A: Gen.* **1996**, *148*, 7-21.

[191] K. J. Chao, C. N. Wu, H. Chang, L. J. Lee, S. F. Hu, *J. Phys. Chem. B* **1997**, *101*, 6341-6349.

[192] J. Patarin, *Angew. Chem. Int. Ed.* **2004**, *43*, 3878-3880.

[193] Z. Huang, L. Huang, S. C. Shen, C. C. Poh, K. Hidajat, S. Kawi, S. C. Ng, *Microporous Mesoporous Mater.* **2005**, *80*, 157-163.

[194] W. A. Gornes, L. A. M. Cardoso, A. R. E. Gonzaga, L. G. Aguiar, H. M. C. Andrade, *Mater. Chem. Phys.* **2005**, *93*, 133-137.

[195] A. N. Parikh, A. Navrotsky, Q. H. Li, C. K. Yee, M. L. Amweg, A. Corma, *Microporous Mesoporous Mater.* **2004**, *76*, 17-22.

[196] F. Kleitz, W. Schmidt, F. Schüth, *Microporous Mesoporous Mater.* **2001**, *44*, 95-109.

[197] T. Asefa, M. Kruk, N. Coombs, H. Grondey, M. J. MacLachlan, M. Jaroniec, G. A. Ozin, *J. Am. Chem. Soc.* **2003**, *125*, 11662-11673.

[198] O. Merdrignac-Conanec, K. El Badraoui, P. L'Haridon, *J. Solid State Chem.* **2005**, *178*, 218-223.

[199] F. Solymosi, R. Nemeth, L. Ovari, L. Egri, *J. Catal.* **2000**, *195*, 316-325.

[200] G. T. Chandrappa, N. Steunou, J. Livage, *Nature* **2002**, *416*, 702.

[201] B. Alonso, J. Livage, *J. Solid State Chem.* **1999**, *148*, 16-19.

[202] STOE Size/Strain analysis software with implemented Scherrer equation (WinXPOW) v.1.06 **1999**

[203] J. Mendialdua, R. Casanova, Y. Barbaux, *J. Electron Spectrosc. Relat. Phenom.* **1995**, *71*, 249-261.

[204] P. S. Herle, M. S. Hegde, N. Y. Vasathacharya, S. Philip, *J. Solid State Chem.* **1997**, *134*, 120-127.

[205] J. G. Choi, *Appl. Surf. Sci.* **1999**, *148*, 64-72.

[206] W. T. Xu, T. Fujimoto, B. Q. Li, I. Kojima, *Appl. Surf. Sci.* **2001**, *175*, 456-461.

[207]   Y. J. Zhang, Q. Xin, I. Rodriguez-Ramos, A. Guerrero-Ruiz, *Appl. Catal. A:Gen.* **1999**, *180*, 237-245.

[208]   A. H. Adams, F. Haass, T. Buhrmester, J. Kunert, J. Ott, H. Vogel, H. Fuess, *J. Mol. Catal. A-Chem.* **2004**, *216*, 67-74.

[209]   M. I. Shukoor, H. A. Therese, L. Gorgishvili, G. Glasser, U. Kolb, W. Tremel, *Chem. Mater.* **2006**, *18*, 2144-2151.

[210]   I. M. Arabatzis, P. Falaras, *Nano Lett.* **2003**, *3*, 249-251.

Publications:

1. Krawiec P., Weidenthaler C. Kaskel S.
    "SiC/MCM-48 and SiC/SBA-15 nanocomposites"
    Chemistry of Materials **2004,** *16*, 2869-2880
    DOI: 10.1021/cm034737+

2. Krawiec P., DeCola P.L. Glaser R., Weitkamp J., Weidenthaler C., Kaskel S.
    "Oxide foams for the synthesis of high surface area vanadium nitride catalysts"
    Advanced Materials **2006**, *18*, 505-509
    DOI: 10.1002/adma.200500278

3. Krawiec P., Kramer M., Sabo M., Kunschke R., Fröde H., Kaskel S.
    „Improved hydrogen storage in the metal-organic framework $Cu_3(BTC)_2$"
    Advanced Engineering Materials **2006**, *8,* 293-296
    DOI: 10.1002/adem.200500223

4. Krawiec P., Kockrick E., Simon P, Auffermann G. Kaskel S.
    „Platinum-catalyzed template removal for the in-situ preparation of MCM-41 supported catalysts"
    Chemistry of Materials **2006,** *18,* 2663-2669
    DOI: 10.1021/cm052830n

5. Krawiec P., Geiger D, Kaskel S.
    „Ordered mesoporous silicon carbide (OM-SiC) via polymer precursor nanocasting"
    Chemical Communication*s* **2006**, *23*, 2469-2470
    DOI: 10.1039/b603284b

6. Krawiec P., Kaskel S.
    „Thermal stability of high surface area silicon carbide materials"
    Journal of Solid State Chemistry **2006**, *179,* 2281-2289
    DOI:10.1016/j.jssc.2006.02.034

Conference contributions:

2004.03 - oral	16th German zeolite conference, Dresden, Germany "High surface area SiC via infiltration of ordered mesoporous silica"
2005.03 - poster	17th German zeolite conference, Giessen, Germany "Oxide foams for the preparation of high surface area vanadium nitride"
2005.09 - oral + poster	Workshop on advanced materials (WAM III), Stellenbosch, South Africa "Oxide foams for the preparation of high surface area vanadium nitride catalysts"
2005.05 - oral	Mitteldeutsches Anorganisches Nachwuchs Symposium MANS III, Leipzig, Germany „Efficient one step synthesis of Pt/MCM-41 materials"
2006.03 - poster	18th Zeolite conference, Hannover, Germany „Platinum-catalysed template removal for the in-situ synthesis of MCM-41 supported catalysts"
2006.03 - poster	XXXVIII Polish catalysis conference Kraków, Poland "Preparation of highly ordered mesoporous silicon carbide materials – a new high temperature stable catalyst support"
2006.06 - oral	Solid state chemistry seminar, Hirschegg, Germany "High surface area nanostructured ceramics for catalytic applications"
2006.09 - oral	European Materials Research Society (E-MRS) meeting, Warsaw, Poland "Highly ordered mesoporous silicon carbide materials – a new high temperature stable catalyst support"

<h1>CURRICULUM VITAE</h1>

Personal Details:

Name:	Piotr Krawiec
Date of Birth:	18th May 1978
Nationality:	Polish
Address in Poland:	22-400 Zamość ul.Wiejska 10
Address in Germany:	01219 Dresden Kreischaer str.12
Telephone:	+48602680776
E-mail:	*piotr.krawiec@chemie.tu-dresden.de*
Family status:	Single

Languages:

English	fluent
German	medium
Russian	basic
Polish	native language

University Education:

1997 - 2002	**University of Mining and Metallurgy in Cracow (AGH) : Poland** – Faculty of Materials Science and Ceramics with a specialisation of Materials Science (graduated 2002 with the excellent degree of 6 – M.Sc.Eng.)
2000	**University of Ghent : Belgium** – Department of Electronics and Information Systems (one semester on Socrates scholarship)
2001 - 2002	**University of Applied Sciences Münster : Germany** – Master of Science studies in Chemical Engineering Faculty (graduated 2002 with honours - final note Excellent 1.0 – M.Sc.)

M.Sc. / PhD work carried at:

M.Sc. (2002)	**Max-Planck-Institut für Kohlenforschung in Mülheim an der Ruhr : Germany** – "Synthesis and Infiltration of Mesoporous Silica Materials with Silicon Carbide"
PhD (2003 – 2006)	**Max-Planck-Institut für Kohlenforschung in Mülheim an der Ruhr : Germany** (01.2003-04.2004) "Nanostructured Porous High Surface Area Ceramics for Catalytic Applications"
	Technical University of Dresden : Germany (05.2004-07.2006) – after moving with the whole group to Dresden, continuation of the PhD work and assistant in the courses of the inorganic chemistry

Practical training / internship:

2000   **University of Bristol : U.K.** – Department of Physics (two months working in polymer physics group - using the maximum entropy method to interpret Small Angle X-Ray Diffraction Images of Polyethylene and Polyurethane)

2001   **Colorobbia S.A. : Spain** – two months of training in the field of production, creation and development of frits, glazes, pigments and other raw materials for ceramic industry.

Teaching experience (at TU-Dresden):

2004   **Inorganic Chemistry Laboratory and Seminars** for 1st semester students

2004-2006   **Advanced Inorganic Chemistry Laboratory** for 6th semester students (Porous Materials Synthesis and Characterization)

2005-2006   **Advanced Inorganic Chemistry Laboratory** for 8th semester students (Porous Materials Synthesis and Characterization)

Awards and Scholarships:

1998 - 2001   **Rector's Award (AGH)**: each year for the best students on the year in the materials science and ceramics faculty (adequately 7th, 2nd, 2nd, and 1st)

1998 - 2002   **University Scholarship (AGH)**: each year for good results during studies

2000   **Staszic Bronze Award (AGH)**: for outstanding student of AGH university

2003   **FH-Münster Award**: for the best master thesis in the chemical engineering faculty in 2002

2002 - 2004   **Max Planck Fellowship**: financial support for the PhD studies in MPI für Kohlenforschung

Versicherung

Hiermit versichere ich, dass ich die vorliegende Arbeit ohne unzulässige Hilfe Dritter und ohne Benutzung anderer als der angegebenen Hilfsmittel angefertigt habe; die aus fremden Quellen direkt oder indirekt übernommenen Gedanken sind als solche kenntlich gemacht. Die Arbeit wurde bisher weder im Inland noch im Ausland in gleicher oder ähnlicher Form einer anderen Prüfungsbehörde vorgelegt.

Erklärung

Die vorliegende Arbeit wurde am Max-Planck Institut für Kohlenforschung in Mülheim an der Ruhr und am Institut für Anorganische Chemie der Technischen Universität Dresden unter wissenschaftlichen Betreung von Herrn Prof. Dr. Stefan Kaskel im Zeitraum von Dezember 2002 bis Mai 2006 angefertigt.

Es haben keine früheren erfolglosen Promotionsverfahren stattgefunden.

Hiermit erkenne ich die Promotionsordnung der Fakultät Mathematik und Naturwissenschaften der Technischen Universität Dresden vom 17. April 2003 an.

Dresden, den 1.08.2006   Piotr Krawiec